Doctoral Dissertation
Doctoral Program in Metrology (31th cycle)

Josephson devices for ac quantum voltage standard

From dry-cooling to metrological application

Paolo Durandetto

* * * * * *

Supervisors
Dr. Ing. Andrea Sosso, Supervisor, INRiM
Dr. Eugenio Monticone, Co-supervisor, INRiM

Doctoral Examination Committee:
Prof. Dr. Marian Kampik, Referee, Silesian University of Technology, Poland
Dr. Ing. Alessio Pollarolo, Referee, Measurement International Ltd, Canada
Dr. Pier Paolo Capra, INRiM, Italy
Prof. Dr. Gianluca Ghigo, Politecnico di Torino, Italy
Dr. Ing. Iulian Mihai, WIKA Italia Srl, Italy

Politecnico di Torino
July 1, 2019

I hereby declare that, the contents and organisation of this dissertation constitute my own original work and does not compromise in any way the rights of third parties, including those relating to the security of personal data.

. . . .

Paolo Durandetto
Turin, July 1, 2019

Summary

Superconducting devices based on Josephson effect are worldwide employed as primary dc voltage standards in National Metrology Institutes (NMIs). Nowadays, research on Josephson voltage standards (JVSs) is aiming at a fundamental change also in the metrology of ac and arbitrary signals: binary-divided programmable standards (PJVS) that convert a digital code into a quantum-based stepwise waveform are already available in primary laboratories, whereas more advanced standards for converting streams of sub-nanosecond pulses into very pure arbitrary signals are now actively developed. Furthermore, a user-friendly and liquid helium-free refrigeration system with adequate cooling power and minimum temperature below 4 K is favorable to the spread of these quantum standards outside NMIs. Commercially-available Gifford-McMahon (GM) and pulse-tube (PT) cryocoolers satisfy these needs, though some collateral effects related to the high-vacuum environment and to the cyclic thermal noise are to be faced.

The dynamical thermal response of a GM cryocooler to programmed power stimuli has been experimentally studied, considering it as a linear system around 4 K. Its power-to-temperature transfer function has been then evaluated via two independent methods, providing comparable results useful to the analysis of cryocoolers behavior and to the development of techniques for actively and passively damp the temperature fluctuations.

The other major downside of cryocoolers is the difficulty of transferring the power generated within the Josephson chip to the cryocooler cold surface, which may cause the detrimental warming of the junctions. With the aim of enhancing heat dissipation of cryocooled PJVS devices, a special cryopackage has been realized and tested in different experimental conditions, with the chip integrated into a sandwich structure with low thermal resistance materials subject to a reproducible mechanical pressure. This cryopackage succeeded in dissipating hundreds of mW of power with a minor increase of the chip temperature.

Subsequently, in order to analyze the electrical properties of a PJVS array, an open-source software has been written. It allows to control the bias currents flowing into the PJVS binary segments and synthesize dc and ac quantum-accurate voltages. The code, publicly shared on *GitHub*, is modular and easily expandable with the support of many libraries, thus allowing prompt reconfiguration for different

experimental needs.

PJVS arrays with 8192 junctions have been electrically characterized in cryocooler and used to synthesize stepwise sine waves with amplitudes up to 2 V and frequencies up to the kHz range, though limited by the cryocooler thermal fluctuations and by frequent magnetic flux trapping events. In addition, the possibility of advantageously operating a binary PJVS array with a reduced number of bias lines was investigated. This feature can be achieved by simultaneously exploiting first and second quantum voltage steps, along with non-conventional codifications. Two newly devised bias techniques are described in detail and preliminary experimental tests on waveform synthesis are presented.

Cryocooler operation of pulse-driven Josephson devices fabricated at Physikalisch-Technische Bundesanstalt (PTB) has been investigated as well. In contrast with PJVS, these have to satisfy less stringent requirements in terms of power dissipation. On the other side, the rigid coaxial cable for the broadband high-frequency pulse transmission introduces a considerable thermal load to the cryocooler cold stage, which has been substantially reduced by means of proper thermal anchorings. Electrical characterization of pulse-driven arrays in cryocooler showed similar results of measurements in liquid helium. In particular, quantum step widths larger than 1 mA have been observed under constant pulse repetition frequencies around 6 GHz.

Afterward, $\Sigma\Delta$ modulation has been exploited to synthesize unipolar and bipolar sine waves with pulse-driven arrays at amplitudes ranging up to tens of mV, frequencies in the kHz range and higher harmonics suppressed by more than 80 dBc. Nevertheless, further studies are required to check degree of quantization and spectral purity with better resolution, especially at signal frequencies approaching the MHz range.

Finally, ac JVSs have been operated at metrological level during a three-month research period at PTB, funded by the European project ACQ-PRO. PJVS-PJVS and JAWS-PJVS indirect comparisons have been carried out via the calibration of semiconductor-based voltage generators at amplitudes and frequencies used in industry and scientific research. Relative differences at the µV/V level in the former case and more than 5 µV/V in the latter have been achieved, and the possible sources of the discrepancies are discussed.

Acknowledgements

Part of the work presented in this dissertation was co-funded by the European Union within the following EURAMET Joint Research Projects:

- EMRP SIB59 Q-WAVE: “A quantum standard for sampled electrical measurements”
- EMPIR 15SIB04 QuADC: “Waveform metrology based on spectrally pure Josephson voltages”
- EMPIR 14RPT01 ACQ-PRO: “Towards the propagation of ac quantum voltage standards”
- EMPIR 17RPT03 DIG-AC: “A digital traceability chain for AC voltage and current”

The EMPIR initiative is co-funded by the European Unions Horizon 2020 research and innovation programme and the EMPIR Participating States. The EMRP is jointly funded by the EMRP participating countries within EURAMET and the European Union.

I also gratefully acknowledge the contribution of the following colleagues:

- Andrea Sosso and Eugenio Monticone, for everything that concerns their role as supervisors;
- Danilo Serazio and Fulvio Francone, for designing and manufacturing some mechanical parts of the cryogenic apparatuses;
- Vincenzo Lacquaniti, Natascia De Leo and Matteo Fretto, for providing the PJVS devices;
- Bruno Trinchera, for actively participating in both experimental measurements and data analysis and for kindly providing parts of the measurement setups;
- Marco Lanzillotti, for the technical support in ac-dc measurements;

- Ralf Behr, Oliver Kieler and Johannes Kohlmann from PTB, for providing the JAWS devices, the pulse pattern generator and relative ΣΔ codes;

- Martin Bauer, Jonas Herick, Oliver Kieler and Ralf Behr from PTB, for supervising and supporting the activities conducted during my research period at PTB, presented in Chapter 7.

Contents

List of Tables

List of Figures

Glossary

2-DEG	bidimensional electronic gas. 21
ADC	analog-to-digital converter. 35, 123, 124
AIST	Advanced Industrial Science and Technology. 38
AWG	arbitrary waveform generator. xii, xiv, xv, 36, 44, 45, 64, 65, 83–86, 88–91, 99, 101, 102, 112, 113, 122–125, 127, 128, 136
BCS	Bardeen, Schrieffer and Cooper. 8–10
BIPM	Bureau International des Poids et Mesures. 20
CCE	Consultative Committee for Electricity. 26
CGPM	General Conference on Weights and Measures. 26
CIPM	International Committee for Weights and Measures. 26
CODATA	Committee on Data for Science and Technology. 13
CPS	coplanar stripline. 17
CPW	coplanar waveguide. 17, 39, 43, 44, 105–107
CSIRO	Commonwealth Scientific and Industrial Research Organisation. 1
CW	continuous wave. xv, 109–112, 114, 118
DAC	digital-to-analog converter. 20, 33, 34, 73, 95, 132
DUT	device under test. xvi, xvii, 46, 47, 115, 116, 122, 125–128, 130, 131
DVM	digital voltmeter. 35
emf	electromotive force. 1–4, 30
EMI	electromagnetic interference. 20, 49, 52, 131
EMPIR	European Metrology Programme for Innovation and Research. v, xxiv, 121, 132

EMRP	European Metrology Research Programme. v
EURAMET	European Association of National Metrology Institutes. v, 84, 105
FET	field-effect transistor. 24
FFT	Fast Fourier Transform. xvi, 113–116, 124, 129
GM	Gifford-McMahon. iii, xii, xiii, xv, xxiii, 52–55, 61, 63, 64, 71, 75, 92, 106, 107, 135, 136
GUI	Graphic User Interface. xiv, 88–91
HTS	high critical temperature superconductor. 9, 17
INRiM	Istituto Nazionale di Ricerca Metrologica. i, viii, ix, xxiii, 39, 73–76, 78, 80, 82, 84, 86, 88, 90, 92, 94, 96, 98, 100, 102, 103, 105, 106, 108, 110, 112, 114, 116, 118, 121
JAWS	Josephson arbitrary waveform synthesizer. iv, vi, viii, ix, xv–xvii, xxiv, 30, 42–47, 105–119, 124, 125, 128–132, 136, 137
JVS	Josephson voltage standard. iii, iv, xii, xxiii, 19, 20, 30, 33, 35, 39–43, 49, 59, 74
LCIE	Laboratoire Central des Industries Électriques. 1
LHe	liquid helium. xv, 46, 50, 59, 99, 105, 106, 108–110, 118, 121, 122, 124, 136
LNE	Laboratoire National de Métrologie et d'Essais. 1
LSB	least-significant-bit. 34, 102
MEMS	micro-electro-mechanical system. 32
MJTC	multi-junction thermal converter. xii, 31–33
MSB	most-significant-bit. x, 96, 97
MSDN	Microsoft Developer Network. 91
NBS	National Bureau of Standards. 1, 16
NIST	National Institute of Standards and Technology. 2, 29, 34, 38, 40, 42, 44–46, 77, 78
NMI	National Metrology Institute. iii, xxiii, 5, 20, 22, 32, 34, 74, 121
NMIA	National Measurement Institute of Australia. 1
NPL	National Physical Laboratory. 122, 123

NPLC	number of power line cycles. 88, 91
NRZ	non-return-to-zero. 42, 110, 114
OFHC	oxygen-free high conductivity. 59, 63, 75, 92, 106
OSR	oversampling ratio. 41, 125
PCB	printed circuit board. 105, 106
PDWQ	präzise doppelwellenform quelle. ix, xvii, 125, 127–129, 131–133
PID	proportional-integrative-differential. 58, 77, 108
PJVS	programmable Josephson voltage standard. iii–v, viii–x, xii–xvi, xxiv, 29, 33–40, 42, 43, 73–79, 81, 83–85, 87–103, 106, 121–123, 133, 135–137
PPG	pulse pattern generator. xv, 40, 42–47, 109, 110, 112, 114, 124, 125, 128, 136
PT	pulse-tube. iii, xii–xiv, 52, 55–57, 92
PTB	Physikalisch-Technische Bundesanstalt. iv, vi, ix, xii, xxiii, xxiv, 1, 16, 32, 38, 39, 42, 45, 73, 105, 110, 112, 121–124, 126, 128, 130, 132, 136
QMT	quantum metrology triangle. 24, 25, 35
QVM	quantum voltmeter. ix, xvi, 35, 121–123, 125–128, 131, 132
QVNS	quantum voltage noise source. 43
RCSJ	resistively-capacitively shunted junction. 13, 40
rms	root-mean-square. xvi, xvii, 30–32, 34, 35, 45, 46, 114–116, 123, 125, 127–131, 133
RZ	return-to-zero. 40, 109, 110, 114, 124
SET	single-electron transport. 22–25
SI	International System of units. vii, xxiii, 1, 25–27
Si-MOSFET	silicon metal-oxide field-effect transistor. 21
SINIS	superconductor/insulator/normal metal/insulator/superconductor. 15, 16, 38
SIS	superconductor/insulator/superconductor. 15, 16, 19, 29, 30, 37–40, 74
SJTC	single-junction thermal converter. xii, 31
SMA	SubMiniature version A. 105, 107, 113
SMD	surface mount device. xiii, 63–65

SNIS	superconductor/normal metal/insulator/superconductor. xiii, 15, 16, 39, 73, 103, 136
SNR	signal-to-noise ratio. 64, 65
SNS	superconductor/normal metal/superconductor. 15, 16, 37, 38, 118, 136
SQUID	Superconducting Quantum Interference Device. 9
TTS	thermal transfer standard. xvi, 32, 33, 43, 116–119
TVC	thermal voltage converter. 30, 31, 33, 35, 43

Preface

Following the great success of Josephson standards for the dc volt representation, two different kinds of ac quantum voltage references have been developed, namely programmable and pulse-driven Josephson devices, to replace conventional calorimetric techniques, based on ac-dc transfer and, as such, not intrinsically accurate. Being Josephson junctions made of conventional superconductors, these need to be operated at cryogenic temperatures well below 10 K, typically achieved with liquid helium bath. The necessity of dealing with liquid cryogens significantly complicates the use of superconducting standards, thus strongly limiting their spread outside National Metrology Institutes (NMIs). However, mechanical refrigerators are becoming increasingly important as a user-friendly and safe alternative to the potentially hazardous coolants, though other critical issues arise.

The latest activities carried out at INRiM in this scope are presented in this dissertation. In addition, a final chapter is entirely dedicated to the metrological application of JVSs at PTB, based on liquid helium cooling systems.

Chapter 1 gives an historical overview of the dc volt, from its definition to its realization in the current International System of units (SI), from the previously employed chemically and electronically-based implementations (e.g. Weston cells and Zener references) to its present quantum-based *representation* through Josephson standards. For completeness, quantum standards for electrical resistance and current are shortly presented, with particular attention to the incoming redefinition of the SI, which will definitely take effect on 20 May 2019.

A thorough description of programmable and pulse-driven ac Josephson voltage standards is given in Chapter 2: principle of operation, state-of-the-art, strengths, weaknesses, and future objectives are extensively illustrated. A brief section on conventional ac-dc thermal transfer techniques is also present.

A whole chapter (Chapter 3) is dedicated to the fundamental issues of cryogenic refrigeration, with special focus on cryogen-free cooling systems. Cryocoolers suitable to reach temperatures below 4 K are presented, highlighting both advantages and disadvantages resulting from their use. In the perspective of getting rid of one of the most deleterious side-effects, namely the temperature oscillations on the cold stage, an intensive experimental investigation of the thermal behavior of a two-stage GM cooler has been carried out and is presented in Chapter 4.

Concerning programmable Josephson voltage standards (PJVSs), Chapter 5 describes the activities carried out for their proper cryogen-free refrigeration and electrical polarization. Furthermore, new unconventional bias modes have been investigated.

The following chapter (Chapter 6) is focused on the operation of pulse-driven Josephson arrays, also known as Josephson arbitrary waveform synthesizers (JAWSs). As with PJVS, their use in a cryocooled environment has been studied via electrical characterization and waveform synthesis.

In conclusion, the application of both PJVS and JAWS systems for the calibration of conventional ac voltage generators is presented in the last chapter (Chapter 7), which describes the activities carried out during my stay at PTB in Braunschweig (Germany) within the Josephson effect working group, following the award of a Researcher Mobility Grant in the scope of the ACQ-PRO EMPIR project.

Chapter 1

The volt and electrical units: the route towards SI quantum standards

The volt (V) is the unit of electromotive force (emf) or electric potential difference in the International System of units (SI) [1]. It is a derived unit, defined as *"the potential difference between two points of a conducting wire carrying a constant current of one ampere, when the power dissipated between these points is equal to one watt"*. In contrast to the definition, the practical realization of a unit is always bound to a physical experiment with an uncertainty larger than zero [2]. Yet, as will be discussed in the following, to put rigorously into practice the volt definition is not a simple task.

1.1 The SI volt realization

The SI volt has been realized by means of the so-called *voltage balance* [3], basically an electrostatic voltage-to-force converter where the electrical energy of a capacitor charged to a voltage V and the gravitational potential energy of a mass m are compared. A schematic representation of the voltage balance is shown in Fig. 1.1 [4]. By vertically shifting one of the electrodes of a distance Δz, the energy stored in the capacitor changes by an amount of $\Delta W_e = -1/2\, V^2\, \Delta C$, where ΔC is the capacitance variation, traceable to the SI via a calculable-capacitor [5]. At the same time, the corresponding change in mechanical energy is $\Delta W_m = m\, g\, \Delta z$. Assuming the equality between electrical and mechanical energy, then $\Delta W_e = \Delta W_m$ and the voltage can be calculated directly in SI units with a relative uncertainty of a few parts in 10^7 [6].

In the eighties of the last century, five voltage balances had been in operation at LCIE (now LNE, France), CSIRO (now NMIA, Australia), PTB (Germany), NBS

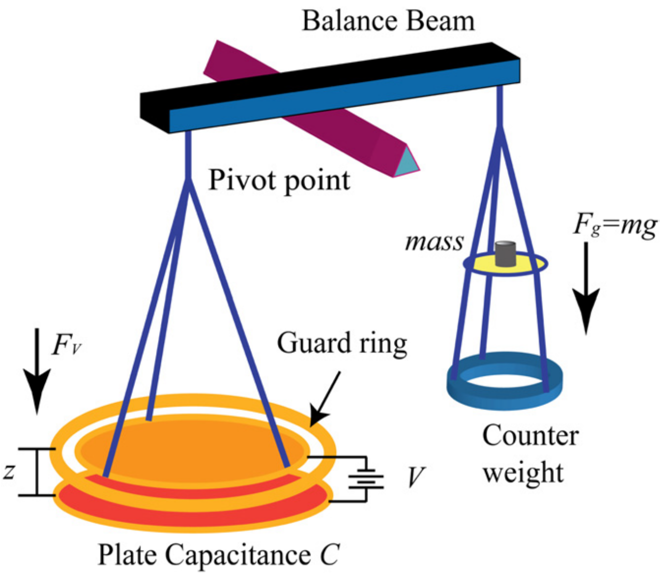

Figure 1.1: Schematic representation of a voltage balance [4]. © 2012 IOP Publishing

(now NIST, United States) and University of Zagreb (Croatia), and mainly differed for the employed voltage-to-force transducer. The major drawback of voltage balances derives from the need of large and heavy electrodes supplying voltages in the kilovolt range. Indeed, owing to the large inertial mass of the electrodes, only small mass references of about a gram could be balanced [4]. Nowadays voltage balances are no longer in operation because their uncertainties are by one order of magnitude larger that those achieved with watt balances [2].

1.2 Reproduction of the dc volt

Since practical realizations of electrical units are complex and time-consuming, they are generally *reproduced* by means of a highly reproducible measurement standard based on a physical phenomenon [7]. Before the discovery of the Josephson effect, the dc volt was reproduced and maintained by Weston cells and Zener references.

1.2.1 Weston cell

Between 1911 and 1990, the international standard for the volt was based on the open-circuit emf of saturated Weston cells [8]. Invented by the English chemist Edward G. Weston in 1893, Weston cells consist of a low-potential electrode (anode) made up by a 12.5% amalgam of cadmium with mercury and a high-potential

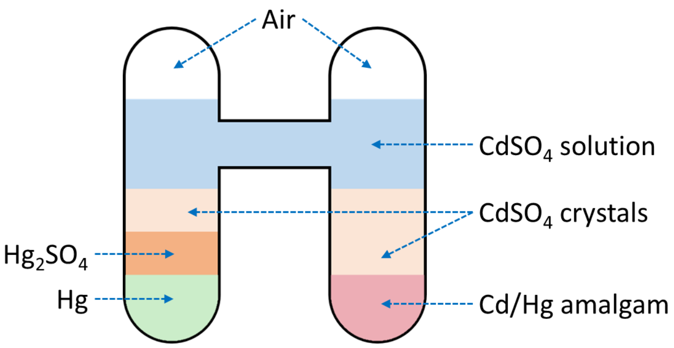

Figure 1.2: Schematics of a Weston cell.

electrode (cathode) of pure liquid mercury. As depicted in Fig. 1.2, these are placed into the arms of an H-shaped glass cell to make contact with platinum wires sealed in the glass at the bottom of each leg. The electrodes are immersed in a saturated solution of cadmium sulfate ($CdSO_4$) acting as electrolyte and separated from the electrodes by a layer of $CdSO_4$ crystals. The electrochemical reactions of the cell are oxidation of cadmium on the anode and reduction of Hg_2^{2+}on the cathode.
The reaction on the anode is

$$\mathrm{Cd}\,(l) \longrightarrow \mathrm{Cd}^{2+}(aq) + 2\,\mathrm{e}^-$$

while the reaction at the cathode is

$$\mathrm{Hg_2SO_4}(s) + 2\,\mathrm{e}^- \longrightarrow 2\,\mathrm{Hg}(l) + \mathrm{SO_4}^{2-}\,(aq)$$

The nominal potential of the saturated cell at $T = 20\,°\mathrm{C}$ is $E_{20} = 1.018\,636\,\mathrm{V}$. It is very stable and varies only slightly with temperature: this variation was determined between 0 °C and 40 °C by the empirical formula

$$\begin{aligned} &E_T = E_{20} - a\,(T-20) - b\,(T-20)^2 + c\,(T-20)^3 \\ &a = 40.6 \times 10^{-6}\,\mathrm{V/°C} \\ &b = 9.5 \times 10^{-7}\,\mathrm{V/°C^2} \\ &c = 10^{-8}\,\mathrm{V/°C^3} \end{aligned} \tag{1.1}$$

Calculated from Eq. 1.1, a 1 °C increase with respect to the 20 °C temperature point leads to an emf variation of $-41.55\,\mu\mathrm{V}$.

The saturated Weston cells have a relatively high internal resistance, ranging from 200 to 1200 Ω. They exhibit very low noise ($4\,\mathrm{nV}/\sqrt{\mathrm{Hz}}$) and long-term stability up to 10^{-7} per year. Nevertheless, they must handled with extreme care, being sensitive to shock and vibration [2].

Differently from the saturated one, the unsaturated Weston cells exhibit a lower temperature coefficient ($-10\,\mu\mathrm{V\,K^{-1}}$) and are resistant to shocks. However, the emf long-terms stability is much worse (up to $300\,\mu\mathrm{V}$ per year), therefore they had to be periodically re-calibrated [9].

1.2.2 Zener voltage reference

Solid-state standards are particular sources that supply a stable dc voltage at their output. Generally, these exploit the properties of Zener diodes, hence the name *Zener voltage references* or simply *Zeners*, and were developed to replace traditional Weston cells.

Zeners are highly-doped silicon diodes that, unlike rectifiers, are operated in the reverse-bias mode. When a generic diode is biased at sufficiently high negative voltages, breakdown phenomena occur, whereby the inverse current flowing across the p-n junction greatly increases for small voltage increments in a wide range of values (the *breakdown region*, Fig. 1.3). Avalanche multiplication and Zener effect are the two processes which produce the breakdown [10], though the term Zener is used independently on the causing mechanism. When operated in the breakdown

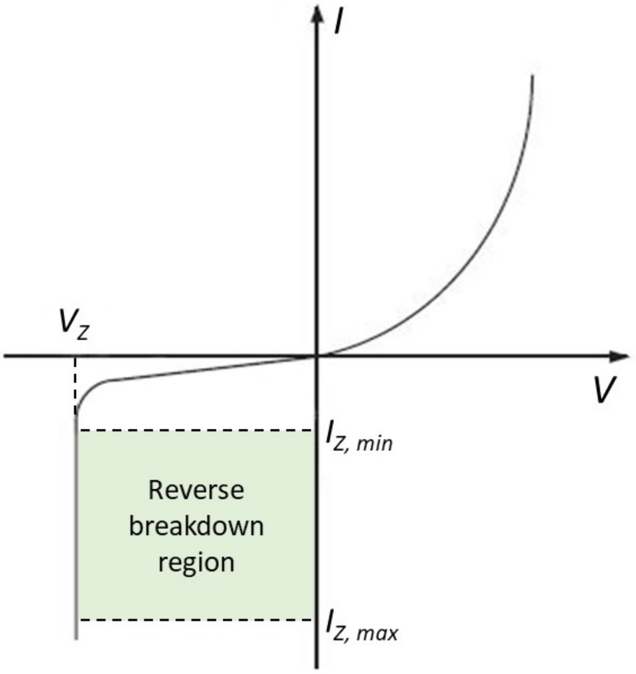

Figure 1.3: Current-voltage characteristic of a Zener diode.

region, Zeners generate a dc voltage V_Z that is ideally independent on the bias current I_Z and that can be used, for example, to stabilize, regulate and limit the voltage drop across a load resistor in electronic circuits. A fundamental parameter that characterizes a Zener diode is the dynamic resistance of the breakdown region, given by

$$r_Z = \frac{dV_Z}{dI_Z} \tag{1.2}$$

Ideally $r_Z = 0$, however, real Zeners exhibit r_Z values of some tens of ohms for V_Z around 10 V [10].

Zener diodes are the essential element of commercialized small and easily transportable instruments [11] that exhibit time stability around 10^{-6} per year for the 10 V output and thermal coefficient lower than $10^{-4}\,\mathrm{K}^{-1}$. By carefully controlling the environmental conditions (temperature, pressure, and humidity) and by modeling the temporal drift, output voltages can be predicted over periods of several weeks to within some parts in 10^{-8}. Eventually, the uncertainty of such Zener references is limited to about 10^{-9} by $1/f$ noise, for which corrections cannot be applied [12].

Though Zener voltage references exhibit higher noise characteristics than Weston cells and are affected by the environmental conditions, they are widely used in many calibration laboratories because of their robust transportability [13]. Before the advent of Josephson voltage standards, they were employed in NMIs as primary standards for the representation of the dc volt, whereas nowadays they are used to maintain the traceability chain to the more accurate primary Josephson standards at 1.018 V and 10 V.

1.3 Towards a dc quantum voltage standard

Before deepening into quantum voltage standards, basic concepts of superconductivity and a detailed description of the Josephson effect are given as follows.

1.3.1 Basics of superconductivity

Superconductivity is a macroscopic quantum phenomenon that occurs in some specific materials (typically metals and metallic alloys) at low temperatures. It has been discovered by Heike Kamerlingh Onnes in 1911 [14], three years after his success in liquefying helium (^{4}He) at 4.2 K: he indeed exploited liquid helium as cooling agent for studying the electrical properties of various materials at low temperatures. He noted that the electrical resistance of different metals as mercury (Hg), lead (Pb) and tin (Sn) abruptly fell to zero below a characteristic temperature [15] specific for each material. This temperature is known as *critical temperature*

(T_c) of the superconductor and represents the transition temperature between normal and superconducting state.

The zero-resistance state is evident by noting that persistent currents in superconducting closed loops can flow for years without any appreciable decay, meaning that no dissipation energy due to a resistance occurs. Moreover, superconductivity can exist only when electrical current densities are lower than a characteristic value J_c, named *critical current density*, different for each material and temperature dependent. However, *perfect conductivity* is not the only hallmark of the superconducting state: the other important feature is *perfect diamagnetism*, discovered by Meissner and Ochsenfeld in 1933 [16]. It provides that weak magnetic fields B cannot penetrate superconductors, even in the case the material in its normal state is first crossed by magnetic field lines and then cooled down below T_c: magnetic field lines will be expelled from the interior of superconductors, leaving $B = 0$ in the inside. Meissner-Ochsenfeld effect cannot be deduced simply by imposing zero-resistance, so it is a separated phenomenon that identifies superconductivity.

For each superconductor it exists also a *critical magnetic field* H_c that breaks down superconductivity and makes the material transit back to the normal state. The effects of magnetic field on superconductors bring to the idea of separation of superconducting materials in two main classes [17]: *type I* and *type II* superconductors, as proposed in 1957 by Abrikosov [18], for which he won the Nobel prize in 2003. In type I superconductors there exists a single critical field H_c above which superconductivity is completely destroyed. The critical magnetic field H_c depends on temperature T through the empirical parabolic relation (displayed in Fig. 1.4, right):

$$H_c(T) \simeq H_c(0)\left[1-\left(\frac{T}{T_c}\right)^2\right] \tag{1.3}$$

Differently, in type II superconductors two different critical fields H_{c1} and H_{c2} exist, with $H_{c1} < H_{c2}$. In this case, the complete expulsion of the magnetic field from the

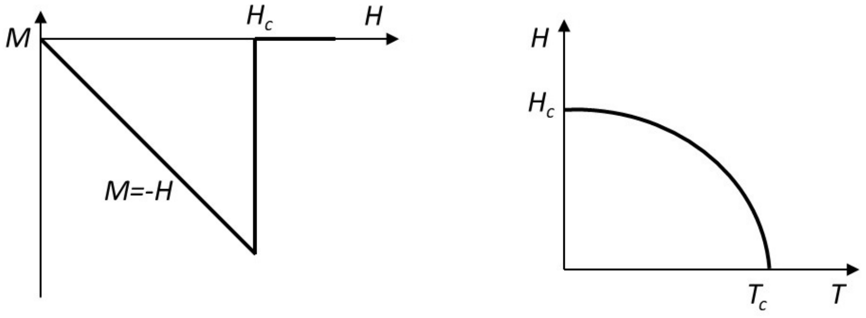

Figure 1.4: Type I superconductors. Left: magnetization vector M as a function of the applied field H. Right: $H-T$ phase diagram showing the Meissner state for $H < H_c$.

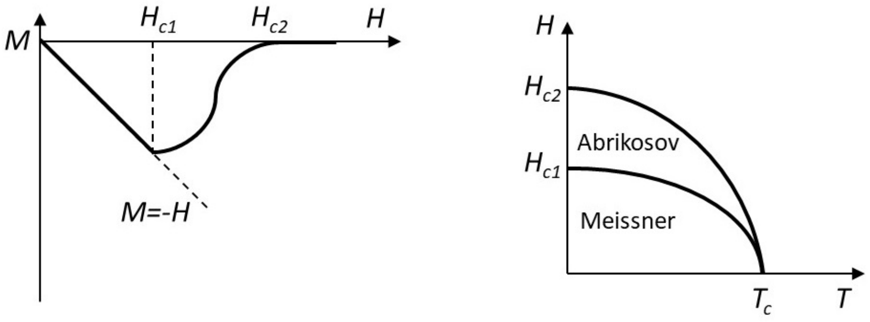

Figure 1.5: Type II superconductors. Left: magnetization vector M as a function of the applied field H. Right: $H - T$ phase diagram showing the Meissner state for $H < H_{c1}$ and the Abrikosov state for $H_{c1} < H < H_{c2}$.

superconductor occurs only for $H < H_{c1}$, whereas for $H_{c1} \leq H \leq H_{c2}$ it stays in a mixed state (Abrikosov state) where magnetic field lines are partially trapped into the material in the form of vortex lattice. Above H_{c2} superconductivity completely disappears. Type I superconductors are pure elements (Hg, Pb, Sn, etc.), apart from niobium (Nb), vanadium (V) and technetium (Tc) that are type II superconductors. Alloys and impure metals are type II superconductors as well [19].

The first theory describing superconductivity was developed by Fritz and Heinz London in 1935 [20]: resembling the two-fluid model of superfluidity, they assumed that, below T_c, a constant fraction of the conduction electrons n_s, named *superelectrons*, can flow without any dissipation, whilst the rest of the electrons stay in the normal state and move with a finite resistance. Applying classical laws of electrodynamics they formulated the London equation (Eq. 1.4), which relates the supercurrent density $\vec{J_s}$ to the electromagnetic field through the vector potential $\vec{A}$:

$$\vec{J_s} = -\frac{(e^*)^2\, n_s}{m^*}\vec{A} \tag{1.4}$$

where e^* and m^* are charge and mass of the superelectron, respectively. The most important consequence of London equation is the explanation of Meissner effect. Indeed, starting from Eq. 1.4 it is easy to show that the magnetic field B in a superconductor undergoes an exponential decay having characteristic length λ_L, named London penetration depth [17] and given by

$$\lambda_L = \left(\frac{m^*}{\mu_0\, n_s\, (e^*)^2}\right)^{-1} \tag{1.5}$$

Following London theory, the first quantum, but still phenomenological, theory of superconductivity was developed by Ginzburg and Landau in 1950 [21] and is based on the theory of second-order phase transitions [22]. The second-order transition from the normal to the superconducting state is characterized by a complex order parameter Ψ that is related to the density of superelectrons: it is equal to zero above T_c, and can be thought as the wave function of the superconducting electrons. Since Ginzburg-Landau theory is a direct evolution of London theory, it is able to predict Meissner effect, but is also capable of describing other important superconducting phenomena as magnetic flux quantization, the Abrikosov vortex lattice in type II superconductors and proximity effect [17].

The first truly fundamental theory of superconductors was developed by Bardeen, Schrieffer and Cooper (BCS) in 1957 [23][24], for which they have been awarded with the Nobel prize in 1972. BCS theory postulates the existence of the so-called Cooper pairs, quasiparticles made up by two weakly coupled electrons at the Fermi level having opposite spin and momentum and a total charge equal to $-2e$, being e the elementary charge. These zero spin pairs obey the Bose-Einstein statistics and, hence, can occupy the lowest energy state at low temperatures [25]. As a consequence, the wave functions of the single pairs are strongly overlapping and form a coherent quantum state described by a single macroscopic wave function $\Psi = \sqrt{\rho_s}\, e^{i\theta}$, with ρ_s the Cooper pairs density and θ the phase of the macroscopic wave function. It is evident how this wave function is strictly correlated to the Ginzburg-Landau order parameter and to the density of superelectrons of London theory, clearly showing the analogy between London superelectrons and Cooper pairs. From the classical point of view, the attractive force that binds two electrons together in a Cooper pair is due to instantaneous electron-phonon interactions, which overcome the electric repulsion of the electrons. However, it has to be noted that BCS theory is independent of the nature of the attractive force between the electrons.

The most important parameter that emerges from BCS theory is the superconducting energy gap Δ, which represents half of the energy required for breaking up a Cooper pair into two single electrons. The superconducting energy gap depends upon temperature according to the trend shown in Fig. 1.6 and, as easily predictable, its value at T_c is equal to zero [17]. Both T_c and Δ depend on material properties such as phonon spectrum, electronic density of states and electron-ion

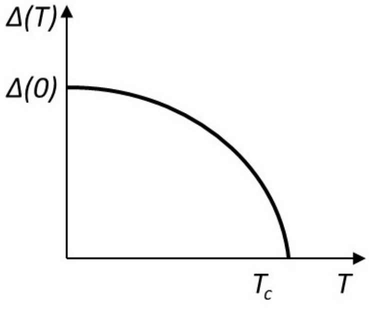

Figure 1.6: Superconducting energy gap Δ as a function of temperature T.

coupling strength [26]. However, it is possible to obtain some thermodynamic ratios that are universal, since they are independent on the involved material, as

$$\frac{2\Delta(0)}{T_c} = 3.52\,k \tag{1.6}$$

where $\Delta(0)$ is the superconducting energy gap at $0\,\mathrm{K}$ and k is the Boltzmann constant.

Despite its great success, BCS theory predicts a maximum critical temperature of about 30 K, that is confuted by the experimental findings. It is then not able to explain the behavior of high critical temperature superconductors (HTSs), better described by Ginzburg-Landau theory [27].

Quantum metrology exploits some of the astonishing properties of superconducting materials, namely Josephson effect for voltage metrology and flux quantization for magnetic field measurements [28]. A detailed description of the former is presented in Sec. 1.3.2, since the application of Josephson devices represents the central subject of this dissertation.

Magnetic flux quantization

The magnetic flux threading a closed loop lying in a bulk superconductor cannot assume arbitrary values; rather it has to be an integer multiple of the *magnetic flux quantum* Φ_0 [25], given by

$$\Phi_0 = \frac{h}{2e} \simeq 2.07 \times 10^{-15}\,\mathrm{Wb} \tag{1.7}$$

Hence, magnetic flux quantum Φ_0 is expressed by a combination of two fundamental constants: the elementary charge e and the Planck constant h. Along with the Josephson effect, magnetic flux quantization represents the basis for the operation of a very sensitive magnetometer: the Superconducting Quantum Interference Device (SQUID) [29]. SQUIDs give rise to an output voltage signal that is a periodic with the flux threading a superconducting loop in which one or two Josephson junctions are inserted. The minimum flux variation they can measure is of the order of fractions of Φ_0 [30].

1.3.2 The Josephson effect

The Josephson effect is a macroscopic quantum phenomenon theoretically predicted by Brian D. Josephson in 1962 [31] and experimentally observed one year later by Anderson and Rowell [32]. For this prediction Josephson received the Nobel prize in Physics in 1973.

Josephson effect states that zero-resistance quantum tunneling of Cooper pairs can occur between two weakly coupled superconductors. This weak coupling can be achieved in special devices, named *Josephson junctions*, made up by two superconducting electrodes separated by a thin barrier ($\sim 10\,\mathrm{nm}$) of non-superconducting material. Josephson junctions exhibit some remarkable features, which are described below.

1.3.3 Josephson equations

In order to derive the characteristic equations of a Josephson junction, several approaches are possible. Here the easiest and effective way proposed by Richard Feynman is presented [33].

Suppose we have two superconducting elements (S_L and S_R) separated by a thin layer of an insulating material (I), as shown in Fig. 1.7, with Ψ_L and Ψ_R defined as the macroscopic wavefunctions of the superconducting state of the left and the right electrodes, respectively. Quantum tunneling of Cooper pairs results to be possible because the barrier is thin enough to allow the two wavefunctions to exceed on the other superconductor and then to be overlapped in proximity of the barrier. The dynamics of Ψ_L and Ψ_R is then defined by the following coupled Schrödinger equations:

$$\begin{aligned} i\hbar\frac{\partial \Psi_L}{\partial t} &= E_L\,\Psi_L + K\,\Psi_R \\ i\hbar\frac{\partial \Psi_R}{\partial t} &= E_R\,\Psi_R + K\,\Psi_L \end{aligned} \tag{1.8}$$

where E_L and E_R are the ground state energies of the superconductors and K is the coupling amplitude, which gives a measure of the interactions between S_L and S_R [30]. As anticipated in Sec. 1.3.1, BCS theory allows to express the superconducting

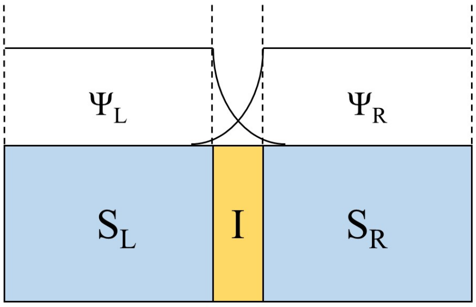

Figure 1.7: Schematic representation of a Josephson junction: two superconducting electrodes S_L and S_R are separated by a thin layer of insulating material (I). More details are given in the text.

wavefunctions as:

$$\begin{aligned} \Psi_L &= \sqrt{\rho_L}\, e^{i\theta_L} \\ \Psi_R &= \sqrt{\rho_R}\, e^{i\theta_R} \end{aligned} \tag{1.9}$$

Substituting Eqs. 1.9 into Eqs. 1.8 and applying simple algebraic manipulations we obtain:

$$\begin{aligned} \hbar\,\frac{\partial \rho_L}{\partial t} &= -\hbar\,\frac{\partial \rho_R}{\partial t} = 2K\sqrt{\rho_L\,\rho_R}\,\sin(\theta_R - \theta_L) \\ -\hbar\,\frac{\partial(\theta_L - \theta_R)}{\partial t} &= E_R - E_L \end{aligned} \tag{1.10}$$

When a constant voltage V is applied across the Josephson junction, the two energy levels E_L and E_R are shifted such that $E_L - E_R = 2e\,V$. Moreover, expressing the Cooper pairs current density as $J_s = \partial\rho_L/\partial t = -\partial\rho_R/\partial t$, Eqs. 1.10 become:

$$\begin{aligned} J_s &= J_c \sin\varphi \\ \frac{\partial\varphi}{\partial t} &= \frac{2e\,V}{\hbar} \end{aligned} \tag{1.11}$$

where $\varphi = \theta_L - \theta_R$ is the phase difference between the two superconductors and

$$J_c = \frac{2K}{\hbar}\sqrt{\rho_L\,\rho_R} \tag{1.12}$$

is the critical current density, which is a function of junction geometry, temperature and magnetic field. Combining the two Josephson equations (Eqs. 1.11), the following relation for the tunneling Cooper pairs current $I_s = J_s\,A$, with A the junction area, is obtained:

$$I_s(t) = I_c\,\sin\left(\frac{2e}{\hbar}\int_0^t V(\tau)\,d\tau + \varphi_0\right) \tag{1.13}$$

with $I_c = J_c\,A$ the junction critical current.

1.3.4 Dc and ac Josephson effect

Eqs. 1.11 represent the constitutive equations of the Josephson effect. It can be noted that, in the case of $V = 0$, the phase φ does not vary with time and a constant supercurrent density J_s can flow across the junction without any voltage drop. The critical current density J_c represents the maximum density of Cooper pairs that can tunnel the barrier with no electrical resistance. This is the essence of the so-called *dc Josephson effect*.

On the other hand, when a constant voltage $V \neq 0$ is applied to the junction, the phase difference φ varies linearly on time and an oscillating supercurrent given by

$$I_s = I_c\,\sin\left(\varphi_0 + \frac{2e\,V}{\hbar}t\right) \tag{1.14}$$

flows through the junction at a frequency $f_J = 2e\,V/h = V/\Phi_0$. This is the *ac Josephson effect*. Owing to the high frequency and the low amplitude, this ac signal is difficult to be directly observed [34].

Both dc and ac driving sources

Concerning Josephson standards for voltage metrology applications, the most important operating mode manifests when junctions are driven by both a dc and an ac voltage biases, as

$$V(t) = V_{dc} + V_{ac}\,\sin(\omega_{ac}\,t) \tag{1.15}$$

where V_{dc} and V_{ac} are dc and ac components amplitudes and ω_{ac} is the angular frequency of the ac component. Combining Eqs. 1.13 and 1.15, the Josephson current I_J becomes

$$I_s(t) = I_c\,\sin\left(\varphi_0 + 2\pi\,\frac{V_{dc}}{\Phi_0}\,t + 2\pi\,\frac{V_{ac}}{\omega_{ac}\,\Phi_0}\,\sin\left(\omega_{ac}\,t\right)\right) \tag{1.16}$$

It can be seen that the frequency of the Josephson current is a superposition of the constant frequency $\omega_{dc} = V_{dc}/\Phi_0$ and a sinusoidally varying term. Therefore, the supercurrent frequency is not the same as that of the driving ac voltage source. The reason is the non-linearity of the current-phase relation (Eq. 1.14), which allows the coupling of different frequencies with the driving frequency ω_{ac}. Expanding Eq. 1.16 in terms of Fourier series one can find

$$I_s(t) = I_c\sum_{n=-\infty}^{+\infty}(-1)^n\,J_n\left(2\pi\,\frac{V_{ac}}{\omega_{ac}\,\Phi_0}\right)\sin\left[(\omega_{dc} - n\,\omega_{ac})t + \varphi_0\right] \tag{1.17}$$

where J_n is the n^{th} order Bessel function of first kind. A current response where the frequency ω_{dc} couples to multiples of the driving frequency ω_{ac} is obtained. Eq. 1.17 shows that the Josephson junction carries a dc supercurrent whenever $\omega_{dc} - n\,\omega_{ac} = 0$, that means

$$V_n = n\,\frac{h}{2e}\,f_{ac} = n\,\Phi_0\,f_{ac} \tag{1.18}$$

where n represents the number of flux quanta Φ_0 transferred across the junction during each cycle of $f_{ac} = \omega_{ac}/2\pi$. The averaged discrete voltages V_n are called Shapiro steps, named after the scientist who experimentally observed them for the first time [35]. For a specific n, the current-amplitude of the Shapiro step is given by

$$|\Delta I_{s,n}| = I_c\left|J_n\left(2\pi\frac{V_{ac}}{\omega_{ac}\,\Phi_0}\right)\right| \tag{1.19}$$

Eq. 1.18 represents the central relation of the so-called *inverse ac Josephson effect*, which shows the Josephson junctions property of converting a frequency excitation

f_{ac} (typically in the microwave range) into a voltage V_n. This relation has been shown to be independent of experimental variables such as type of superconductor, temperature, excitation frequency and power with very low uncertainty ($\sim 10^{-16}$) [36][37][38]. The conversion factor ${\Phi_0}^{-1}$ is known as Josephson constant and is indicated with K_J. According to the most recent CODATA adjustment [39], the value of the Josephson constant is

$$K_J = {\Phi_0}^{-1} = \frac{2e}{h} = 483\,597.8525(30)\,\mathrm{GHz/V} \tag{1.20}$$

where the number in parentheses is the one-standard-deviation uncertainty in the last two digits of the given value.

Thanks to inverse ac Josephson effect and to the extreme accuracy of frequency measurements via caesium atomic clocks (10^{-15}) [9], Josephson junctions represent the heart of highly accurate dc voltage standards, as Josephson himself already suggested in his pioneering manuscript [31].

1.3.5 Real Josephson junctions

The electrical behavior of real Josephson junctions can be described by the resistively-capacitively shunted junction (RCSJ) model, proposed by Stewart and McCumber [40, 41]. Here, only the main aspects of the RCSJ model needed for a sufficient understanding of the following sections are reported. A complete and rigorous description can be found in Ref. [25].

As depicted in Fig. 1.8, the RCSJ model treats a real Josephson junction as a current-biased parallel circuit between an ideal Josephson junction (×), the junction capacitance C and the normal-state resistance R. Therefore, the electric current I_b supplied by the source is split into three components: the supercurrent I_s through

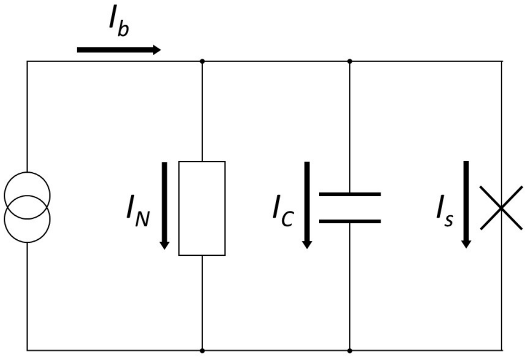

Figure 1.8: Current-biased real Josephson junction in RCSJ model.

the ideal Josephson junction, the displacement current I_C through the capacitance and the normal electron current I_N through the resistive branch. The dynamic of such system is governed by the equation:

$$I_b = I_c \sin(\varphi(t)) + \frac{V}{R} + C\,\frac{dV}{dt} \tag{1.21}$$

where V is the voltage drop across the parallel circuit. Combining Eqs. 1.21 and 1.14 one gets the following non-linear differential equation

$$I_b = I_c \sin(\varphi(t)) + \frac{h}{2e\,R}\frac{d\varphi}{dt} + C\,\frac{h}{2e}\frac{d^2\varphi}{dt^2} \tag{1.22}$$

Such non-linear system is prone to show chaotic behavior [42], which must be avoided by a thorough optimization of the junction parameters. From Eq. 1.22 it is useful to extract the dimensionless parameter

$$\beta_c = \frac{2e\,I_c\,R^2\,C}{\hbar} \tag{1.23}$$

that is known as Stewart-McCumber parameter and corresponds to the square of the quality factor of the parallel circuit in Fig. 1.8. Stewart-McCumber parameter is related to the damping of the Josephson oscillations caused by R and C and leads to distinguish between underdamped ($\beta_c > 1$) and overdamped ($\beta_c \leq 1$) Josephson junctions.

Practically speaking, underdamped Josephson junctions exhibit large resistance and/or capacitance. Current-voltage characteristic of underdamped junctions are hysteretic, as shown in Fig. 1.9. If a sole dc current is applied, the Cooper pairs current increases until I_c is reached for increasing currents. If bias current is further increased, the current-voltage characteristic approaches the normal state. By decreasing the bias current, an hysteretic behavior appears, more pronounced as β_c is

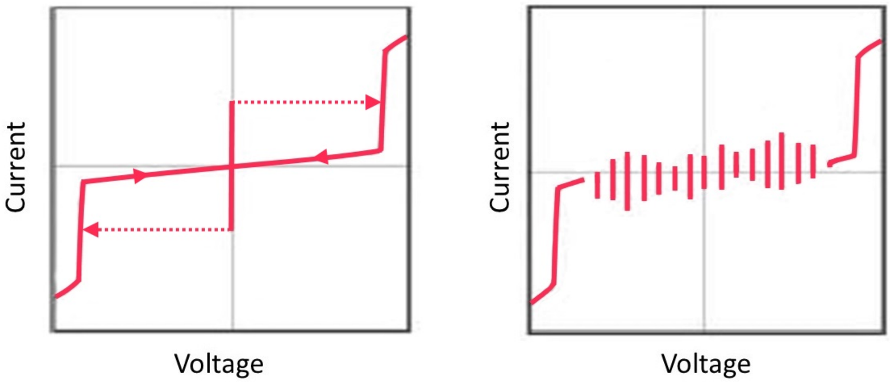

Figure 1.9: Current-voltage characteristics of an underdamped Josephson junction without (left) and with (right) ac excitation.

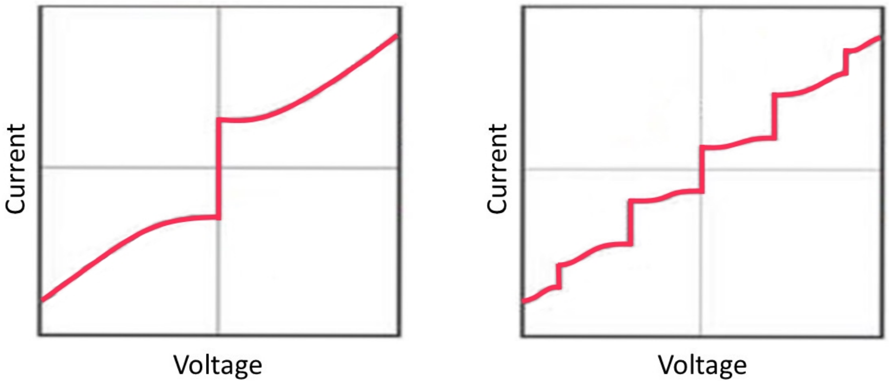

Figure 1.10: Current-voltage characteristics of an overdamped Josephson junction without (left) and with (right) rf radiation.

larger. If ac current excitation is added to the dc bias, several Shapiro steps overlapping around the zero-bias current axis are observed. This behavior is exploited in dc Josephson Voltage Standards, as will be explained in Sec. 1.3.6. Underdamped Josephson junctions are realized by using a thin layer of insulating material (I) as tunnel barrier, realizing the so-called superconductor/insulator/superconductor (SIS) Josephson junction.

Conversely, overdamped junctions exhibit a non-hysteretic current-voltage characteristic, where the same voltage value is measured for increasing and decreasing current. As can be seen in Fig. 1.10, different order Shapiro steps do not share the same current range, hence producing a single-valued curve: as it will be shown in the next chapter (Ch. 2), this is the most important feature for the realization of Josephson devices for time-dependent voltages. Overdamped junctions were first realized by externally shunting SIS junctions to lower their total resistance. However, intrinsically-shunted junctions using either a normal metal (N) or a combination between normal metal and insulating layers (I) as barrier are proven to be more compact and easier to fabricate and provide higher critical current values. Most common intrinsically-shunted Josephson junctions structures are SNS, SINIS and SNIS.

1.3.6 Arrays of Josephson junctions

In the early days, voltage standards consisted of single junctions which provided voltages of 5-10 mV [43]. Though much more stable than Weston cells, they were difficult to use because of the very low voltages [44]. Indeed, comparing the secondary Weston reference to the Josephson standard necessitated a precise voltage divider that was difficult to calibrate with the required accuracy [45]. Moreover, it is not possible to increase the voltage output by raising the microwave frequency, since it is not convenient to employ higher frequency generators because of their high cost and limited availability. Furthermore, it is not possible to increase the Shapiro step order n, due to the fact that step amplitude, i.e. quantum operating range, decreases for n increasing: as a consequence, many Josephson junctions have to be series-connected in order to attain practical voltage values. A first ambitious attempt was made by Endo in 1983 [46], where 20 junctions were connected in series and reached a relative accuracy of 10^{-9}. However, this solution was impractical for realizing larger arrays, because each junction was required to be individually biased on a quantum voltage step. Indeed, at that time, junctions fabrication was not sufficiently reliable to ensure a spread of the parameters that would have allowed to bias a large series array with a single current source. [25].

The solution to this limit was found by Levinsen in 1977 [47]: he suggested the use of highly-underdamped Josephson junctions ($\beta_c >> 1$) that, when microwave-radiated, develop overlapped quantized dc voltages crossing the zero-current axis. Therefore, using these zero-crossing steps, a larger spread in the junction parameters could be tolerated.

The possibility of obtaining quantized voltage steps at zero current over a wide range of junction and operating parameters paved the way to the realization of voltage standards using large arrays. The first Josephson array based on Levinsen's idea was developed in 1984 by NBS and by PTB and was made of 1474 underdamped junctions [48]. The first practical Josepshson arrays were realized in 1985 again by NBS [49] and PTB [50], using about 1500 junctions and rf fields from 70 GHz to 90 GHz. Improvements in the superconducting integrated-circuit technology allowed the fabrication of the first 10 V array in 1987 [51], which consisted of 14 484 junctions generating about 150 000 voltage steps in the range between −10 V and 10 V.

Josephson junctions technology

In order to realize Josephson arrays with thousands of series-connected junctions, integrated circuits are fabricated using thin-film technology, which includes sputter deposition of superconducting layers and dielectrics, patterning by photo or electron-beam lithography, and etching processes [28].

In the 80's, Josephson junction technology was based on lead (Pb) junctions, which have the drawback to be very sensitive to thermal cycling and humidity. For this reason, the research of a suitable material for realizing reliable and performing Josephson junctions addressed towards niobium (Nb), which still today is the most used element in conventional Josephson arrays. Niobium has a rather high critical temperature ($T_c \simeq 9.2\,\mathrm{K}$) that allows the operation in liquid helium at 4.2 K. In the fabrication of SIS, SINIS and SNIS junctions, niobium represents a good choice because it can be easily covered by aluminum (Al), which, in its oxide form, is used to realize the insulating layers. Moreover, for the fabrication of SNS junctions, it can be easily coupled to normal barriers made by gold-palladium (AuPd) and niobium-silicide (NbSi). Another possibility is the adoption of niobium-nitride (NbN) as superconducting material for raising the critical temperature to approximately 15 K and, hence, allowing operation at $\sim$ 10 K. Concerning Josephson arrays based on HTSs, a major breakthrough has not been achieved yet, since HTSs inhomogeneities prevent the realization of integrated circuits with a large number of uniform junctions [52].

The optimal frequency at which the array can be operated is called *characteristic frequency*, and is given by

$$f_c = K_J \, I_c \, R_N = K_J \, V_c \tag{1.24}$$

where I_c and R_N are critical current and normal resistance of the junction. Their product gives the *characteristic voltage* V_c, that is linked to the characteristic frequency f_c via the second Josephson equation (Eq. 1.18). Since both I_c and R_N are related to the size of the junctions, material parameters, dimensions and excitation frequency have to be attentively chosen to obtain the desired voltage output [53]. The value of the external rf frequency is set by a compromise between maximum voltage per junction and the cost of the high-frequency microwave source [54]. Moreover, to guarantee the junctions stable operation, i.e. optimal phase-locking between Josephson oscillation and external rf-field, a careful choice of the main parameters (junction size and critical current) has to be made, as rigorously descripted by Kautz [55, 42] and Nöldecke [56].

A Josephson array must be properly designed such that all junctions are excited by approximately the same rf power, which should be sufficiently high to generate wide zero-crossing steps. To that aim, junctions are embedded in high-frequency transmission lines, such as low-impedance microstriplines, coplanar waveguides (CPWs), or coplanar striplines (CPSs), depending on the frequency of the rf field employed. With microstriplines, the splitting of a single high-frequency line in two parallel ones is rather simple and can be performed several times [57].

Josephson chips are generally fabricated on silicon or glass substrates, with the integrated circuit consisting of [54]: (1) a $\sim$ 200 nm Nb film forming the base superconducting electrode of the junction, (2) a few nm of insulating/normal metal layer forming the tunneling barrier, (3) a $\sim$ 100 nm Nb junction top superconducting electrode, (4) a $\sim$ 300 nm SiO_2 film with windows for contacts to the top electrode, (5) a $\sim$ 400 nm Nb wiring film connecting the junction top electrodes, (6) a $\sim$ 2 µm layer of SiO_2 forming the dielectric of the microstripline, and (7) a $\sim$ 300 nm thick Nb ground plane. A schematic layout of such structure is shown in Fig. 1.11.

As anticipated, common Josephson arrays are operated at frequencies close to 70 GHz, for which a superconducting microstrip transmission line is required. The number of junctions in a single transmission line is limited by the attenuation of the rf power along the line. Therefore, in order to equally excite a large number of junctions, several branches are operated in parallel: the microwave is split and the resulting partial waves are fed into the different branches [28]. This is shown in

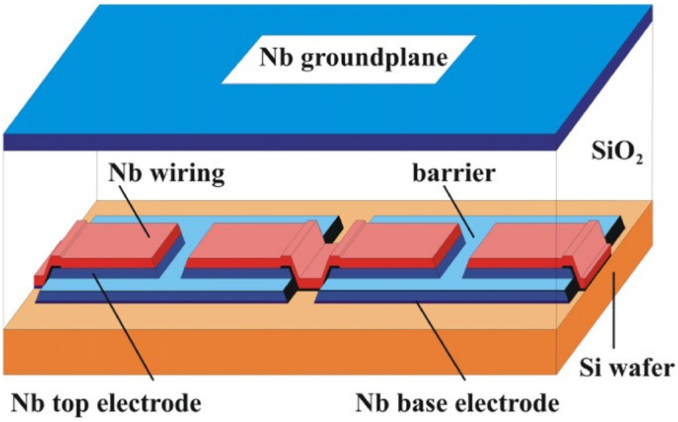

Figure 1.11: Schematic layout of a series of Josephson junctions arranged into a superconducting microstripline [58]. © 2012 IOP Publishing

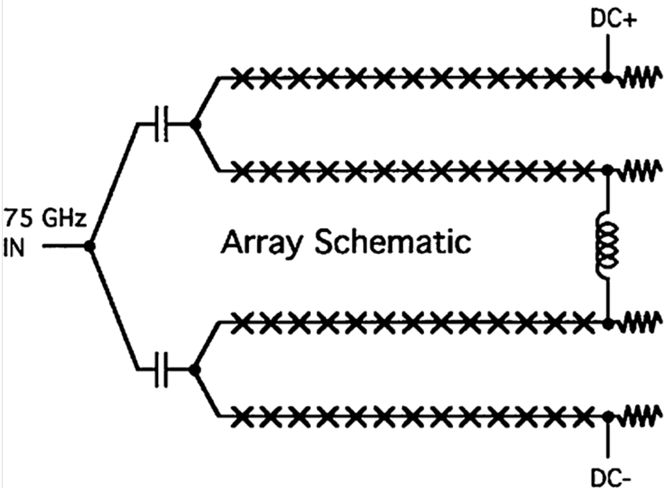

Figure 1.12: Circuit of a typical Josephson voltage standard integrated circuit chip [60]. © 2004 IEEE

Fig. 1.12, where a network of low and high-pass filters allows the microwave power to be split into four parallel paths, maintaining at the same time a dc path with all junctions connected in series [50]. The maximum attenuation of these branches ranges from 4 to 8 dB [59], which assures an adequately uniform distribution of the power to all junctions. Each microwave branch is terminated with a matched lossy loadline that suppresses microwave reflections, thus providing a uniform distribution of the microwave power by avoiding standing waves.

A typical integrated circuit layout for a Josephson array of 20 208 junctions is shown in Fig. 1.13 [54]: the microwave power is collected by a finline antenna and injected into sixteen microstriplines of 1263 junctions each. Microwave power is applied by inserting the finline into a slot parallel to the electric field in a WR-12

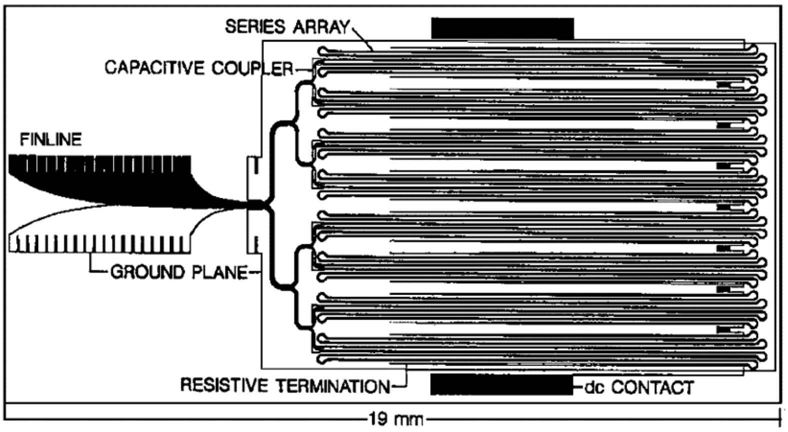

Figure 1.13: Layout of a 20 208 junction, 10 V Josephson voltage standard chip [60]. © 2004 IEEE

rectangular waveguide. The dc voltage output appears across the superconducting pads at the edge of the chip.

The dc Josephson voltage standard

Josephson voltage standards (JVSs) for the dissemination of dc voltages up to 10 V have been developed since the 1980s [54]. Presently, many JVSs systems are in use all over the world in national, industrial and military standard laboratories [43]. Currently, $Nb/Al_2O_3/Nb$ structure technology is employed for the fabrication of 10 V SIS Josephson arrays [28].

Thousands of underdamped Josephson junctions connected in series act as a quantum voltage standard that provides a voltage V_J given by

$$V_J = \frac{N\, n\, f_{rf}}{K_J} \tag{1.25}$$

where N is the number of junctions and n is the Shapiro step order, which typically ranges between 0 and 8 [9].

Owing to the high normal resistance of SIS junctions and the consequently large characteristic voltage, rf frequencies around 70 GHz can be applied to operate the arrays on higher order quantum steps: with $f_{rf} = 70\,\text{GHz}$ and $n = 5$, 14 000 junctions are sufficient to obtain a 10 V output [28]. Typical critical currents range from 80 to 200 µA, while, under microwave irradiation, overlapping voltage steps with a current width of 20-50 µA can be obtained [59].

In order to generate a well-defined quantum voltage with an underdamped Josephson array, a quite complicated procedure has to be followed [54]. The difficulty arises from the fact that all Shapiro steps are overlapping and, then, possible switching between them may occur. A digital-to-analog converter (DAC) with an

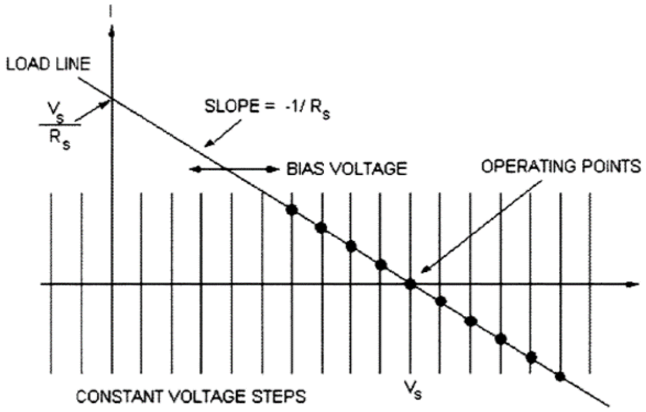

Figure 1.14: Graphical solution of the operating points for the dc Josephson voltage standard [60]. © 2004 IEEE

optically-modulated source resistance R_S is usually employed for applying a voltage V_S to the array: because of the source resistance R_S, the voltage V_S is split between the array and R_S following the loadline in Fig. 1.14. The intersections of this loadline with the current-voltage curve of the array are possible stable operating points. In order to select a particular quantum step, R_S is properly set such that the loadline becomes steep enough to intersect only the desired quantum step. After selecting a step, the source impedance is smoothly increased until the array current is zero. At this point, the array is disconnected from the bias source and the selected quantum steps are maintained for hours.

To calibrate a secondary voltage standard, i.e. a Zener reference, its output voltage is compared to that provided by a Josephson standard. To this aim, the difference of the two voltages is measured with a sensitive nanovoltmeter working as a null detector. The rf frequency is referenced to an atomic clock standard and can be adjusted in order to finely tune the Josephson voltage. Due to the temperature difference between the Josephson array and the room-temperature measurement equipment, thermal voltages appear, which can be compensated by reversing the polarity of both Josephson voltage and that of the secondary standard [28]. A further application of conventional JVSs is the calibration and linearity measurement of high-precision digital voltmeters [61].

Though the voltage across the Josephson array is, in principle, exact, the accuracy of the precision voltage measurement is limited by a wide number of uncertainty contributions, as frequency offset, leakage currents and EMI [54]. The accuracy of JVSs is then determined via international comparisons between the transportable JVS of the Bureau International des Poids et Mesures (BIPM) and those of the NMIs. Generally, the difference between two dc quantum voltage standards is better than 10^{-9} at 10 V [45, 62].

1.4 Other quantum electrical effects

For the sake of completeness, quantum standards for electrical resistance and current are shortly described below. Together with Josephson voltage standards, these can be combined in a single experiment to provide a self-consistent validation of the underlying physical theories.

1.4.1 Quantum Hall effect: the quantum resistance standard

Quantum Hall effect is a macroscopic quantum phenomenon discovered by Klaus Von Klitzing in 1980 [63]. It is the quantum-mechanical version of the classical Hall effect. Quantum Hall effect is generally observed as a stepwise variation of the electrical resistance of a sample as a function of the applied magnetic field at temperatures lower than few kelvins. For his findings, Von Klitzing was awarded with the Nobel Prize in 1985.

In the classical Hall effect [64], a current of particles with charge q and velocity $\vec{v}$ flows through a device placed in a perpendicular magnetic field $\vec{B}$. The particles are then deflected by the resulting Lorentz force qvB toward one side of the device. This leads to a charge redistribution that gives rise to an electric field $\vec{E}$ across the device. The equilibrium is reached when a Coulomb repulsive force $q\vec{E}$ opposing the Lorentz force appears, which generates a Hall voltage V_H proportional to B and perpendicular to both the magnetic field and the current flow.

Quantum Hall effect occurs in bidimensional electronic gas (2-DEG) systems subjected to low temperatures and strong magnetic fields. The 2-DEG can be realized in semiconductor devices by confinement with electrostatic fields: silicon metal-oxide field-effect transistors (Si-MOSFETs) require an appropriate gate voltage polarization, while in gallium arsenide (GaAs/AlGaAs) heterostructures the field is created at the interface of two epitaxial layers of different composition [65]. Again, when the Lorentz force resulting from the applied magnetic field is equal to the Coulomb force, a Hall voltage V_H perpendicular to the current direction is generated and a longitudinal voltage V_{xx} appears across the device. Nevertheless, differently from the classical case, V_H is no longer directly proportional to the magnetic field B: a series of voltage plateaus arise for some specific ranges of B for a heterostructure (or gate voltages for a Si-MOSFET) and, at this occurrence, the longitudinal voltage V_{xx} turns out to be zero [66]. Therefore, as shown in Fig. 1.15, the transverse resistance R_H, defined as the ratio between the Hall voltage V_H and the current flowing through the device, has a constant value along the plateaus that depends only on fundamental constants:

$$R_H = \frac{h}{i\,e^2} \tag{1.26}$$

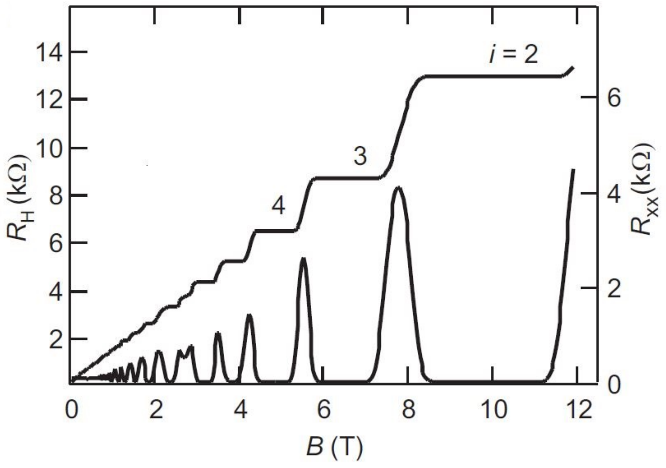

Figure 1.15: Hall resistance R_H and longitudinal resistance R_{xx} as a function of the magnetic field B in a GaAs/AlGaAs heterostructure and with constant current [67]. © 2001 IOP Publishing

where i is an integer number identifying the plateau. As with the Josephson constant K_J, a new constant arises from the combination of the Planck constant h and the elementary charge e: it is known as the Von Klitzing constant R_K and it is given by [39]

$$R_K = \frac{h}{e^2} = \frac{\mu_0\, c}{2\alpha} = 25\,812.807\,455\,5(59)\,\Omega \tag{1.27}$$

where μ_0 is the magnetic permeability of vacuum, c is the speed of light and α is the fine structure constant. Thus, R_K is linked to fundamental constants (α) which can be determined via atomic physics experiments [28].

Measurements of the quantum Hall resistance R_H are typically performed by NMIs and involve GaAs/AlGaAs heterostructures, which require cooling below 2 K and magnetic field $B > 10\,\mathrm{T}$ to reach the $i = 2$ plateau [68, 65]. Over thirty quantum Hall systems are in operation worldwide and comparisons have demonstrated that resistance artifacts can be calibrated with a reproducibility of about 10^{-9} [43][69].

1.4.2 Single-electron transport: a possible quantum standard for electrical current

In single-electron transport (SET) devices, n single charges are transferred at a clock frequency f, yielding a quantized current I given by [28]:

$$I = n\, e\, f \tag{1.28}$$

SET devices are based on two physical phenomena: 1) the tunneling of electrons through potential barriers and 2) the Coulomb blockade. Tunnel junctions consist of two metallic contacts separated by a sufficiently thin insulating layer. Coulomb blockade occurs in small devices with a large capacitive charging energy: electrons inside the device create a strong coulombian repulsion that prevents other electrons to flow [70].

The basic SET circuit is the single-electron transistor shown in Fig. 1.16: it consists of a conducting island connected to two electron reservoirs (source and drain) via two tunnel junctions with resistance R_T and capacitance C_T. The island is capacitively coupled to a gate electrode via the gate capacitance C_G [71]. Tunneling of single electrons can be observed as a macroscopically observable effect if Coulomb interaction dominates on the energy scale. In order to prevent random thermal transfer of electrons, the charging energy E_C required to transfer a single electron on the island must be considerably larger than the thermal energy, hence

$$E_C = \frac{e^2}{2C} \gg kT \tag{1.29}$$

where C is the total capacitance ($C = C_T + C_G$). Thus, this effect can only be observed at temperatures in the mK range and in structures with $C \sim 1\,\mathrm{fF}$, that means at the nm size [72]. When the gate potential V_G is zero, tunneling of an electron from the reservoir onto the island is suppressed for energetic reasons. At the same time, an electron cannot leave the island due to the potential barrier between the island and the reservoir. By means of the gate capacitance C_G, the electrostatic potential of the island can be continuously varied so that, for certain V_G values, an electron can be transferred to the island or leave the island. Such a SET

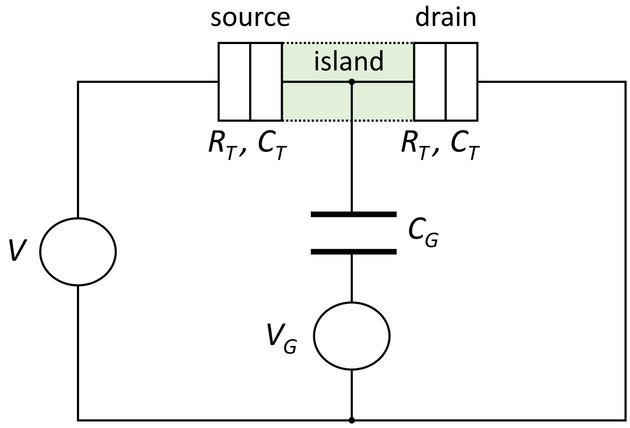

Figure 1.16: Single-electron transistor circuit.

transistor works similar to a field-effect transistor (FET), whereby the conductance is modulated by the gate charge.

In the scope of a possible realization of the ampere with SET devices, the most important parameters are the clock frequency f, related to the amount of the quantized current, and the accuracy of this generated current, determined by a transfer error describing the difference between the number of elementary charges actually transferred and the intended number.

The clock frequency f is limited by the time constant of the tunneling process ($f \ll (R_T\, C_T)^{-1}$). It is not easy to reduce this time constant, since the junction resistance R_T should be larger than R_K for preventing quantum fluctuations, whereas the reduction of C_T requires the fabrication of extremely fine nanostructures. For high-accuracy single-electron transfer, the clock frequency is limited to the 10 MHz range, corresponding to picoampere currents [28].

1.4.3 Quantum metrology triangle

In quantum metrology triangle (QMT) experiments, a consistency check of the three electrical quantum standards, i.e. Josephson voltage standard (Sec. 1.3.6), quantum Hall resistance standard (Sec. 1.4.1), and the single-electron tunneling current standard (Sec. 1.4.2) is investigated. Its graphical representation is depicted in Fig. 1.17.

The original version of the QMT aims to exploit Ohm's law ($V = R\, I$) to verify

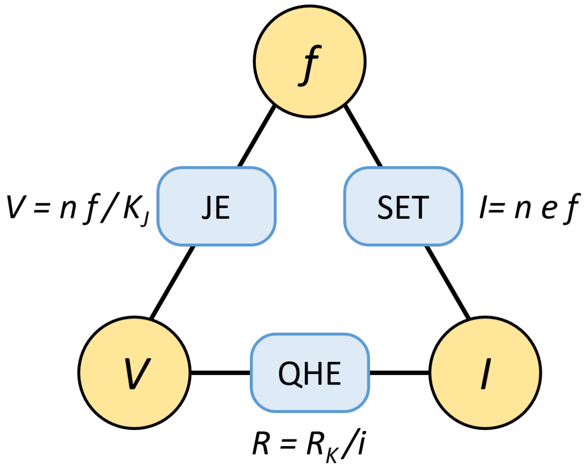

Figure 1.17: Quantum metrology triangle.

the mutual consistency of the three relations defining electrical quantum effects:

$$\begin{aligned} V_J &= \frac{n_J\, f_J}{K_J} \\ R_H &= \frac{R_K}{i} \\ I_S &= n_S\, e\, f_S \end{aligned} \tag{1.30}$$

Applying Ohm's law to Eqs. 1.30 and assuming that $K_J = 2e/h$ and $R_K = h/e^2$, one obtains

$$\frac{i\, n_J\, f_J}{n_S\, f_S} = K_J\, R_K\, e = 2 \tag{1.31}$$

It is commonly accepted that checking Eq. 1.31 with an uncertainty of 10^{-8} would be a relevant test of the validity of the three theories [73] and the triangle is said to be closed. Conversely, any deviation would lead to reconsider the validity of the equations for K_J and/or R_K.

The most straightforward way to test the closure of the QMT is to use a SET device for supplying a quantized current to a Hall resistance and, then, to measure its voltage drop against a Josephson voltage standard. Since the current involved in this experiment is very low ($\sim$ pA), it must be scaled up by means of a cryogenic current comparator [74]. Nevertheless, even with a current ratio of 10 000:1, the voltage across the Hall resistance would be too small to be measured with the required accuracy (10^{-7}) [2].

A more promising solution is represented by the so-called "charge version" of the QMT, where, Ohm's law is replaced by the natural definition of capacitance $C = Q/V$. A cryogenic capacitor C is charged by a SET device and, after a charging time T, the well-known charge $Q = n_S\, e\, f_S\, T$ is accumulated on the capacitor and its voltage drop is then measured by comparison with a Josephson standard. Finally, the capacitance $C = Q/V$ can be linked to the quantized Hall resistance via a quadrature bridge [65]. Up to now, the closure of the "charge version" QMT has been realized with uncertainties around 10^{-7} [75].

1.5 The conventional system of electrical units

As already mentioned, Josephson and quantum Hall effects are exploited to obtain highly reproducible voltage and resistance values which depend only on natural constants. To enable the use of Josephson and quantum Hall systems as realization of volt and ohm, the value of K_J and R_K have to be known in SI units. However, the best SI volt and ohm realizations are less accurate than the reproducibility of quantum standards by about two orders of magnitude [45].

It was then realized that defining conventional values for K_J and R_K would have benefited the world-wide uniformity of electrical measurements. Therefore, the Consultative Committee for Electricity (CCE) was asked to recommend such values based upon all relevant data that become available by June 1988 [76]. In 1988, the International Committee for Weights and Measures (CIPM) adopted two recommendations [77][78] that set *exact* values for K_J and R_K and called for all member states of the Metre Convention to base their standards on these values from 1 January 1990. All the values for K_J and R_K in SI units were analyzed and the following conventional values were proposed:

$$\begin{aligned} K_{J-90} &= 483\,597.9\,\mathrm{GHz/V} \\ R_{K-90} &= 25\,812.807\,\Omega \end{aligned} \tag{1.32}$$

Relative uncertainties of 4×10^{-7} and 2×10^{-7} were respectively assigned to K_{J-90} and R_{K-90} to guarantee the consistency with the SI values [76]. By convention, these are not included in the uncertainties of the representation of the volt and the ohm, since any offset from the SI volt and ohm will be consistent among different laboratories using the Josephson and quantum Hall standards. This led to the birth of non-SI units for electrical quantities, generally identified with the ‘90’ subscript (V_{90}, Ω_{90}, F_{90}, H_{90}, ...), derived from K_{J-90} and R_{K-90} and said to be representations of the corresponding SI unit.

Subsequent accurate measurements of K_J and R_K in SI units have shown that K_{J-90} and R_{K-90} differ by some small amount, which are not significant for practical electrical measurements.

1.6 The redefinition of the SI

In October 2011, the 24th General Conference on Weights and Measures (CGPM) has proposed to redefine four of the seven SI base units, i.e. the kilogram, the ampere, the kelvin and the mole, in terms of fundamental constants. The revised definitions have been approved in November 2018 by the 26th CGPM and have come into force on 20 May 2019 [79]. The new definitions for the kilogram, the ampere, the kelvin and the mole are based, respectively, on fixed numerical values of the Planck constant h, the elementary charge e, the Boltzmann constant k, and the Avogadro constant N_A, and joined the fixed numerical values of three constants already included in the definitions of the other three base units (the second, the meter and the candela) [80]. These modern units do not depend on any external parameters and can be simultaneously realized in laboratories all over the world, thus strongly simplifying and improving the traceability of any measurements to the primary standards [43].

As regards to electrical units, the main change that follows from the new SI is that K_J and R_K are also fixed and, consequently, there is no longer the distinction between the representations of the volt and the ohm maintained in the laboratory and the inaccessible *true* SI units. The impact of the new SI and the resulting step change in resistance and voltage measurements is very marginal beyond the primary intrinsic standards calibrations. The most significant impact has been observed in the area of voltage, with a discontinuity of about −0.1 µV/V [81].

Chapter 2

Ac Josephson voltage standards

Following the great success of Josephson standards for the dc volt, in the mid-nineties, research on quantum voltage metrology was mostly focused on the study and development of Josephson devices for the synthesis of ac and arbitrary voltages. This was possible mainly thanks to the pioneering work by National Institute of Standards and Technology (NIST), which proposed and first successfully tested two distinct techniques, nowadays still under investigation and refinement, that exploit the quantum-physical properties of Josephson junctions to provide time-dependent voltage signals. According to the second Josephson equation:

$$V_J = \frac{n\,N}{K_J}\,f = n\,N\,\Phi_0\,f_{rf} \tag{2.1}$$

it is evident that the temporal dependence of the voltage V_J can be related to the time dependence of one of the variables on the right side of Eq. 2.1, namely the Shapiro step order n, the number of junctions N, and the excitation frequency f_{rf}.

The first ac Josephson standard proposed aimed at independently changing the Shapiro step order n of series-connected array segments, each counting a different number of junctions: it is called the programmable Josephson voltage standard (PJVS) [82]. The required rapid and programmed selection of the quantum steps can be achieved only with overdamped junctions, owing to their single-valued current-voltage characteristic. Conventional hysteretic Josephson junctions prevent this possibility since all the Shapiro steps are overlapping and share the same current range around zero-current axis (zero-crossing steps). The application of SIS arrays is in fact limited to dc calibrations, since their quantum state cannot be precisely controlled for an indefinitely long period [45]. Fortunately, important improvements in both the choice of materials and fabrication techniques enabled the production of large and uniform arrays of overdamped junctions, which was the main limitation that led to the employment of underdamped SIS arrays.

The second type of ac Josephson voltage standard allows the synthesis of voltage signals by properly modulating the excitation frequency over time. Nevertheless, the necessary phase-lock between the Josephson oscillating current and the modulated sinusoidal microwave drive can be maintained over a limited range of frequencies close to the characteristic frequency f_c, thus making this technique impracticable. However, it has been demonstrated that using trains of short current pulses in place of the continuous sinusoidal excitation allows to extend the phase-lock over a significantly wider frequency range [83, 84, 85]. Following this assumption, pulse-driven JVSs have been developed and are still under investigation. Owing to their capability of synthesizing basically any arbitrary waveform, in the literature they are also known as Josephson arbitrary waveform synthesizers (JAWSs). Moreover, pulse-driven junctions are treated as devices that generate perfectly quantized voltage pulses rather than constant voltage steps, as in the case of sinusoidally-driven junctions. Digital synthesis techniques and precise control of the timing of each pulse allows the synthesis of voltage waveforms with ultimate accuracy and stability [86].

Besides their quantum-accuracy, both types of ac JVS have the potential to determine the complete waveform of ac voltages, which is not possible in conventional calibration techniques based on rms thermal measurements. In addition, thanks to their rapid programmability, they allow to considerably reduce the calibration time. Clearly, these systems are also capable of synthesizing accurate and stable dc voltages, therefore, due to the improved noise immunity and simplified operation, they are supposed to supplant the use of conventional SIS-based Josephson standards in the next future.

In the following sections, the operating principles and the main features of programmable and pulse-driven Josephson standards are presented. However, for the sake of completeness, a short description of the “non-quantum” techniques based on thermal power currently employed in ac voltage metrology is given first.

2.1 Non-quantum ac volt: thermal voltage converters

To date, the measurement of ac voltage and ac current requires the use of ac-dc transfer standards, where some feature of the ac quantity to be measured is related to a known dc quantity in a calculable manner [87, 88]. Usually, the exploited feature is the rms of the ac electrical quantity, which can be related to a known dc voltage level. Thermal voltage converters (TVCs) represent a natural mean to achieve this relationship, since they work in accordance with the equivalent heating power principle, i.e. the equivalence of the Joule heat of a dc and ac current in a resistive heater: the Joule heat rises the temperature at the hot junction of one or several thermocouples, which in turn generate a measurable emf due to the Seebeck effect [2]. The heat produced by an unknown ac voltage signal is compared to that produced under a dc excitation, accurately calibrated through a dc JVS. The dc voltage produced by the thermocouples can be measured with high precision to achieve resolution of few parts in 10^7 [89].

Nevertheless, the most relevant limitations of real TVCs are due to the occurrence of thermoelectric and frequency-dependent effects. The discrepancy between real and ideal TVCs is described by the ac-dc transfer difference δ_{ac-dc}, defined as

$$\delta_{ac-dc} = \frac{Q_{ac} - Q_{dc}}{Q_{dc}} \tag{2.2}$$

where Q_{ac} is the rms ac input quantity and Q_{dc} is the mean of the positive and negative polarity dc quantities required to produce the same response of the rms ac quantity. Both polarities of the dc excitation are needed to average out any possible asymmetric difference in output arising from polarity reversal. Typically, ac-dc differences occur at low frequencies ($< 40\,\mathrm{Hz}$) by failure of the device to fully integrate the ac waveform (high time constant), at midrange frequencies ($40\,\mathrm{Hz}$ to $10\,\mathrm{kHz}$) by the thermoelectric effects that are not present with ac applied, and at higher frequencies ($> 10\,\mathrm{kHz}$) by parasitic reactive effects and skin-effect in the heater, lead structure or input connectors. For frequencies above $\sim 10\,\mathrm{MHz}$, signal reflection becomes an issue, and careful consideration must be given to impedance matching [89].

To date, four types of ac-dc thermal converters have been developed: single-junction thermal converter (SJTC) [90], multi-junction thermal converter (MJTC) [91], thin-film MJTC [92] and solid-state thermal rms sensor [93]. The simplest form of TVC is the SJTC, depicted in Fig. 2.1: it consists of an evacuated glass bulb containing a thin resistive heater wire and a single thermocouple attached to its mid-point by means of a small insulating bead. Due to their limited dimensions, SJTCs exhibit good frequency characteristics up to 1 MHz [95].

Subsequently, in order to significantly reduce thermoelectric effects, multi-junction thermal converters (MJTCs) were developed by connecting in series about a hundred thermocouples and thus reducing both heater temperature and thermal gradients. Furthermore, due to the larger output voltage, the temperature difference

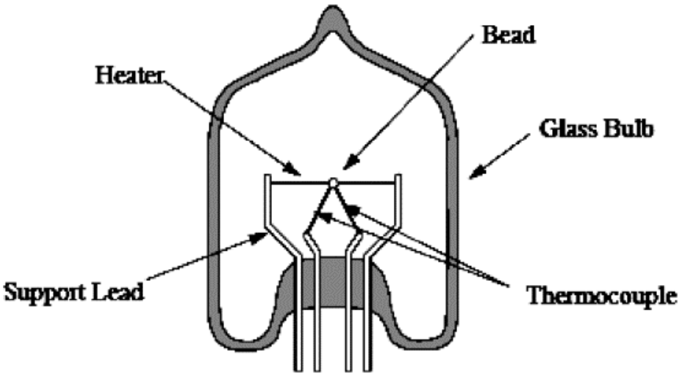

Figure 2.1: Schematic representation of a single-junction thermal converter (SJTC) [94]. © 2008 IEEE

between the hot and cold junctions can be kept small without loosing sensitivity. Ac-dc differences of MJTCs were calculated with an uncertainty of 3×10^{-7} in a frequency range from 10 Hz to 100 kHz [2].

The main drawback of MJTCs is related to their construction, which is difficult, costly and time-consuming. With the aim of overcoming these fabrication complexities, in the latter half of the 1980s, thin-film and micro-electro-mechanical system (MEMS) technologies, such as photolithography, thermal evaporation and sputtering techniques, replaced manual manufacture for the fabrication of planar MJTCs. As shown in Fig. 2.2, the basic elements of a planar MJTC are a thin-film heater on a thin dielectric membrane, a silicon substrate that surrounds and supports the structure, and thin-film thermocouples with hot junctions close to the heater and cold junctions over the silicon [66]. The silicon substrate thermally isolates the device from changes in ambient temperature, while the thin-film dielectric membrane isolates the heater and thermocouple hot junctions from the thermocouple cold junctions. This thermal isolation allows a temperature gradient to be developed across the thermocouple [89]. The voltage range for transfer measurements with planar MJTCs extends from 100 mV to 3 V, with uncertainties from 1 to 10 µV/V at 3 V in a frequency range from 10 Hz to 1 MHz. Ac–dc differences at voltages up to 1000 V and down to 2 mV are determined using range-to-range scaling techniques, with uncertainties rapidly escalating with the number of scaling steps [97].

Since planar MJTCs are very delicate and difficult to fabricate, they are mainly used by NMIs as primary standards. Among calibration laboratories, commercially-available solid-state thermal rms sensors [93], commonly called thermal transfer standards (TTSs), are the most widespread [95]. These work in a quite different

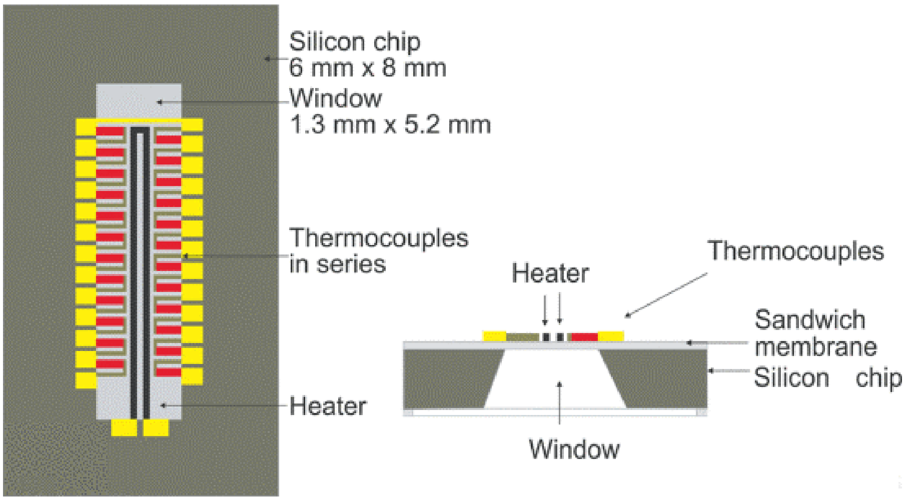

Figure 2.2: Top view (left) and cross section (right) of a thin-film planar multi-junction thermal converter (MJTC) developed at Physikalisch-Technische Bundesanstalt (PTB) [96]. © 2007 IEEE

way: instead of a thermocouple, they use the temperature dependence of the base-emitter junction voltage of a transistor to detect the temperature rise of the heater. The ac-dc difference of TTSs is a bit larger and less accurate than that of MJTCs. However, owing to an embedded protection circuit against overcurrents, they are hard to break up. In addition, the output voltage is higher than in TVCs, thus increasing the signal-to-noise ratio.

2.2 Programmable Josephson voltage standard

As anticipated, two main techniques exist to obtain quantum-based time dependent voltages across a Josephson junction array.

The programmable Josephson voltage standard (PJVS) is the first proposed and simplest quantum digital-to-analog converter (DAC) [82]. As shown in Fig. 2.3, a PJVS array is subdivided into M series-connected segments whose number of junctions follows a power-of-two sequence. As for dc JVSs, the entire array is radiated by the same microwave field, which allows each segment to produce useful Shapiro steps. Each segment (i) is individually current-biased on the center of the desired quantum step (usually $n = 0, \pm 1$) by a dedicated computer-controlled bias source ($I_{i,n}$), thus contributing to the overall output voltage in proportion to the number of junctions (2^i). For doing this, overdamped Josephson junctions are required, such that the current-voltage characteristics are single-valued and the steps are easily selected by setting the bias currents $I_{i,n}$. The PJVS operating principle is inherited from conventional DACs of semiconductor electronics, where the output voltage is

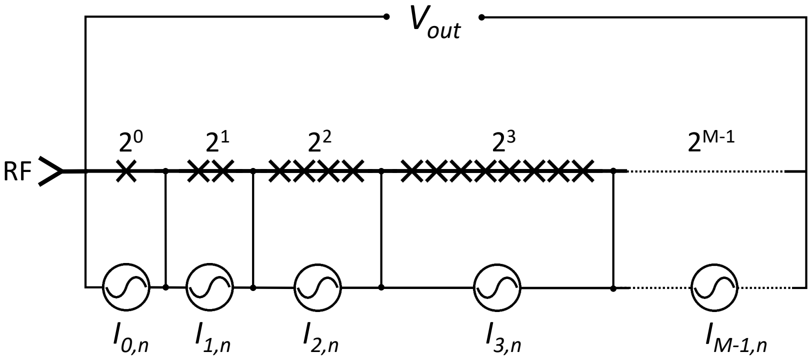

Figure 2.3: Schematic representation of the binary-divided programmable Josephson voltage standard (PJVS). Each segment is individually driven on its $n = 0$ or ± 1 Shapiro step by a current $I_{i,n}$ provided by a dedicated bias source.

digitized into M bits: if the bit is equal to 1 (or -1), the corresponding segment is current-biased on the $n = 1$ (or -1) quantum step, otherwise no current flows and the sub-array is biased on the zero quantum step. Finally, by properly driving and synchronizing each bias source, the PJVS output voltage can be modulated to synthesize quantum-based dc voltages as well as bipolar stepwise-approximated voltage waveforms, whose value at a given instant t is

$$V_J(t) = \sum_{i=0}^{M-1} 2^i \, n_i(t) \, K_J^{-1} \, f_{rf} \tag{2.3}$$

The resolution of this quantum DAC, i.e. the least-significant-bit (LSB), is given by the voltage across the smallest sub-array, which typically counts a single Josephson junction. On the other hand, the maximum voltage, i.e. the full-scale voltage V_{FS}, depends on the number of segments M and is obtained when the whole array is operated on the $n = 1$ step. Negative voltages up to $-V_{FS}$ are simply obtained by reversing the bit word, so that $n = 0$ and -1 steps are used. Ternary-divided PJVSs have been also developed by NIST to take advantage of the simultaneous availability of three quantum states and for reducing the number of bias lines without compromising the resolution [98].

Both V_{LSB} and V_{FS} are proportional to the microwave frequency f_{rf}: lower frequency means better resolution, but more junctions would be necessary to reach a given full-scale voltage. Typical rf frequencies of the different PJVS implementations around the NMIs are 15 GHz and 70 GHz. At 70 GHz, $V_{LSB} \simeq 145\,\mu\text{V}$ and nearly 70 000 junctions are required to reach the 10 V target level. On the other hand, working at 15 GHz is favorable in terms of resolution and cost of the microwave equipment, but the number of junctions per volt is about five times higher. PJVSs with up to hundreds of thousands junctions have been realized both for 15 GHz and 70 GHz, and are capable of providing voltages up to 20 V [99, 100]. Particular dual rf drive PJVS systems have been also investigated to further increase the resolution and produce quasi-continuous voltages [101, 102], with the aim of making them suitable for the calibration of nanovoltmeters at microvolt level.

PJVS circuits generate staircase-approximated voltage waveforms from dc to few kHz, whose frequency spectra exhibit many harmonics. Indeed, the original goal of programmable arrays was not the synthesis of highly pure sine waves, but rather to generate voltage waveforms whose rms is quantized and exactly calculable [82]. Unfortunately, this expectation has not been fulfilled by the experiments: the rms is not quantized at all and results to be largely affected by the finite rise time of the bias electronics ($\sim 1\,\mu\text{s}$), necessary to realize the transitions between the quantum voltage steps. During these transients, the voltage is not quantized, and special attention has been taken to reduce their duration. The rms error is then directly affected by the transients and, consequently, it was found to increase with the waveform frequency. Numerous investigations have also shown that the transition time and, hence, the rms voltage are affected by variations in the bias parameters, as microwave power and bias currents [103, 104, 105]. Modern electronics have proven successful to reduce the switching time and the duration of the transients to less than 100 ns [106], though the realization of an accurate rms waveform synthesizer was still precluded by transients-related systematic errors [107].

Synthesis with PJVSs is practical for rms measurements only for frequencies below 100 Hz, where a total uncertainty of few parts in 10^7 might be achievable [104]. This allowed the use of PJVS systems for ac electrical power metrology, where low frequencies waveforms around 50-60 Hz are of primary interest [108, 109]. To exploit the PJVS potentialities at frequencies up to the audio-range, a differential sampling technique has been developed, where the effect of the transients can be eliminated. A detailed description of this method is given in Sec. 2.2.1.

As anticipated, PJVSs enable easy and rapid selection of each accessible voltage level and, consequently, they are going to fully replace conventional dc JVS. Direct dc comparisons between PJVS and conventional JVS systems have demonstrated agreements of 10^{-10} and better at 10 V [110, 111, 112], and direct dc comparisons of two PJVS systems achieved agreements better than 10^{-11} [113, 114]. Therefore, the replacement of conventional JVSs with PJVSs has no impact on reported calibration accuracy. Indeed, PJVS standards are already exploited in several applications where the utmost accurate and stable dc voltages are required, as Zener standard calibrations [115], digital voltmeter (DVM) linearity measurements [116, 117], characterization of ADCs [118, 119], fast-reversed dc measurements of TVCs [120], impedance bridge implementations [121, 122], watt balance [123, 124] and QMT [125] experiments.

2.2.1 Differential sampling: the ac quantum voltmeter

The transients effect described in Sec. 2.2 can be eliminated using special sampling techniques, where the data points sampled when the PJVS is not settled on a quantum voltage level are simply discarded. In a first experiment, a sampling voltmeter was calibrated by directly sampling the PJVS quantum voltage levels [118]. Later, differential sampling has been proposed to calibrate ac voltage sources against the PJVS stepwise sine wave, thus improving the overall accuracy by using the sampler in a null-detection configuration [126, 102].

A schematic representation of such calibration system, commonly known as ac quantum voltmeter (QVM), is shown in Fig. 2.4. The ac signal from the source under calibration is subtracted by a stepwise PJVS sine wave of same frequency and amplitude: these two waveforms are synchronized and properly phased to minimize the voltage amplitude of the differential signal. To that aim, the sine wave has to cross the PJVS waveform at the center of the quantum steps, as illustrated in Fig. 2.5. This differential signal is then measured with a sampling voltmeter, acting as a null-detector and, thus, reducing errors due to gain, non-linearity and input impedance. Afterward, the original sine wave is reconstructed by properly summing

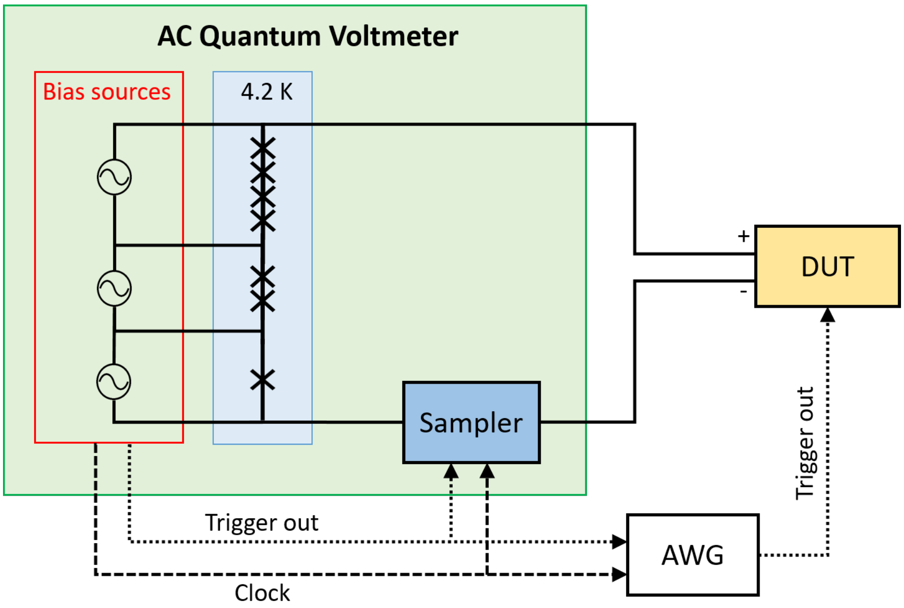

Figure 2.4: Schematic representation of the ac quantum voltmeter. The waveform generator (AWG) is required to adjust the phase between the two signals.

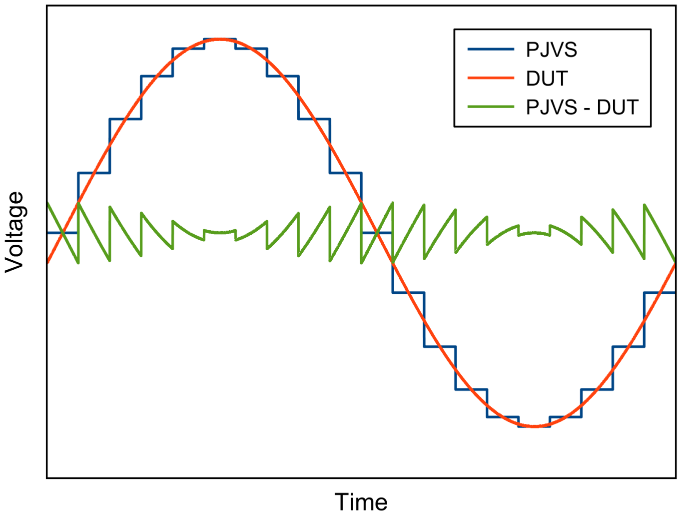

Figure 2.5: Differential signal (green) between the ac voltage provided by the source under calibration (red) and the stepwise sine wave provided by PJVS (blue). The red curve crosses the blue stepwise waveform in the center of each quantized step, so that the voltage amplitude of the difference signal is minimized.

the perfectly known values of the PJVS quantum steps to the measured differential signal. Furthermore, the data points sampled during the transients are canceled and, thus, do not affect the properties of the reconstructed sine wave. The output of the PJVS is then only used as reference if the array has settled on a quantized voltage step.

Thanks to the direct link to a quantum standard and to the low voltage measured by the sampler, a considerable improvement of the uncertainty is achieved. Excellent agreement between two PJVS systems of less than 10 nV/V was demonstrated using the differential sampling method with 60 Hz stepwise sine waves [102]. In addition, ac quantum voltmeters have proven to calibrate high-stability commercial voltage sources at better than 1 µV/V up to the kHz range [127, 128, 129], limited by the noise of the ac source. These are at least a factor of ten lower than those from the direct sampling method [126]. Furthermore, calibrations can be fully automated and take few minutes, whereas conventional ac-dc transfer measurements require about one hour to achieve uncertainties in the range of 0.1 µV/V [130]. Moreover, the capabilities of ac quantum voltmeters can be also extended to resistance ratios and dc currents measurements [131].

Owing to the transients issue, the maximum frequency of the ac quantum voltmeter is limited to few kHz: the number of voltage steps representing the reference sine wave cannot be neither excessively low, otherwise the differential signal would be too large to benefit from the null-detection configuration, nor too high, otherwise too many transients occur and an excessive number of data points should be discarded. Coherent subsampling methods are currently under investigation for extending the frequency of the ac source under calibration up to the MHz range, while keeping the reference PJVS waveform frequency below 1 kHz [132, 133].

Ac quantum voltmeters are commercially available both in liquid helium and in cryocooled versions [134, 135], allowing calibration laboratories to take advantage of quantum standards for improving their capabilities in ac electrical measurements. Furthermore, the use of cryocoolers allows the setup of fully automated turn-key systems [136].

2.2.2 PJVS technology

As already mentioned, single-valued current-voltage characteristics necessary for PJVS operation are obtained with overdamped Josephson junctions ($\beta_c < 1$, see Sec. 1.3.5). The most successful way to realize them is to replace the insulating layer (I) of SIS junctions with a low resistivity normal conducting barrier (N) or with a combination of I and N layers. Because of the low resistance of the N layer, SNS junctions generally exhibit lower characteristic voltages V_c with respect to hysteretic SIS junctions. Accordingly, the optimal microwave frequency f_{rf} is also reduced (typically $f_{rf} < 20\,\text{GHz}$), which is an advantage for the cost of the microwave electronics, though four-times as many junctions per volt are required

[45]. On the other hand, critical currents up to 10 mA and quantum steps few mA wide are achievable with SNS junctions, thus providing greater immunity to thermal and electrical noise.

The first practical 1 V PJVS array was realized by NIST [137]: it consisted of 32 768 Nb/PdAu/Nb junctions operated at 16 GHz and exhibited constant voltage steps 1 mA wide. Subsequently, the PdAu normal barrier has been replaced by amorphous niobium-silicide ($\mathrm{Nb_xSi_{1\text{-}x}}$), whose electrical properties are much easier to control. In fact, the stoichiometry and, thus, the resistivity of the barrier are determined by adjusting the relative sputtering rate, while the barrier thickness for a given stoichiometry determines the characteristic voltage V_c [138]. In addition, $\mathrm{Nb/Nb_xSi_{1\text{-}x}/Nb}$ junctions exhibit high fabrication yield, critical currents densities from 2 to $100\,\mathrm{kA\,cm^{-2}}$ and characteristic frequencies f_c up to hundreds of GHz, making them good candidates for the superconducting digital electronics [139]. Despite the wide range of characteristic frequencies attainable with NbSi barriers, NIST continued developing low f_c SNS junctions for frequencies from 15 to 20 GHz and voltages up to 10 V [140].

Prior to the success of NbSi barriers, the search of overdamped junctions suitable for operation at 70 GHz was mainly led by PTB, which developed and fabricated the so-called SINIS junctions, made by $\mathrm{Nb/AlO_x/Al/AlO_x/Nb}$, where two thin insulating layers ($\sim 1\,\mathrm{nm}$) are placed between the S/N interfaces of a SNS junction to increase V_c. One of the advantages of SINIS junctions was the adoption of the same reliable Nb-Al standard technology well established for conventional SIS junctions. Small series arrays and 1 V PJVSs with 8192 junctions were firstly fabricated [141]. Subsequently, 10 V PJVSs consisting of 69 120 junctions were also developed [142] and later significantly improved [143]. However, compared to other technologies, the fabrication of large SINIS arrays proved to exhibit low yield, due to their thin Al oxide insulating layers, and smaller current widths. PTB decided then to abandon SINIS technology and cooperated with NIST to the development of SNS junctions based on the more robust $\mathrm{Nb_xSi_{1\text{-}x}}$ technology, but tuning its stoichiometry ($\mathrm{x} \sim 10\,\%$) and barrier thickness ($\sim 10\,\mathrm{nm}$) to still get optimal characteristic voltages for the 70 GHz ac bias [144]. Using NbSi barriers, PTB fabricated for the first time 20 V PJVSs with roughly 140 000 junctions arranged in two stacks [99].

Researchers of Advanced Industrial Science and Technology (AIST) also fabricated 20 V PJVS arrays [100], but using a completely different technology: they employed $\mathrm{NbN/TiO_x/NbN}$ SNS junctions, exhibiting $f_c \simeq 15\,\mathrm{GHz}$ and a relatively high critical temperature that allows them to work at 10 K, particularly convenient for cryocooler operation [145]. On the other hand, the fabrication process of these arrays is complex and, owing to the low characteristic frequency, a considerably high number of junctions per volt is required.

Finally, it is worth to mention another kind of overdamped junction suitable for PJVS arrays that was proposed and widely investigated by researchers at INRiM: it features a SNIS structure, made by Nb/Al-AlO$_x$/Nb and derived from the well-known Nb/AlO$_x$/Nb technology of SIS arrays. The main differences reside in the increased thickness of the Al film, ranging from tens of nm up to about 100 nm, and in the augmented transparency of the AlO$_x$ insulating barrier [146, 147]. By properly tuning these two quantities, SNIS junctions can be fabricated over a wide range of electrical parameters, showing current densities from less than $1\,\mathrm{kA\,cm^{-2}}$ up to several tens of $\mathrm{kA\,cm^{-2}}$ and V_c from 100 µV to 700 µV at 4.2 K, thus enabling the operation at temperatures above the liquid helium boiling point [148]. In addition, because of the proximity effect induced in the thick Al layer, the temperature dependence of the critical current is reduced approaching the Nb critical temperature, with respect to other types of junctions [149, 150]. Following these findings, 1 V PJVS arrays with 8192 SNIS junctions have been fabricated in cooperation with PTB for rf bias around 70 GHz [148].

Concerning the transmission of the microwave signal, at frequencies around 70 GHz a microstripline is used, whereas PJVSs working at 15 GHz generally use a coplanar waveguide (CPW), where the junctions are embedded in the central line. Guidelines for the design of series arrays embedded in microstriplines were already established for conventional dc JVSs and, supplemented by some special design principles for overdamped junctions [151], are mostly valid for PJVSs radiated at 70 GHz [58]. Therefore, the structure of this kind of PJVS circuits (shown in Fig. 2.6) is very similar to that of SIS arrays for the dc JVS described in Sec. 1.3.6, though the microwave design becomes more complicated. PJVSs usually work on the first quantum step, whereas dc JVSs can be biased up to the fifth: a higher number of junctions is then needed to reach a given voltage and, consequently, a higher number of parallel microstriplines is required as well (from 16 to 128). In addition, it has been shown that the rf power attenuation in overdamped junctions

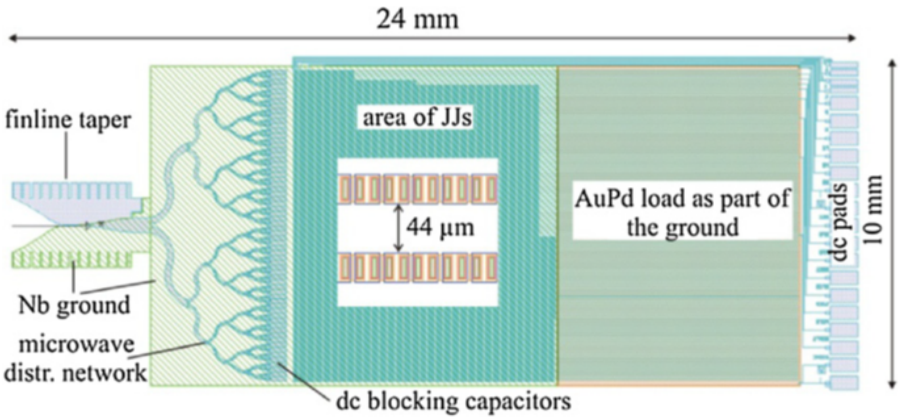

Figure 2.6: Layout of a 69 632 junction 10 V PJVS chip developed at PTB for operation at 70 GHz [58]. © 2012 IOP Publishing

is larger than in SIS arays, thus reducing the maximum number of junctions per microstripline. As with the dc JVS circuit in Fig. 1.12, the AuPd load of each microstripline serves as microwave termination, necessary to avoid an inhomogeneous rf power distribution by standing waves. Dc pads at the edge of the chip are connected to the PJVS sub-arrays via superconducting lines and allow low frequency bias currents and voltages to be applied and measured, respectively. The antipodal finline antenna connects the microstripline to the E-band rectangular waveguide while simultaneously matching the impedance of the waveguide ($\sim 500\,\Omega$) to that of the microstripline ($\sim 5\,\Omega$) [57].

2.3 Pulse-driven Josephson voltage standard

In principle, according to Eq. 2.1, quantum-accurate ac voltages from a single Josephson array can be attained by properly modulating the microwave frequency f_{rf}. Nevertheless, this is unfeasible for two main reasons: first, frequency-modulation with conventional rf synthesizers is difficult and not always possible; secondly, the Josephson current oscillation is phase-locked to the external microwave excitation only for a limited interval of frequencies around f_c. On the other side, simulations based on the RCSJ model demonstrated that rf-driving overdamped junctions with a stream of fast rectangular pulses in place of conventional sine waves allows to significantly extend the phase-lock frequency range [83, 84].

These observations led to the development of pulse-driven ac JVSs, whose output voltage is proportional to the repetition frequency of fast digital pulses. The pulse-driven JVS was first demonstrated by NIST with a 512 junctions array that generated constant voltage steps up to 265 µV, under operation by unipolar pulses at a repetition frequency up to 250 MHz [85]. The width of the quantum voltage steps was shown to be approximately identical for pulse repetition frequencies between zero and f_c, if rise and fall times of the pulses are short compared to $1/f_c$.

2.3.1 The Josephson arbitrary waveform synthesizer

The modulation of a generic voltage waveform in terms of pulses follows three main steps, schematically represented in Fig. 2.7. First, the desired waveform is encoded into a three-level digital sequence of ‘0’, ‘+1’ and ‘-1’, which mean respectively ‘no pulse’, ‘positive pulse’ and ‘negative pulse’. This is usually accomplished by means of second-order $\Sigma\Delta$ algorithms [152], that digitize one period of the waveform into M bits, indicatively with $M > 10^4$. Secondly, this digital pattern is stored into the memory of a semiconductor pulse pattern generator (PPG), which repeatedly provides the return-to-zero (RZ) fast current pulses to the Josephson array at a clock frequency $f_{clock} \sim 10\,\text{GHz}$. If the proper quantum conditions are met, each

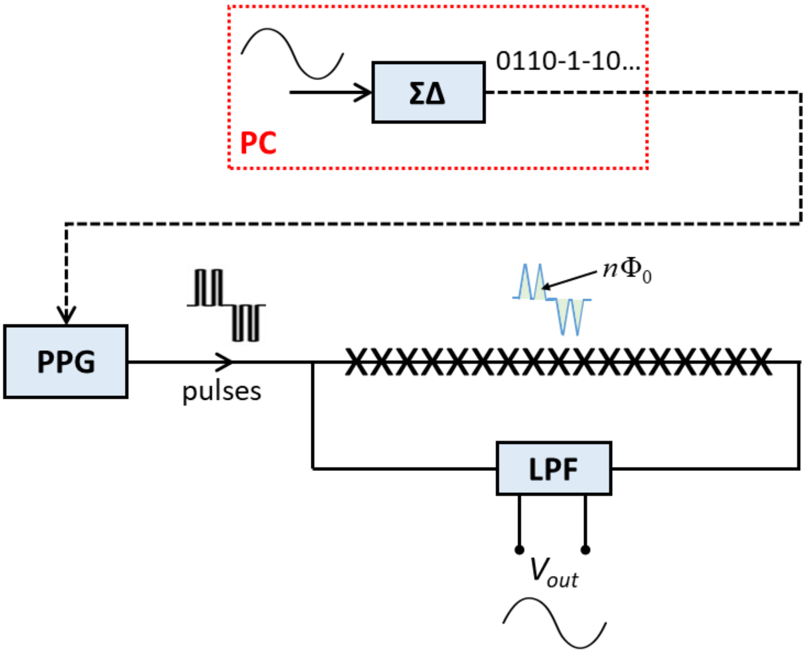

Figure 2.7: Operating principle of the pulse-driven JVS. A properly-designed low-pass filter (LPF) allows to obtain the low-frequency quantum waveform generated by the Josephson array.

junction converts each current pulse into a voltage pulse, whose time-integrated area is perfectly quantized and directly follows from the Josephson equation

$$\int V_J(t)\,dt = n\,\frac{h}{2e} = n\,\Phi_0 \tag{2.4}$$

where n is selected by adjusting the pulse amplitude. Finally, these quantized voltage pulses are low-pass filtered to obtain the quantum-accurate output voltage signal, whose peak amplitude V_p and frequency f_{out} are calculated as

$$V_p = n\,N\,\Phi_0\,f_{p,max} = n\,N\,\Phi_0\,A_{\Sigma\Delta}\,f_{clock} \tag{2.5}$$

$$f_{out} = \frac{f_{clock}}{M} \tag{2.6}$$

where N is the number of junctions and $f_{p,max} = A_{\Sigma\Delta}\,f_{clock}$ is the highest pulse repetition frequency. The $A_{\Sigma\Delta}$ parameter is the amplitude of the $\Sigma\Delta$ modulator and expresses $f_{p,max}$ in terms of the clock frequency. The $\Sigma\Delta$ modulation technique, in cooperation with the high oversampling ratio (OSR) ($f_{clock} \gg f_{out}$), enables to shift the quantization noise towards high frequencies (typically $> 10\,\text{MHz}$), so that it can be easily filtered out without affecting the quantized output waveform

[45]. $A_{\Sigma\Delta}$ generally takes values up to 95 %, i.e. $f_{p,max} \simeq 0.95\,f_{clock}$, since at higher percentages the stability of the $\Sigma\Delta$ algorithm is reduced, resulting in inband quantization noise [107].

From Eq. 2.6, it can be noted that the lowest frequency is limited by the memory size of the PPG, leading to frequency values around 500 Hz. Lowering the signal frequency by decreasing f_{clock} is not a viable solution because, from Eq. 2.5, the maximum output voltage V_p would be reduced as well. However, it has been demonstrated that the minimum frequency can be reduced up to few Hz by modifying the readout of the PPG memory, such that each bit is read repeatedly up to eight times in a row before reading the next [153].

The most remarkable outcome of the pulse-driven JVS is that, differently from PJVS, it enables the synthesis of sine waves with very high spectral purity and arbitrary waveforms with a programmable output spectrum for frequencies up to the MHz range [58, 154]. For this reason, it is commonly referred as Josephson arbitrary waveform synthesizer (JAWS). Indeed, notwithstanding that JAWS arrays neither improve time jitter nor quantize the pulse amplitudes, the fact that the time integral of the pulses is quantized (Eq. 2.4) is sufficient to produce nearly ideal spectra [155].

Initially, only two-level PPGs were available, so that either '0, 1' or '0, -1' digital codes could be delivered to the Josephson array and, hence, only unipolar ac voltages could be synthesized. To overcome this limitation, a special bias technique to obtain bipolar ac voltages was developed at NIST [156, 157]: the basic idea is to superimpose a two-level non-return-to-zero (NRZ) digital pattern provided by the PPG with a continuous sine wave using a directional coupler. By optimizing frequency, phase and amplitude of this sine wave, the unipolar digital code becomes bipolar and contains the three logic values '0', '1' and '-1'. Despite the complexity related to the need of a dual simultaneous rf bias, this technique succeeded in the synthesis of bipolar waveforms, but was abandoned as soon as three-level PPGs became available [158].

To date, JAWS systems capable of synthesizing bipolar and spectrally-pure sine waves with amplitudes up to 3 V have been successfully developed [159, 160, 161, 162]. Moreover, comparisons between two JAWS standards and between a JAWS and a PJVS have been performed, with the aim of verifying the accuracy of both systems. Sine waves generated with two JAWS arrays were found to agree with uncertainties better than 0.1 µV/V [163, 164]. The first direct JAWS-to-PJVS comparison, performed at 100 mV and 500 Hz with a sampling and multiplexing method, reported a relative agreement better than 1 µV/V [165]. A much lower relative uncertainty of few nV/V was achieved at 1 V and 250 Hz, by calibrating the JAWS sinusoidal waveform with an ac quantum voltmeter [166]. Furthermore, to highlight the JAWS capability of synthesizing arbitrary waveforms, PTB researchers employed a pulse-driven array to cancel the harmonic content from the stepwise waveform synthesized by a 1 V PJVS, with a relative accuracy of the sine wave amplitude around 0.1 µV/V [167].

JAWS standards are mainly used for audio-frequency applications, especially for the calibration of TVCs and TTSs [168, 169, 170]. In this frequency range, JAWS systems are indeed capable of reducing the ac voltage calibration uncertainty by an order of magnitude, compared to the traditional ac-dc transfer methods [171, 172, 173]. Instead, approaching the MHz range, frequency-dependent systematic errors arise, seriously limiting the accuracy (see Sec. 2.3.3 for more details). JAWS systems are also employed as dual voltage sources in automated impedance bridges [174, 175], which exhibit enhanced performances compared to PJVS-based bridges: in fact, the large harmonic content of PJVS stepwise waveforms makes the comparison of impedances of different kinds more challenging and limits the frequency range to few kHz [174]. Other applications include the calibration of null-detectors, such as nanovoltmeters and lock-in amplifier [176], and the testing of electronic components at high frequencies ($> 10\,\mathrm{kHz}$) [177].

Finally, not only electrical metrology has been taking advantage of pulse-driven standards outstanding capabilities: a low voltage version of the pulse-driven source is being used for Johnson noise thermometry and for an electronic measurement of Boltzmann constant. In such system, called the quantum voltage noise source (QVNS), the Josephson standard generates a calculable pseudo-random voltage noise, whose power is compared to the thermal noise power of a resistor [178]. The method can be implemented with voltage amplitudes below 1 µV [179], hence with few junctions.

2.3.2 Technology and techniques for the JAWS

Notwithstanding the demonstrated operation of JAWS arrays, the route to all these important outcomes required a lot of technological efforts. The most critical technological issue of pulse-driven arrays was related to the highest achievable output voltage. Since the maximum clock frequency of commercial PPGs is limited to about 15 GHz, tens of thousands junctions per volt are needed. The search for the optimal barrier material for overdamped junctions with $f_c \sim 15\,\mathrm{GHz}$ involved different technologies, as hafnium-titanium (HfTi) [180, 181], palladium-gold (PdAu) [85, 182] and amorphous niobium-silicide ($\mathrm{Nb_xSi_{1\text{-}x}}$) [138]. As with PJVS, the NbSi barrier resulted to be the most convenient and reliable solution. Compared to the ‘70 GHz recipe’ (Sec. 2.2.2), both Nb content and barrier thickness are slightly increased to about 20 % and 25 nm, respectively, allowing to reach the targeted characteristic voltage with suitably high critical current values and quantum operating margins [58, 183].

Concerning the rf pulse transmission, generally CPWs are employed, with the junctions embedded in the center line. Due to the harmonic richness of the pulsed ac bias, the splitting of the broadband microwave power into several branches is much more difficult than it is for conventional JVS and PJVS systems, where an almost monochromatic rf field is employed. Furthermore, arranging a such large number of junctions into a single line is also not feasible, since the rf power attenuation along the CPW would prevent the uniform radiation of all the junctions. The unique solution for achieving practical voltages was then to sum up the low voltages provided by several independently biased JAWS arrays.

However, before doing this, another issue was to be addressed. To avoid the reflection of the pulsed signal and the consequent formation of standing waves, detrimental for the uniformity of the rf power, a matching resistor is placed at the end of distributed Josephson arrays. The low frequency component of the rf pulsed signal generates an unwanted common-mode voltage across this termination resistor, which prevents to directly measure the JAWS output voltage with the electronic equipment, usually ground-referenced, and to connect in series two or more arrays. To avert this, the initially used arrays were then designed as lumped elements, with a consequent reduction of the maximum number of junctions, compared to distributed arrays [182]. Indeed, in order to be treated as lumped, the array size should be shorter than $\lambda/8$, where λ is the wavelength of the maximum repetition frequency ($\lambda/8 \sim 1.5\,\mathrm{mm}$ at $10\,\mathrm{GHz}$), thus setting strong requirements on junctions technology. All junctions are then all integrated near the maximum of the standing wave, and hence are uniformly operated. Lumped arrays can be directly grounded and a termination for the rf circuit can be inserted just before the array to reduce standing waves [184]. Moreover, arranging junctions in two or more stacks [185, 186] or in a meander line [187, 188] allowed to increase the total number of junctions within the limited length of a lumped array.

Yet, from the technological point of view, the use of larger distributed arrays was preferable and promising to increase the output voltage, though possible only if a microwave termination resistor was placed at the end of the array, with the consequent common-mode voltage noise problem. The solution to this was found by NIST researchers, who implemented the so-called ac-coupling method. A schematic representation of this technique is shown in Fig. 2.8: the rf pulsed signal delivered by the PPG is ac-coupled to the Josephson array by means of an inner/outer dc-blocking capacitor, i.e. a high-pass filter, which removes the low-frequency component of the pulsed signal so that no common-mode voltage appears across the termination resistor (R_{load}). However, this low-frequency component is necessary to current-drive the junctions on their quantum range. Since its shape is the same of the desired output waveform initially encoded into the pulse pattern, it can be directly reinjected across the Josephson array as a compensation current signal, via dedicated bias lines and by means of an additional arbitrary waveform generator (AWG), properly synchronized and phased with the PPG signal. Quantum operation is realized by adjusting pulse amplitudes, compensation signal amplitude and relative phase, and is identified by the complete suppression of the unwanted harmonics in the frequency spectrum [58]. As shown in Fig. 2.8, the output voltage leads are floating from ground, enabling the series-connection of several arrays to

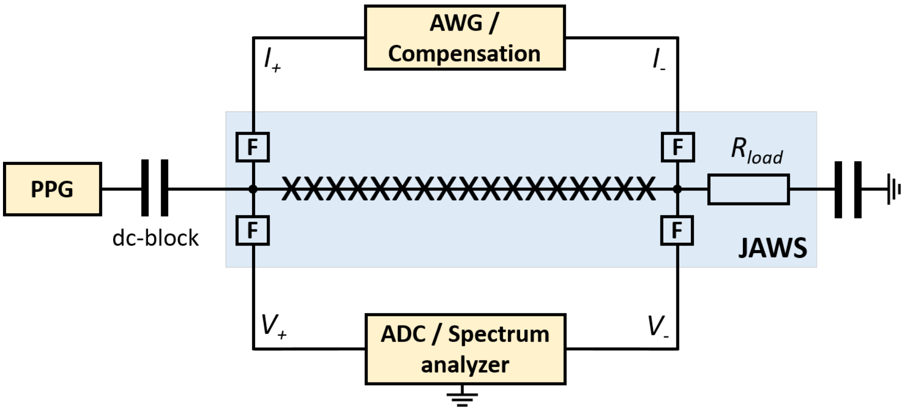

Figure 2.8: Schematic representation of the ac-coupling technique. The blue shaded area shows the actual on-chip elements. The two capacitors represent a single inner/outer dc block. The voltage output-leads and the compensation-current input-leads contain integrated on-chip low-pass filters (F) to avoid high-speed pulses to propagate on these lines.

increase the overall voltage. Yet, many parameters have to be adjusted, since each array requires its own dedicated PPG and AWG channels for the compensation, increasing both complexity and cost of JAWS systems for practical voltages.

For the sake of completeness, it is worth to mention an alternative, but less popular, solution for the common-mode noise issue in distributed arrays, for which no compensation current is required. For this reason, it is called the zero-compensation method [189, 190]. It makes use of PPGs capable of providing multiple levels to construct pulses with zero average current, if integrated over the entire pulse duration, but enough instantaneous peak power to transfer a flux quantum through the junction. This technique allows to considerably reduce errors generated by the pulse and compensation signals, although it limits the highest pulse repetition frequency and, as a consequence, the maximum output voltage.

A further, but completely different, way to avoid the ac-coupling technique consists of adopting particular opto-electronics schemes to transmit the pulses via optical fibers, as a way of splitting a single rf-pulse to many arrays and connecting these in series. More details on this method are given in Sec. 2.3.3.

PTB and NIST reached the important 1 V rms target level with Nb/$\mathrm{Nb_xSi_{1\text{-}x}}$/Nb junctions and adopting the ac-coupling method, hence by independently driving each array with dedicated pulsed and compensation lines [159, 160, 161]. PTB system consists of eight series-connected arrays operated on four separate chips, with a total of 63 000 junctions, and showed current margins of about 0.2 mA [159]. NIST first 1 V JAWS system consisted of 25 600 junctions, split in four arrays on a single chip, driven to the $n = 2$ quantum step and with operating margins around 0.4 mA [160]. Later, current margins larger than 2 mA have been obtained by doubling the number of junctions per array and driving them on the $n = 1$ step [161]. Recently, NIST researchers successfully realized on-chip Wilkinson dividers to equally split the broadband rf power from a single pulse bias line to two arrays. Consequently, summing up the voltages of two chips, each with 12 810 junctions distributed in eight arrays and two layers of Wilkinson dividers, they developed a 3 V rms JAWS system that requires only four PPG channels [162]. All these standards have proven to be capable of synthesizing spectrally-pure sine waves with highest harmonic suppression around -120 dBc at frequencies of few kHz.

2.3.3 Ongoing investigation

Mitigation of the voltage lead errors

As mentioned in Sec. 2.3.1, JAWS standards are nowadays capable of performing ac voltage calibrations up to 10 kHz with lower uncertainties than those obtained with ac-dc thermal techniques. A major challenge is the extension of this capability to faster signals, since frequency-dependent systematic errors arise and become the dominant contribution to the uncertainty budget [191]. Indeed, the voltage measured at the input of the ac voltmeter, i.e. the device under test (DUT), deviates from the calculable voltage provided by the JAWS array following approximately this relation:

$$\frac{V_{DUT}}{V_{JAWS}} \simeq 1 + 2\,\pi^2\, f_{out}^2\, L\, C \tag{2.7}$$

where f_{out} is the signal frequency and L and C are the equivalent inductance and capacitance of the system, thus including voltage line and DUT. This deviation is positive and has a squared dependence on both signal frequency and length of the voltage leads, being the latter correlated to the cable inductance and capacitance values [192].

The increase of the measured ac voltage can be explained in terms of a resonance in the system due to the combination of the DUT input impedance, on-chip inductance of the array and inductive filters, and the output voltage cable inductance and capacitance. This voltage lead error can be neglected below 10 kHz, but is relatively large and requires correction at higher frequencies [191]. It can be both estimated from the residual parameters of the cable [191] and experimentally determined [172, 192].

The most straightforward solution to reduce this error is however to use shorter cables: this would lower significantly the cable inductance and capacitance, causing the resonance to shift towards higher frequency. On the other hand, the use of long leads is unavoidable, since these have to connect the DUT at room temperature to the Josephson array operated in a 4 K cryostat. If the array is cooled in a LHe dewar, the output leads are typically about 1.5 m long, whereas leads can be shortened up to 0.5 m with cryocoolers. Deviations of almost 10 000 µV/V (1 %) at

1 MHz have been reported with voltage leads about 1.5 m long [192]. Halving the cable length with the use of a small cryostat reduces the deviation at 1 MHz by an order of magnitude [193]. The correction to be made for the voltage leads is then an order of magnitude smaller and, hence, more reliable.

This voltage deviation can also be explained in terms of electromagnetic waves reflection between the DUT and the JAWS array, caused by impedance mismatch, even if the signal wavelength is much longer than the typical cable length [194]. Therefore, another approach to avoid this systematic error is to use impedance matching, such that reflections do not take place. Matching the impedance at the load side of the system is an hard task, since a frequency independent resistance that is equal to the characteristic impedance of the cable (typically 50 Ω) should be used. In addition, this low resistance would cause the Josephson array to source a significant amount of current. Impedance matching at the source side of the system is then under investigation to flatten the frequency response of the voltage leads [195].

Opto-electronic pulse-driven Josephson standard

An opto-electronic version of the JAWS was proposed [196] and is nowadays under development [197]. In such system, the electrical pulse stream from the PPG is converted into optical pulses, usually by modulating a laser source, and then transmitted through an optical fiber to the cryogenic environment. Here, a reversed-bias photodiode is used to reconvert the optical pulses into electrical, which are then used to ac bias the Josephson array, as customary. Since photodiodes generate unipolar electical pulses, two of these are series-connected and biased with opposite polarities to produce three-level electrical pulses, necessary to synthesize bipolar ac voltages.

The main advantage of this intermediate optical stage is that the optical stream can be sent to many parallel arrays by means of conventional optical beam splitters, thus enabling easy scalability to larger voltages by using several arrays in series [198]. The Josephson array is in fact electrically isolated from the PPG, preventing the common-mode noise issue and avoiding the complexities related to the ac-coupling technique. Furthermore, an optical fiber allows operation at frequencies up to 40 GHz [199] and reduces the heat load to the cryogenic stage with respect to coaxial cables for the current pulses transmission.

On the other hand, several challenges related to the packaging of such a system need to be addressed. These include the accurate bonding and contacting of the photodiode to the carrier, the precise alignment of the optical fibers to the photodiodes, and the significant thermal stresses induced at cryogenic temperature, typically at interfaces between dissimilar materials [200].

Chapter 3

Cooling quantum voltage standards

This chapter provides an overview of the common techniques and equipment employed for achieving cryogenic temperatures suitable for the application of JVSs. As mentioned in the previous chapters, most of these use niobium as superconducting elements, whose critical temperature is around 9 K. Cooling such standards well below this point, hence in a range around 4 K, is generally required. Techniques to obtain such temperatures include both passive systems, involving the use of a liquid helium in a bath cryostat, and active cryo-refrigeration systems, commonly known as cryocoolers. Both cooling methods are described in this chapter, with more insights on the latter, in that they represent an ongoing intense field of research, as demonstrated by literature.

3.1 Passive cooling: bath cryostats

For many years, the use of stored liquid cryogen systems has provided a reliable and relatively simple method of cooling over a wide range of temperatures, from below 4 K for liquid helium (^{4}He) to 77 K for liquid nitrogen (N_2). These systems rely on the boiling of the low-temperature fluid to provide cooling of the desired load, thus making use of their latent heat of vaporization.

Stored cryoliquids can be used for cooling in a number of different states, including normal two-phase liquid-vapor (subcritical), low-pressure liquid-vapor (densified) and high-pressure, low-temperature single-phase (supercritical) states. Subcritical fluids, such as low-pressure helium, have long been the cooling means for very-low-temperature (1.8 K) sensors for space astronomy missions [201].

The advantages of these systems are temperature stability, high thermal conductivity, freedom from vibration and electromagnetic interference (EMI), and negligible power requirements. The disadvantages are their limited life or requirement for constant replenishment, the inability to smoothly control the cryogenic load over a broad range of temperatures and the high weight and volume.

3.1.1 Liquid helium cryostat

Liquid helium (LHe) cryostats are commonly based on "dewars", which are special containers consisting of one or more reservoirs surrounded by a vacuum jacket that isolates these from the room temperature environment. Dewars inner tank holds the LHe at 4.2 K and is suspended inside an outer vacuum shell with low-conductivity structural supports [201]. The gap between the two tanks is evacuated and filled either with multilayer superinsulation, consisting in several thin layers of low emissivity material, or with liquid nitrogen at 77 K, allowing to further reduce the radiation heat load into the inner LHe reservoir.

Most simple and reliable dewars are made of stainless-steel, because of its low thermal conductivity and of the facility of welding it to similar or dissimilar metals [202]. Welded joints can withstand several cycles between room temperature and 4.2 K and still remain leak-tight after years of use. Welded dewars are used for storage or for directly immersing the sample, generally installed at one end of a special low-thermal conductivity stick probe, into the LHe vessel through an open neck on the top of the dewar. Temperatures up to 1.3 K can be achieved by reducing the pressure on the top of LHe bath through an appropriate pumping port. Temperatures higher than 4.2 K can instead be attained either by means of an external heater, properly placed in contact with the sample holder, or by raising up the stick probe, such that the device is cooled by evaporating He gas. All dewars for cryogenic liquids are equipped with safety valves, which prevent the internal pressure to raise to dangerous values in case of accident [203].

The latent heat of evaporation of ^{4}He is about 2.6 kJ/dm^3 at its normal boiling temperature. The enthalpy of He gas between 4.2 K and 77 K (300 K) is 64 kJ/dm^3 (200 kJ/dm^3). Therefore, it is important to cool the cryostat by exploiting the full enthalpy, accomplished when the He gas leaves the cryostat at a temperature close to room temperature. Furthermore, pre-cooling the dewar with liquid nitrogen from 300 K to 77 K before the LHe transfer is convenient in terms of LHe consumption, since liquid N_2 has a vaporization heat about 60 times that of LHe and is much cheaper [203].

3.2 Active cooling: cryocoolers

For cryogenic applications where stored liquid cryogens are inconvenient, mechanical refrigerators (cryocoolers) are often the preferred solution [201]. Cryocoolers are closed-cycle engines that use gas compression-expansion cycles to produce refrigeration: the work done on the gas by compression is rejected to the surrounding, then the expansion of fluid to a lower pressure in a separate chamber achieves cooling [203].

Recently, the development of small and reliable cryocoolers has been strongly stimulated by the emergence of specific applications that require modest refrigerating powers, among which

- cryogenic pumps for high vacuum in semiconductor processing facilities;
- cooling infrared detectors for military, space and laboratory instruments;
- cooling superconducting devices;
- sample and test cooling for scientific and medical research;
- cooling of heat shields and recondensation of cryogenic liquid in machines for magnetic resonance.

A wide range of cryocoolers has been developed to meet different temperature and cooling power needs. Several thermodynamic cycles are exploited, among which Stirling, Ericsson, Joule-Thomson and reverse-Brayton cycles are the most common [201]. In addition, other cycles, such as adiabatic demagnetization and the dilution cycle, are primarily used for achieving ultra-low temperatures below 1 K [204].

Cryocoolers can be classified into two types according to the employed heat exchangers, which can be divided in recuperators and regenerators [205]. A recuperative heat exchanger is a device in which two separate conduits are provided, respectively for the hot and cold fluid. The flows are separated by a solid wall, through which the heat is transferred by conduction. On the other hand, a regenerative heat exchanger is provided with a single conduit through which the hot and cold fluids alternate. It generally consists of a porous matrix of finely divided material in the form of wire mesh, plates or small balls [203]. Regenerators material exhibit poor thermal conductivity, high specific heat and large surface area, to absorb the heat from the incoming warm gas and return it to the colder exiting gas [202]. Another key feature for the classification of cryocoolers is the way the refrigerant fluid flow is regulated, which can be made by volume changes or by valves [205]. All the recuperative machines use valves, so the classification based on the flow regulation mode refers only to the regenerative cryocoolers.

The main advantages of a cryogen-free system compared to bath cryostats are [206]:

- the need of periodic supplies of cryogenic liquids is avoided, resulting in lower operating costs;
- no special knowledge or precaution is required, since cryocoolers are basically “push-button” machines;

- the dimensions of a cryogen-free system are generally smaller than those of a bath cryostat, as there is no accumulation tank for the cryogenic fluid;
- a cryogen-free system can operate anywhere there is a power outlet;
- cryocooler provide cooling over a broad range of temperatures.

However, because of the inefficiencies and parasitic losses, the actual operation of cryocoolers is quite different from the ideal behavior: the main causes are pressure drops, the non-isothermal compression and expansion transformations of the thermodynamic cycle and the inefficiency of heat exchangers. Compared to bath cryostats, power dissipation becomes more demanding, as described in detail in Sec. 3.5.1. Additionally, mechanical and temperature fluctuations of hundreds of millikelvin occur, as a result of the intrinsic cyclic nature of cryocoolers. Furthermore, an electrically driven compressor is required, leading to measurable levels of equipment vibration, EMI and audible noise that may negatively interact with the intended cryogenic application [201].

3.3 Cryocoolers for Josephson voltage standards

Gifford-McMahon (GM) and pulse-tube (PT) cryocoolers are commonly employed for the dry-cooling of quantum voltage standards. Both are regenerative coolers and use He gas as working fluid, whose flow is regulated by valves. The primary distinction between GM and PT cryocoolers resides on the method employed to obtain the necessary phase shift between the gas flow and pressure oscillations. In GM coolers, the fluid is moved through the regenerator by controlling the motion of a displacer, which is generally combined with the regenerator in a single body. The phase shift is determined by the timing of the displacer motion with respect to the production of low and high pressures. Differently, no moving parts are required to achieve the phase shift in PT coolers. This feature and the associated long-term reliability explain the attractiveness of PT refrigerators [207].

To achieve temperatures below 4 K, GM and PT cryocoolers employ two linked stage. A two-stage GM cooler can be indeed viewed as two cryocoolers in series, where the second stage, also known as cold finger, uses as hot source the cold heat-exchanger of the first stage. Regenerators used in the first stage are made of stainless steel, phosphor bronze or nickel, while, for cooling stages down to 4 K, a combination of lead balls and rare earths is used [203]. A radiation shield surrounding the second stage is typically attached to the first stage in order to minimize radiation heat load [201].

Nowadays, commercially-available GM and PT cryocoolers provide cooling powers up to 1.5 W at 4.2 K (second stage) and 40 W at 45 K (first stage).

3.3.1 Gifford-McMahon cryocooler

The GM cryocooler is based on an alternate oscillating flow of He gas in the $1 \div 3$ MPa range with a working frequency around 1-2.4 Hz. This low frequency is particularly useful for obtaining improved efficiency at very low operating temperatures, where the reduced specific heat of regenerator materials limits heat storage between the cycle phases [201].

GM cryocoolers are designed to work according to Ericsson cycle, which consists of two isothermal and two isobaric transformations. Its working principle is outlined in Fig. 3.1: the gas compression is obtained by an external compressor, supplied by electric power of typically 6 kW; the expansion-compression cycles are obtained by a rotary valve mounted on the GM cooler's cold head assembly that alternately connects the cold gas volume to the input or the output of the compressor. As anticipated, the required phase shift between gas pressure and mass flow is achieved by synchronizing the rotary valve with the motion of the “regenerator-displacer”.

The operation process of the GM cryocooler can be divided into four steps, illustrated in the right side of Fig. 3.1:

Step 1. The displacer is at the cold end, the low-pressure valve is closed, the high-pressure valve is open. The high-pressure He gas enters the upper chamber at room temperature.

Step 2. The high-pressure valve remains open while the displacer moves upwards. The high pressure gas flows through the regenerator, undergoes an isobaric cooling transformation and fills the lower chamber at low temperature.

Step 3. The displacer is at the top dead center, the high-pressure valve is closed, the low-pressure valve is open, placing the cryocooler in communication with the low-pressure tube of the compressor. The gas in the lower chamber undergoes an expansion; the obtained cooling effect can be used for cooling the low-temperature environment, so that the expansion can be assumed to occur at a constant temperature.

Step 4. The low-pressure valve remains open, while the displacer moves downwards. The low-pressure gas flows through the regenerator, is heated at constant pressure and refills the upper chamber at ambient temperature. The low-pressure valve is then shut and the cycle is repeated.

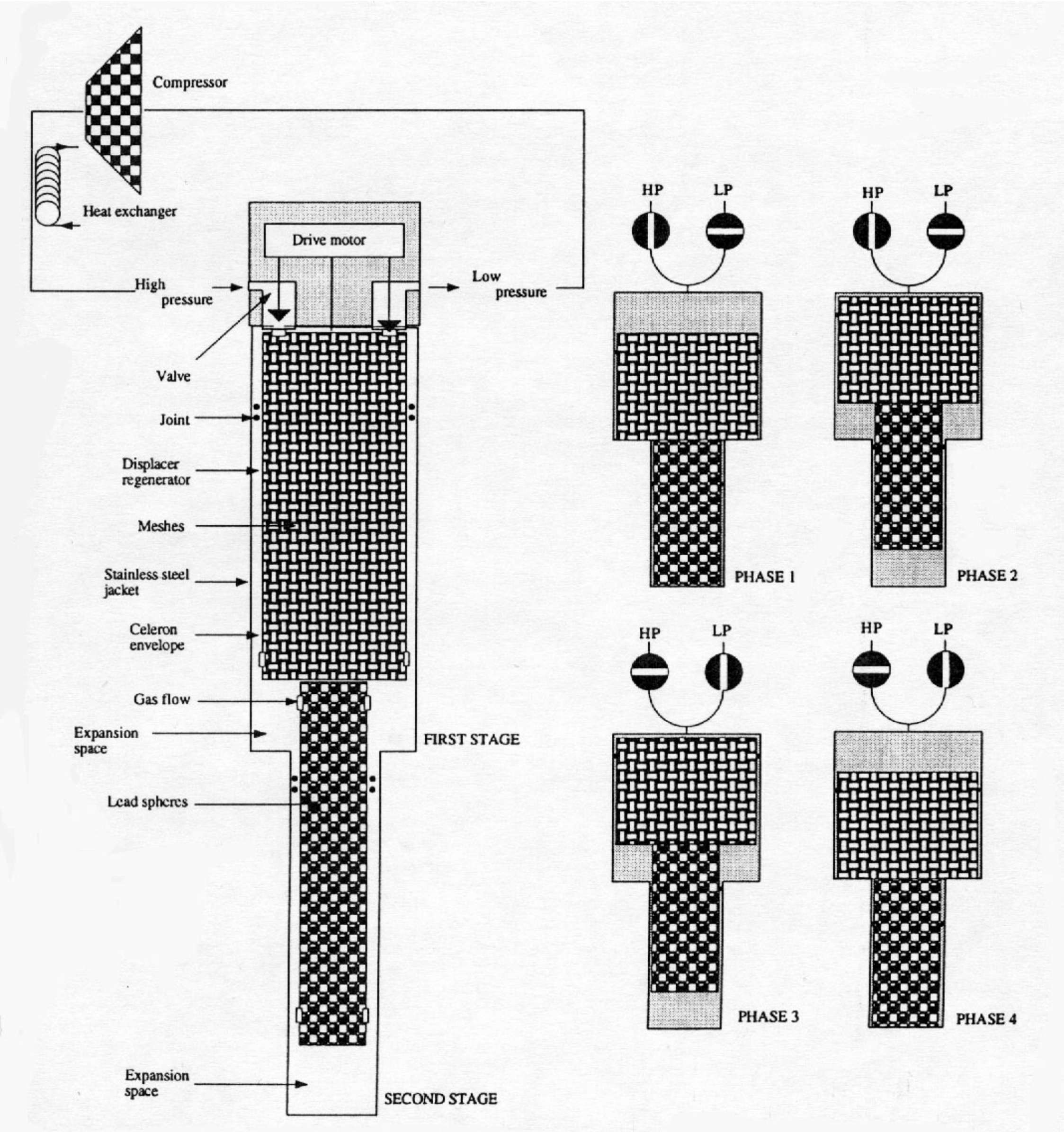

Figure 3.1: Scheme of a two-stage Gifford-McMahon (GM) cryocooler [208]. On the right side, its working principle: phase 1) high-pressure gas supply; phase 2) isobaric pre-cooling; phase 3) isothermal expansion; phase 4) isobaric heating and expulsion. © 1998 Taylor & Francis

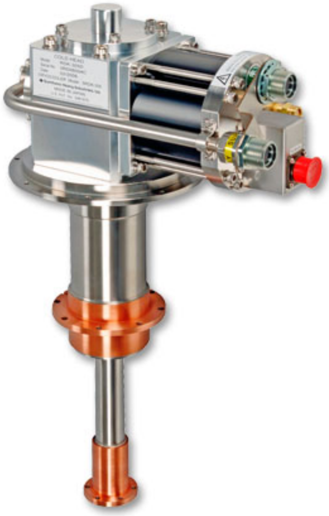

Figure 3.2: Commercial two-stage GM cryocooler with 1 W cooling power at 4 K. The He gas compressor is not shown. Courtesy of Sumitomo Heavy Industries [209].

A commercial two-stage GM cryocooler is shown in Fig. 3.2. Thanks to the high reliability and constructive simplicity, GM cryocoolers are widely used today and produced in a wide range of cooling powers.

3.3.2 Pulse-tube cryocooler

The best approach to increase the reliability of a cryocooler is to limit the number of moving parts at low temperature. With pulse-tube (PT) refrigerators, a cooling effect using an expansion device without a moving displacer is obtained, leading to a considerable gain in terms of oscillations, mechanical wear and maintenance issues.

PT coolers come into a wide variety of configurations [210]: here, only the orifice PT cryocooler is presented, in that it is the version generally employed in quantum voltage metrology applications. For simplicity, its schematic representation is shown in Fig. 3.3 for a single-stage configuration. As with conventional GM refrigerators, PT coolers contain a regenerator through which the cold and hot fluid is periodically cycled. The movement of the displacer is replaced by the alternate movement of a gas column induced by the same pressure oscillation [212]. The phase shift between the flow of the pressure fluctuation and the motion of the gas column is obtained by means of throttling valves, a flow-resistance (the orifice) and a buffer volume [203]. The so-called “pulse-tube” is a simple hollow tube with heat exchangers at either ends that puts in communication the orifice and the regenerator. Its purpose is to isolate the cold end of the regenerator from the hot gases returning from the orifice. It does this by achieving a temperature stratification along its length and

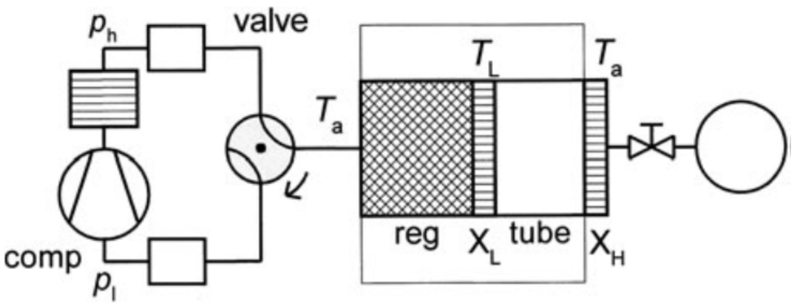

Figure 3.3: Schematics of a single-stage orifice pulse-tube (PT) cryocooler [211]. From left to right, it consists of a compressor, a rotary valve, a regenerator, a cold heat exchanger (X_L), a hollow tube, a hot heat exchanger (X_H), an orifice, and a buffer volume. © A.T.A.M. De Waele

having sufficient volume such that the gas at the hot end of the pulse-tube never reaches the cold end during the cycle. In order to maintain this strict temperature stratification, the pulse-tube design must carefully prevent any kind of gas mixing due to turbulent flow or gravity caused convection [201]. Therefore, PT coolers exhibit best performances when operated in vertical position and with the second stage heat exchanger pointing down [213].

Referring to Fig. 3.3, the operating principle of a single-stage orifice PT cooler can be simplified by considering a small gas parcel travelling from the regenerator to the cold heat exchanger X_L into the pulse-tube and back [203]. The cycle is divided into four steps and it is assumed that the orifice is closed during steps 1 and 3 and open during steps 2 and 4.

Step 1. The high-pressure valve is opened, the gas element moves through the regenerator towards the cold heat exchanger X_L and enters the pulse-tube at temperature T_L. After that, the gas element is adiabatically compressed during its travel towards the closed orifice and its temperature and pressure increase.

Step 2. The orifice is opened and the pressure inside the buffer volume is lower than the pressure in the tube. Hence, the gas element flows rightward at constant temperature and pressure.

Step 3. The low-pressure valve is opened, the orifice is closed, the pressure inside the tube decreases and expansion takes place. The gas parcel enters the pulse-tube and its pressure gradually decreases during its path toward X_L. At this point, the gas parcel temperature is lower than T_L.

Step 4. The orifice is open again and the pressure inside the buffer volume becomes higher than in the tube. The gas element continues its way towards X_L. Pressure

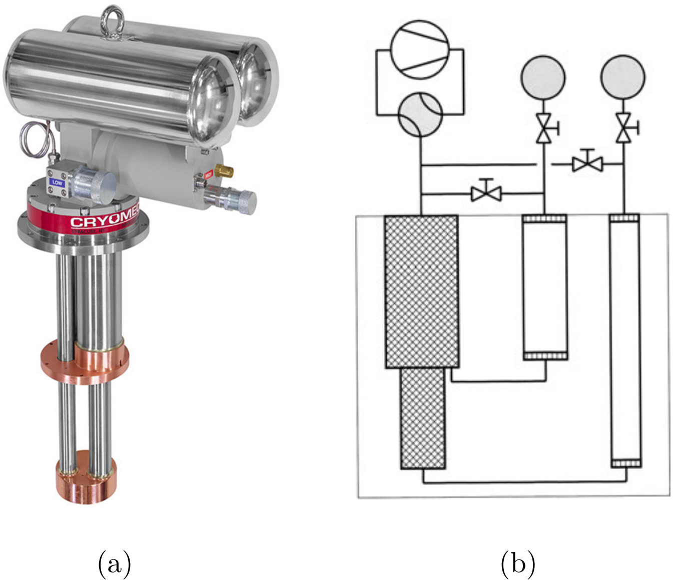

(a) (b)

Figure 3.4: (a) Commercial two-stage double-orifice PT cryocooler with 1 W cooling power at 4 K. The He gas compressor is not shown. Courtesy of Cryomech [214]. (b) Schematic representation of the same kind of PT cryocooler [211]. © A.T.A.M. De Waele

and temperature are constant and the gas element reaches $\mathrm{X_L}$ at a temperature lower than T_L. When passing $\mathrm{X_L}$, the gas warms up to the temperature T_L: the heat amount took away from $\mathrm{X_L}$ by the gas is the cooling power. In the rest of the cycle, the gas element passes over the regenerator and return to its original position.

A commercial two-stage double-orifice PT cryocooler is shown in Fig. 3.4a. Here, one pulse-tube pre-cools the second one, while the hot end of both pulse-tubes is connected to room temperature (Fig. 3.4b). This parallel configuration avoids large heat loads on the cold end of the first stage, which would result from the heat released in the hot heat exchanger of the second pulse-tube [203].

3.4 Additional equipment

A sole cryocooler is not enough to provide the suitable conditions to operate a given device: it is “only” the bare cooling engine. The additional required instrumentation is presented as follows.

3.4.1 Vacuum system

For thermal isolation between room temperature and the cold regions, the cryocooler cold head is installed in a vacuum chamber. This vacuum chamber must be equipped with different accesses (ports) to ambient pressure and temperature. Such ports must be must be leak-tight and are generally used for:

- vacuum pumping and measurement;
- wiring for thermometry and heater;
- wiring for sample bias and measurement;
- other special needs.

The thermal isolation between the cold system and the room temperature environment is acceptable if the pressure in the vacuum chamber is below 10^{-2} Pa. Since the chamber volume is relatively small (often less than $100\,\mathrm{dm}^3$), compact vacuum system with relatively low pumping speed ($50\,\mathrm{dm}^3\,\mathrm{s}^{-1}$ to $80\,\mathrm{dm}^3\,\mathrm{s}^{-1}$) are adequate [215]. Pressure sensors are generally integrated into the system.

3.4.2 Thermometry

Several kind of sensors for low temperature measurement exist and are commercialized [216]. Most widespread cryogenic thermometers are resistors (germanium, Cernox®), diodes (Si, GaAlAs), and thermocouples.

Germanium resistors have the highest accuracy, reproducibility and sensitivity from 0.05 K to 100 K. Cernox® sensors can be used from 100 mK to 420 K with good sensitivity over the whole range. Standard calibration curves for germanium and Cernox® resistors do not exist, hence they require to be calibrated. Silicon diodes are the best choice for general-purpose cryogenic use: they follow a standard curve (from 2 K to 300 K) and are available in robust mounting packages and probes. GaAlAs diodes are similar to Si ones, but do not follow a standard curve. Finally, thermocouples follow a standard curve and can be used over a wide temperature range and in harsh environmental conditions [216]. However, they exhibit a relative poor sensitivity below 10 K and need special techniques for installation.

For monitoring and controlling the temperature of these sensors, different instruments are commercialized, which are generally capable of measuring more sensors simultaneously. Usually, the standard calibration curves are digitally stored in the controller, whereas custom calibration curves can be stored by the user. To set the temperature at a given value, one or more control loops are integrated, providing a power output (up to 100 W) calculated from a proportional-integrative-differential (PID) process. This output must be connected to a heating resistor located to the cold stage to be controlled: its temperature will be stable when the available cooling power at this stage is counterbalanced by the heating power provided by the controller.

3.5 Enhancing thermal performances of cryocooled devices

3.5.1 Optimizing heat transmission

Compared to LHe systems, one of the main downsides of cryocoolers is that a careful thermal design of the cryopackage containing the device is needed: the heat generated inside the device has to be dissipated to avoid the increase of its temperature and the appearance of thermal gradients across it. In bath cryostats, this excess heat is easily dissipated thanks to the high thermal conductivity of the liquid cryogen. This is not the case of cryocoolers working in high-vacuum conditions. Therefore, in order to enhance the heat transmission in cryogen-free systems, the device must be thermally linked to the cryocooler cold region by means of high thermal conductivity materials: oxygen-free high conductivity (OFHC) copper is the best choice in terms of performances and cost. Attention has to be paid also to the thermal contact resistance R_k between different layers, causing a temperature drop ΔT given by:

$$\Delta T = R_k \, Q \tag{3.1}$$

where Q is the heat flowing through the contact area [217]. R_k is inversely proportional to the actual contact area between the two layers, which is much less than the apparent contact area because of the surfaces microscopic irregularities. A “filler” material, e.g. vacuum grease, or a highly deformable pure metal foil , e.g. indium, can be used to fill the void spaces and increase the actual contact area. Applying a moderate force between surfaces is an alternative way to increase the contact area and, hence, to reduce R_k.

3.5.2 Minimizing heat loads

Since cryocoolers have relatively low cooling powers (around 1 W at 4 K), direct thermal links to the room temperature environment should limited. For instance, the coaxial cable or the waveguide for the rf field transmission to a JVS chip is typically made of a good thermal conductor, which then transfers large heat amounts. Thermal anchorings to the cryocooler first stage reduce heat flow and temperature gradients [218]. Furthermore, radiating shields around low temperature areas reduce heat from radiated power that would otherwise limit cooling effectiveness and create temperature inhomogeneities. As for the low-current wirings from room temperature to the device in the coldest region, thin threads of constantan or manganin are best choices, due to their low thermal conductivity and for the low temperature dependence of the electrical properties [207]. On the other hand, if large currents have to be drawn, copper cables represent the best solution [215]. However, in both cases, wires and flexible cables should be suitably wounded around the cryocooler cold head, with the aim of gradually dissipating the heat along their path to the coldest region.

Chapter 4

Dynamic analysis of a Gifford-McMahon cryocooler

This chapter deals with the dynamical analysis of a two-stage Gifford-McMahon (GM) cryocooler as a linear system over a limited temperature range around 4 K. This method is useful to develop a model describing the thermal behavior of the refrigerator, which can be effective for systematic analysis, design of temperature controllers and development of thermal damping techniques. The determination of the input/output response of the GM cooler has been performed using different techniques in time and frequency domain: these allowed to overcome some measurement difficulties, such as those related to fitting the transient response in output signals and system noise. In addition, the consistency check between the two methods provides a first estimate of the measurement uncertainty.

Parts of this chapter are taken from the manuscript in Ref. [219].

4.1 Background

As mentioned in Ch. 3, the rapid evolution of cryocoolers has widened their fields of application, both in terms of cooling power and temperature requirements [204]. Yet, some specific drawbacks are to be faced, as the periodic fluctuation of the cold stage temperature ($\sim 2\,\mathrm{Hz}$), particularly troublesome for high-sensitivity experiments [220]. Most attempts to reduce these thermal oscillations are generally based on the addition of thermal resistance (R_T) and capacitance (C_T) along the cooling path [221, 222]: the damping is obtained with a thermal analog of the resistance/capacitance network in electrical circuits, namely a low-pass filter with time constant $\tau = R_T\, C_T$ significantly longer than the fluctuation period. Hence, the simplest solution to increase τ is to partially decouple the experiment region from the cryocooler cold finger with an increased thermal resistance R_T, usually employing stainless steel [223] and plastic materials [224]. Nevertheless, the additional thermal resistance reduces heat transmission to the experiment part and, hence, the performances of the refrigerator. A high C_T element is then necessary to provide suitable damping, though the reduced specific heat of all materials at cryogenic temperatures makes this extremely difficult. Solid state materials with this property, as erbium or ceramic materials, can be employed to increase the thermal capacitance, though a He-gas pot tightened to the cold finger surface represents the most effective solution [225]. These are capable of damping thermal oscillations from a few hundreds mK of bare cryocooler down to less than 10 mK. Nevertheless, all the proposed dampers exhibit some disadvantages: a longer time is required to cool down the decoupled mass [226] and, as regards the He-pot, the retrofitting of a cooler is expensive or even unfeasible.

Thermal dampers are usually developed on empirical bases, where the effect is first estimated and, then, experimentally evaluated. However, in order to design optimized passive dampers and/or develop active feedback techniques, a dynamical model of the cryocooler thermal response would be advantageous. In this context, papers in the literature are generally aimed at simulating the overall cryocooler behavior [227, 211], in some cases including both mechanical and thermodynamic aspects [228]. Owing to their complexity, these models are studied with numerical methods [229], making it too hard to apply linear dynamical system theory and express the relationship between applied power and temperature by a transfer function.

4.2 Measurement method

Cryocoolers are complex thermal machines, far from linear behavior [228]. However, in most practical cases, the analysis of the cryocooler response around a stable point is required, which allows to assume that the parameters describing the system are subject to limited variations. The physical model is then linearized around a stable point and, hence, linear system theory can be applied.

According to the theory, a linear dynamic system can be completely described either from the output to a proper time dependent input signal or by spectral analysis. A step-shaped input is commonly used to measure the system transfer function, given by the complex ratio between output and input. Such step stimulus is easy to generate and, at the same time, its spectral content includes all frequencies. This technique is particularly useful to characterize thermal systems where long time constants may occur and to provide information about the thermal flow path [230].

A second technique has been used to check the measurement effectiveness: it consists in the analysis of the cryocooler response to a sinusoidal input power. Since linear system theory guarantees that the response to a sinusoidal input is sinusoidal with the same frequency [231], the voltage across the temperature sensor

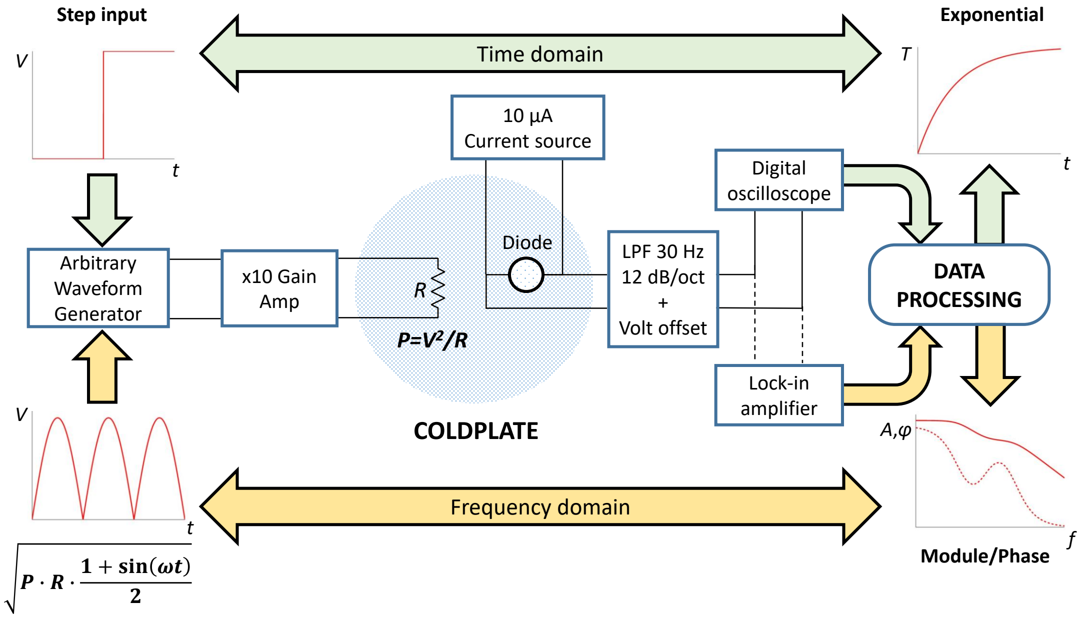

Figure 4.1: Schematic representation of the measurements performed for the dynamic characterization of the GM cryocooler.

was measured with a lock-in amplifier, after being properly filtered and amplified. Lock-in technique allows to reliably determine magnitude and phase of the output signal component at the frequency of interest, i.e. the same of the input signal, thus providing a straightforward estimation of the cryocooler transfer function.

4.3 Experimental setup

A schematic representation of the measurement setup is shown in Fig. 4.1. The cryocooler under study was a two-stage GM (Leybold Coolpower 4.2GM [232]), with cooling power of 1 W at 4.2 K and minimum temperature below 3 K with no thermal load. To augment the useful cold surface and avoid the wear of the cold finger, an OFHC copper disk, the "coldplate" henceforth, was carefully tightened to the latter, with a thin layer of vacuum grease (Apiezon N [233]) at the interface to further improve thermal contact. A $\sim 70\,\Omega$ heating wire made of manganin is wound around the coldplate, whereas a second heater, realized with a SMD resistor ($330\,\Omega$ nominal value, $340\,\Omega$ measured value at 4 K), was placed in the center of the coldplate. Two calibrated silicon diodes [216] and a Lake Shore 350 controller [234] were used for temperature measurements. As shown in Fig. 4.2, the SMD resistor and the diodes are tightened to the coldplate by means of brass screws. The second

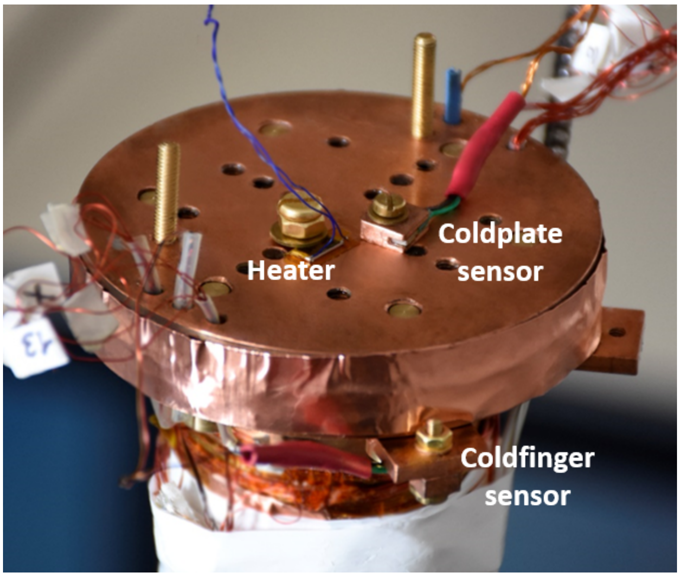

Figure 4.2: Photograph of the GM cryocooler coldplate, showing the temperature sensors and the SMD heater used in the measurement. The manganin wire wound around the coldplate is covered by a protective copper tape.

diode, placed in direct thermal contact with the cold finger, allows to assess the effectiveness of the grease thermal interface by comparing the temperature of the diodes. No appreciable difference has been detected, meaning that coldplate and cold finger are thermally shorted and, hence, can be treated as a single Cu block. A constant current was fed through the 70 Ω manganin wire for heating the coldplate up to approximately 4 K. The time-dependent input stimulus, provided by an AWG (Agilent 33250A [235]) and subsequently amplified, was applied instead across the SMD resistor.

Owing to the limited sampling time, common temperature controllers employed in cryogenics are not suitable to observe fast transients. To circumvent such limitation, diodes were directly current-biased at 10 µA by means of high accuracy current sources (Keithley 6220 [236]) and the resulting voltage was measured, after being amplified and filtered of frequencies greater than 30 Hz with a differential preamplifier (SRS-SR560 [237]). A dc compensation voltage was provided to cancel out the diode voltage offset: compared to ac-coupling, this method allows to avoid any low frequency cut-off, which is of fundamental importance when long transients have to be observed. To do this, diode voltage and compensation voltage, provided by a stable dc source (Agilent 6634B [238]), were applied at the non-inverting and inverting inputs of the low-noise differential amplifier, respectively. Furthermore, removing the offset improves signal-to-noise ratio (SNR), since the gain of the differential amplifier can be increased without saturating. Finally, differential amplification guarantees high rejection to common-mode electrical noise.

4.3.1 Time domain

In the time-domain analysis, a 10 mHz rectangular voltage signal is applied across the SMD resistor to provide the power input stimulus to the system. Low and high levels of this square wave were set to 0 V and 8 V, respectively. The high-level voltage was carefully chosen to simultaneously maximize SNR and maintain the coldplate temperature around 4 K, hence keeping the system in the linear regime. A LeCroy HDO6034 digital oscilloscope [239] was employed to sample and average the voltage of the diodes. The temperature response was then obtained by post-processing the acquired data with the use of the diodes voltage-to-temperature calibration curve.

4.3.2 Frequency domain

In the frequency domain analysis, the sinusoidally-varying power input was again generated by the SMD heater. In particular, as shown in the low-left side of Fig. 4.1, a sine-shaped power stimulus with frequency f and values from zero to P_{max} was obtained by programming the AWG to source the time-dependent voltage function

$$V(t) = \sqrt{P_{max}\, R\, \frac{1 + \sin(2\pi\, f\, t)}{2}} \tag{4.1}$$

where R is the SMD heater resistance. A Signal Recovery 7265 DSP lock-in amplifier [240] has been employed to measured magnitude and relative phase of the output component at the same frequency of the input signal, thus allowing to determine the transfer function in the frequency range from 25 mHz to 10 Hz. For higher frequencies, the expected sinusoidal response is very hard to observe, since the cryocooler noise is higher than the thermal variation resulting from the input power. Optimal rejection of this noise has been achieved by averaging the demodulated signal over several period of the reference, accomplished by setting the time constant of the output integrating filter to a value five times higher. Again, the amplitude of the input voltage (13 V) was carefully chosen to simultaneously optimize the SNR and maintaining the system in the linear range.

4.4 Results

4.4.1 Step response analysis

In time-domain, the response of a linear system (ΔT in this case) to a step input is described by a sum of exponential decays

$$\Delta T(t) = \sum_{i=1}^{n} A_i\,(1 - e^{-t/\tau_i}) \tag{4.2}$$

with A_i and τ_i amplitude and time constant of the i^{th} decay contribution, respectively. The number of terms n depends on system complexity and, for this reason, has to be determined *a posteriori*. Best-fit analysis of the measured temperature variations ΔT shows that optimal results occur with $n = 2$ and $n = 3$. Tab. 4.1 reports the values of best-fitting parameters for $n = 2$ and $n = 3$, i.e. normalized amplitudes $a_i = A_i/P$ and time constants τ_i, determined from both rising and falling steps of the periodic input. Experimental data and fitting functions are displayed in Fig. 4.3, with the inset highlighting the initial part of the system response, where the fast rising exponential term can be observed.

Table 4.1: Sum of n exponential functions parameters that best fit the normalized step response.

	a_1	a_2	a_3	τ_1	τ_2	τ_3
		$(\mathrm{K\,W^{-1}})$			(s)	
$n = 2$	0.173	1.378	-	0.086	6.629	-
$n = 3$	0.160	0.910	0.526	0.053	4.861	13.014

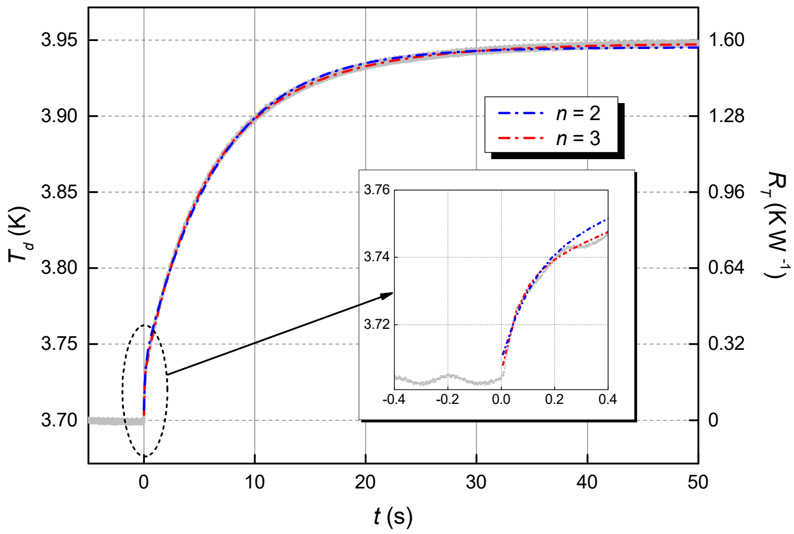

Figure 4.3: Experimental cryocooler step response and exponential fitting functions with $n = 2$ (blue) and $n = 3$ (red). Right y axis scale reports the incremental system response normalized to a unit step input, physically a thermal resistance (R_T).

Nevertheless, a linear system is most appropriately described by the "pulse response", given by the time derivative of the step response [231]. Time derivative of Eq. 4.2 is

$$\frac{d}{dt}\sum_{i=1}^{n} A_i(1-e^{-t/\tau_i}) = \sum_{i=1}^{n} \frac{A_i}{\tau_i}\, e^{-t/\tau_i} \tag{4.3}$$

from which emerges that each term is weighted by the corresponding time constant τ_i. This leads to the normalized pulse response parameters a_i/τ_i reported in Tab. 4.2, which are separated by approximately one order of magnitude from each other. Consequently, amplitude a_3/τ_3 can be neglected. Moreover, the amplitudes obtained for $n = 2$ and 3 are in good agreement for both a_1/τ_1 and a_2/τ_2. Therefore, it can be stated that the cryocooler thermal response can be suitably described by a linear dynamical system with a second order input-output (power-temperature) relation.

The measured temperature increment ΔT has been also checked against the cryocooler specifications, outlined in the load-capacity map in Fig. 4.4 [241]. Around the operating point, i.e. 4 K second stage heat load, the temperature increase per unit of power is $\Delta T/\Delta P = 0.7/0.5 = 1.4\ \mathrm{K\,W^{-1}}$, extracted from the 0.5-1 W map segment (0 W first stage heat load, red line in the plot). The same parameter, obtained from the step response measurements, gives $\Delta T/\Delta P = 0.242/0.157 = 1.54\ \mathrm{K\,W^{-1}}$, which is in good agreement with the nominal one, taking into account that the cryocooler performances may have been slightly degraded over time.

Table 4.2: Parameters describing the time-derivative of the normalized step response exponential fit.

	a_1/τ_1 (K W^{-1} s^{-1})	a_2/τ_2 (K W^{-1} s^{-1})	a_3/τ_3 (K W^{-1} s^{-1})
$n = 2$	2.012	0.205	-
$n = 3$	3.026	0.185	0.038

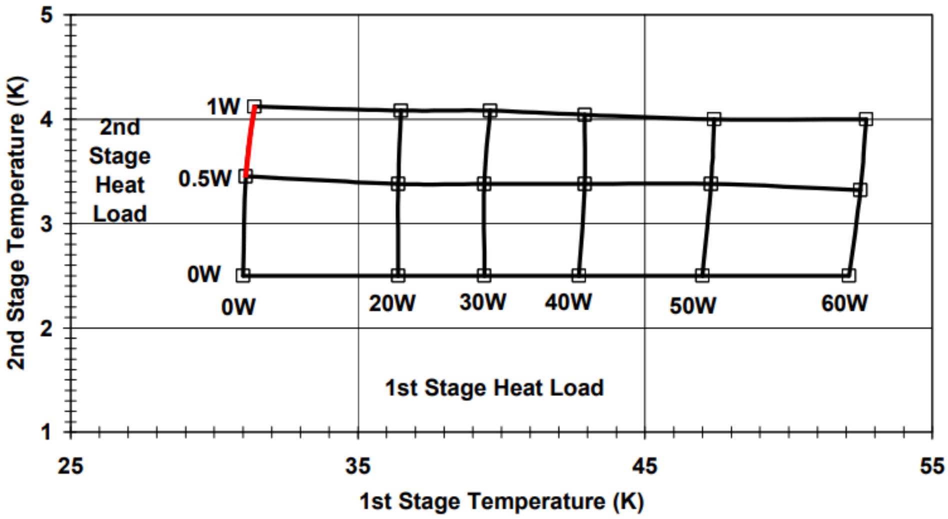

Figure 4.4: Leybold Coolpower 4.2 GM 1 W capacity map for 50 Hz mains frequency. The red segment indicates the range of interest for this study [241]. Courtesy of Oerlikon Leybold Vacuum.

4.4.2 Frequency response analysis

In frequency domain experiments, amplitude and relative phase of the oscillating temperature variation, resulting from the applied sinusoidal power, is measured at frequencies values equally spaced in a logarithmic plot. To remove the offset in phase measurement, data have been corrected to obtain zero degrees at the lowest frequency, as required by theory. Therefore, it was assumed that the cryocooler dynamical response observed with a 25 mHz input stimulus is the same as with a constant input.

As anticipated, with the purpose of reducing noise at the input of the lock-in amplifier, the voltage signal from the diode was low-pass filtered by means of the differential pre-amplifier (Fig. 4.1). Since the effect of the filter, set to 30 Hz cut-off and 12 dB/octave roll-off, is not negligible at the frequencies of interest, data measured at higher frequencies have been suitably post-corrected to compensate this contribution, as illustrated in Fig. 4.5.

The cryocooler transfer function has been then evaluated by fitting the corrected frequency response, hence giving

$$H(s) = \frac{1.7\,(1 + s/1.76)}{(1 + s/0.153)\,(1 + s/11.9)} \tag{4.4}$$

Observing Eq. 4.4, it can be stated that the cryocooler behaves as a second order system, with zero at $z = 1.76/2\pi = 280$ mHz and poles at $p_1 = 0.153/2\pi = 24$ mHz and $p_2 = 11.9/2\pi = 1.9$ Hz.

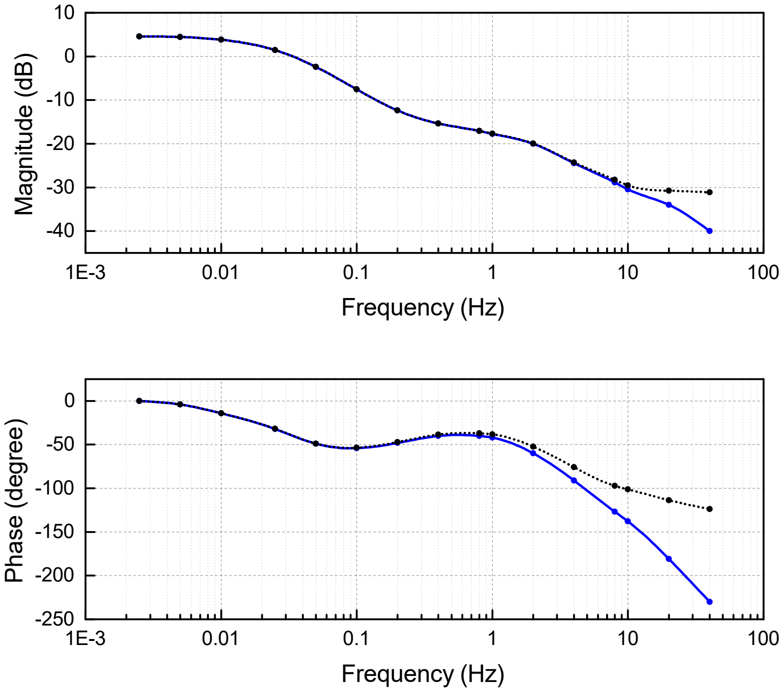

Figure 4.5: Magnitude and phase plots of the measured cryocooler frequency response (blue line and marks) and frequency response corrected to compensate the effect of the low-pass filter (black dotted line and marks).

The accuracy of the fit provided by Eq. 4.4 is clearly verifiable in Fig. 4.6, though, in the phase plot, measured data and fitted values differ by an approximately constant offset. This deviation can be justified considering the previous discussion on the difficulties in the determining the absolute phase difference, solved setting to zero the phase of the lowest frequency value. Eventually, the residual offset shows that the assumption was not correct and, hence, that the phase of the transfer function must approach zero at lower frequencies than initially guessed. A second discrepancy between data and fit is observed in the higher frequency range, which can be explained by the high input-output attenuation with respect to the response to a constant input and, as a consequence, by the very low measured signals. Therefore, data at frequencies greater than ~5 Hz are not reliable and hidden by a noise floor distinctly observable in the magnitude plot.

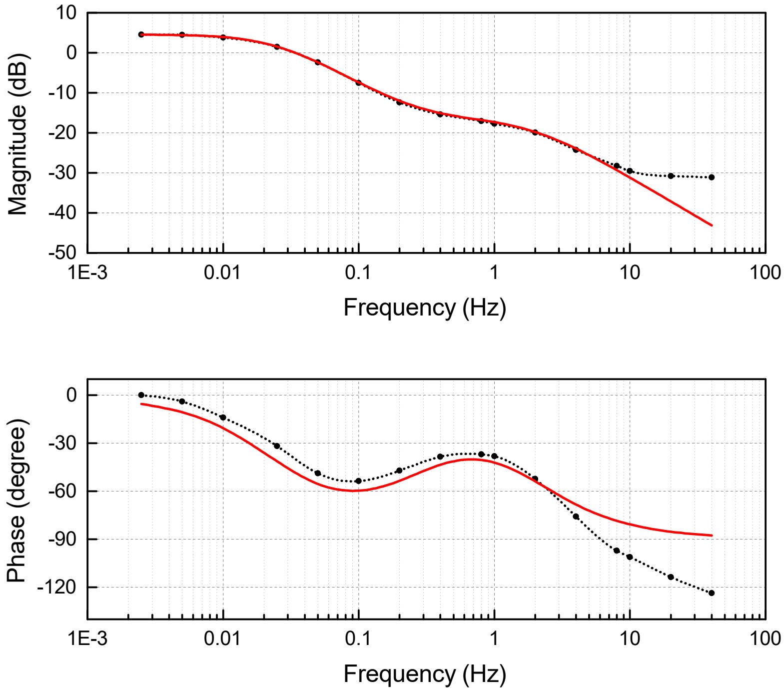

Figure 4.6: Magnitude and phase plots of the corrected frequency response data (black dotted line and marks) and fitting function (red line).

4.5 Comparative analysis of time and frequency domain approaches

As known from theory [231], results obtained with either time or frequency analysis of the system response can be derived from each other. Yet, this does not mean that either one of these approaches can be chosen arbitrarily. For example, the lock-in technique is particularly efficient in noise rejection, allowing to reliably filter the interference from mains and, in this specific case, the cryocooler thermal oscillations. On the other hand, time domain measurements are simpler, though a step response averaging over several hours is needed to achieve an equivalent filtering effect. Hence, the choice of the most suitable solution depends on the required accuracy and should be evaluated on a case-to-case basis. Even though a detailed analysis of data statistics and model approximations would be necessary to perform a rigorous uncertainty estimation, a direct comparison of results obtained with two different techniques allows to derive a first evaluation of the uncertainty. For this purpose, the pulse response of the system has been derived by calculating the inverse Laplace transform of $H(s)$, which can be written as

$$\mathcal{L}^{-1}\left(H(s)\right) = \frac{a'_1}{\tau'_1}\, e^{-t/\tau'_1} + \frac{a'_2}{\tau'_2}\, e^{-t/\tau'_2} \tag{4.5}$$

Time constants are equal to the reciprocal of the two $H(s)$ poles' angular frequencies, i.e. $\tau'_1 = 1/11.9 = 0.084\,\mathrm{s}$, $\tau'_2 = 1/0.153 = 6.54\,\mathrm{s}$, with both values in good agreement with those obtained in time domain analysis (Tab. 4.1). The weighting coefficients are calculated via the following equations

$$\begin{aligned}\frac{a'_1}{\tau'_1} &= C\,\frac{1/\tau'_1 - z}{1/\tau'_1 - 1/\tau'_2} = 1.52\\ \frac{a'_2}{\tau'_2} &= C\,\frac{z - 1/\tau'_2}{1/\tau'_1 - 1/\tau'_2} = 0.24\end{aligned}$$

with $C = \lim_{s\to\infty} H(s) = 1.76$, i.e. the initial value theorem. It can be noticed that these values are quite different from those listed in Tab. 4.2, probably due to the $\sim 40\,\%$ experimental standard deviation of the latter. Therefore, the combined uncertainty of the two measurement systems largely explain the differences between the results in time and frequency domain.

4.6 Summary and future work

A thorough study of the thermal properties of a GM cryocooler in non-stationary conditions has been performed according to linear system theory. System parameters have been derived with suitable accuracy via time and frequency domain analysis, thus providing a cross validation of the obtained information and a first uncertainty estimation. Furthermore, the self consistency of both results demonstrates that a lumped model provides an adequate representation of the cryocooler dynamic thermal properties, with interesting applications to temperature control, simulation and design of thermal dampers.

First attempts to actively compensate the cryocooler thermal fluctuations with a programmed power function, determined from the temperature-to-power transfer function $H(s)$ and the oscillating temperature profile, showed that, at 4 K, the amount of power required by the system is greater than the refrigerating power. Further investigation is then planned to analyze the cryocooler behavior at higher temperatures and different frequencies of the cryocooler displacer motion.

Chapter 5

Investigation on programmable Josephson standards at INRiM

In the last years, research on PJVS devices at INRiM has been mainly focused on the implementation of a PJVS cryocooled system and on the development of alternative bias techniques. To meet these goals, several tasks had to be addressed, among which the realization of a cryopackage suitable for the PJVS dry operation and the development of a software for its proper electrical polarization are the most relevant. In this scope, the main activities carried out in accomplishment of this thesis are presented here.

Parts of this chapter are extracted from the manuscripts in Refs. [242], [243], [244] and [245].

5.1 Employed PJVS device

The PJVS chips employed at INRiM (Fig. 5.1) were developed in cooperation with PTB [148] and contain 8192 SNIS Josephson junctions subdivided into 14 segments. These devices are typically rf-biased at 70 GHz and, hence, provide output voltages from $-1.2\,\mathrm{V}$ to $1.2\,\mathrm{V}$ with a minimum increment of approximately $150\,\mu\mathrm{V}$, thus acting as a 13-bit + sign quantum DAC. The entire array is arranged over

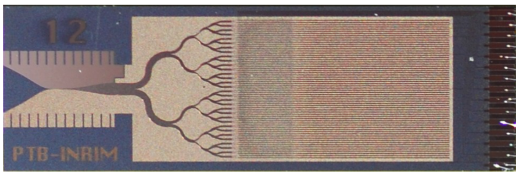

Figure 5.1: 1 V PJVS chip with 8192 SNIS Josephson junctions. The chip size is $5.5 \times 15 \times 0.5\ \mathrm{mm}^3$. Courtesy of Luca Callegaro.

32 parallel microstriplines of 256 junctions each. Starting from the low potential point, the total number of junctions is distributed among the 14 sub-arrays following N_s = [64, 32, 16, 8, 4, 2, 1, 1, 128, 256, 512, 1024, 2048, 4096]: this apparently atypical arrangement of junctions optimizes the rf signal transmission along the first microstripline, which contains the sub-arrays from "64" to the second "1". A detailed explanation of this fact is given in Ref. [246]. The two independent single-junction segments enable the splitting of the full array into two equal branches, with 4096 junctions each. This feature is useful to perform accurate quantization tests, where one branch is biased on the positive quantum step and the other on the negative one, such that the sum should be exactly zero.

5.2 Development and thermal analysis of a cryopackage for PJVS

As discussed in Chap. 3, cryogenics-related complexities still limit the spread of JVSs outside NMIs. Cryocooler systems then bear a particular interest, although several issues related to power dissipation arise. Due to the low bias currents employed, the dissipated power is negligible in conventional SIS arrays, for which integration in cryocooler has been already demonstrated more than twenty years ago [247]. In contrast, thermal issues are more challenging in ac JVSs, since a larger amount of rf power is required to generate suitable voltage steps. In addition, bias currents are needed to drive junctions on a given quantum step, thus contributing to the increase of the overall heat generated inside the chip. To guarantee proper operation of the Josephson device, this excess heat has to be transferred to the sample holder and, then, to the cryocooler second stage via suitable thermal links. At cryogenic temperature, heat conduction across the interface between two solids largely depends on the quality of the surfaces: if these are perfectly flat, the unique limitation to heat flux is represented by thermal boundary resistance [248], also known as Kapitza resistance. Differently, the actual contact area is reduced in the case of rough surfaces, hence resulting in a further contribution to the thermal flow resistance. To avoid this, using a solder represents the best approach [249], since it easily fills the empty spaces between the solid surfaces. Yet, some difficulties may occur, as the risk of damaging the chip during the soldering process, possible voids in the solder [250] and failures after repeated thermal cycles [251]. Another possibility to enhance heat transfer is to apply a moderate mechanical pressure between chip and chip-holder, with a high thermal conductivity and soft material placed in between [252]. Indium is generally adopted as thermal interface material [253, 254] in that, owing to its softness and ductility, compensates for the differential thermal expansion between distinct layers.

Following these assumptions, a novel cryopackage for PJVS devices has been realized and its thermal performances have been experimentally investigated in different operating conditions. It can be considered as the evolved version of custom cryopackages previously adopted at INRiM [255, 256, 257].

5.2.1 Structure of the cryopackage

A photograph of the designed cryopackage and its schematic cross-section are shown in Fig. 5.2. The chip, fabricated on a Si substrate, is fitted inside a groove into an OFHC copper block (the base henceforth) with a special 0.1 mm thick Heat-Spring® indium foil [258] interposed at their interface. With the aim of providing clean surfaces, the oxidized layer was mechanically removed from the indium foil and the chip backside was sputter cleaned and covered by a 400 nm thick AuPd metalization layer. A 0.3 mm thick c-plane sapphire substrate is positioned on the upper face of the chip, with thin Apiezon N layers applied at both surfaces. Owing to its specific properties, the sapphire lamina has the double function of providing an additional path for heat transmission by simultaneously avoiding accidental short circuits that a common metal as copper would cause. This sapphire/Si chip/indium 'sandwich" is then carefully pressed against the base by a Cu bridge-like structure. The pressure is exerted by means of a brass screw inserted at the center of the bridge, which in turn transfers the force to a thin flexible Cu slab. An alumina spacer is placed over the slab, so as to prevent the wear that the direct contact with the brass screw would cause.

The operation of this bridge-screw appliance is simple: the force acting on the chip is adjusted by turning the central screw with a calibrated torque screwdriver and via the relation between force and torque, previously determined using a calibrated load cell and approximately linear in the interested force range.

Measurements presented below have been carried out with the two-stage GM refrigerator already presented in Chap. 4. The cryopackage is properly tightened

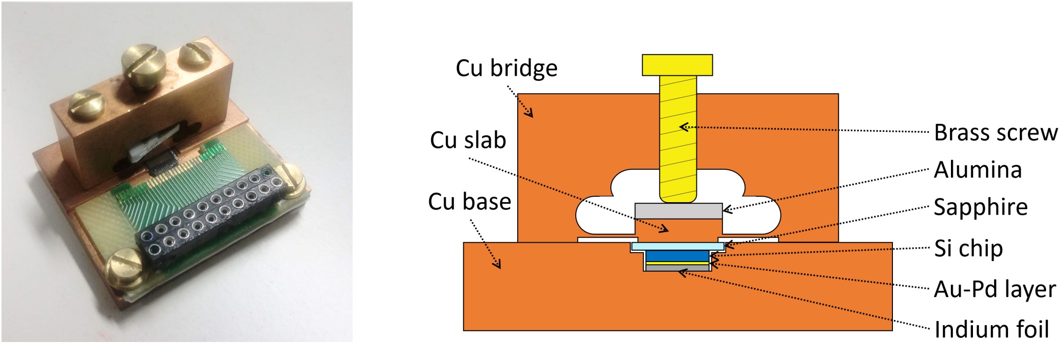

(a) (b)

Figure 5.2: (a) Photograph of the designed cryopackage for PJVS devices and (b) its front-view section (not in scale).

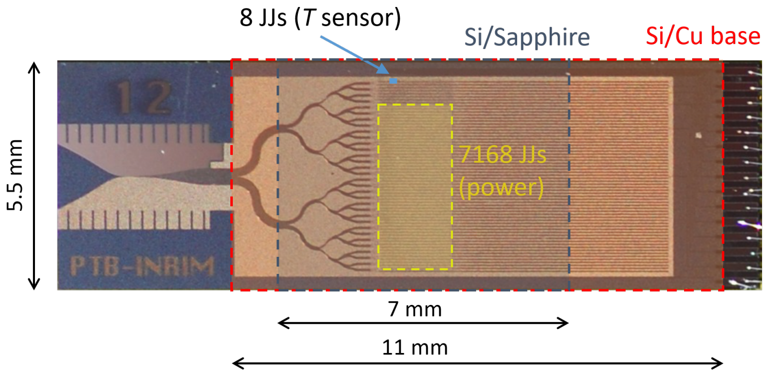

Figure 5.3: Overview of the geometrical properties of the employed PJVS array for the thermal characterization of the cryopackage. Three segments with a total of 7168 junctions (yellow dashed line) were used as power source. A single segment with eight junctions was used as temperature sensor. The red dashed line indicates the chip backside surface in contact with the Cu base (with In and AuPd as interfaces). The blue dashed line indicates the area of the chip upper side in contact with the sapphire lamina (Apiezon N as interface). © 2019 IEEE

onto the cryocooler coldplate, with a thin layer of Apiezon N applied at their interface.

5.2.2 Measurement of the cryopackage thermal resistance

The cryopackage effectiveness has been investigated by using three PJVS segments, counting 7168 junctions in total, to generate a known heat amount by biasing them at currents above the critical current. A single segment with eight junctions was instead operated as on-chip temperature sensor, through the dependence of critical current I_c on junctions temperature T. I_c values were extracted from the observed current-voltage characteristics, obtained with a high-accuracy current source (Keithley 6220 [236]) and a nanovoltmeter (Keithley 2182A [259]). Additional current source (Keithley 220 [260]) and nanovoltmeter (Keithley 181 [261]) were used to generate and accurately measure the electrical power dissipated in the heating junctions. The $I_c(T)$ dependence of the temperature-sensing subsection was previously measured in cryocooler and with zero power from the heating junctions. A dc current was fed through the manganin heating wire surrounding the coldplate to change its temperature, measured by a calibrated sensor after its stabilization. During this measurement, the temperature of the chip was supposed to be the same as the coldplate, since very low heat flows at the interface. The $I_c(T)$ experimental curve is shown in Fig. 5.4: it is satisfactorily expressed by the power equation $I_c(T) = I_0\,(1 - T/T_c)^a$, with $I_0 = 12.6\,\text{mA}$, $T_c = 8.18\,\text{K}$ and $a = 1.62$,

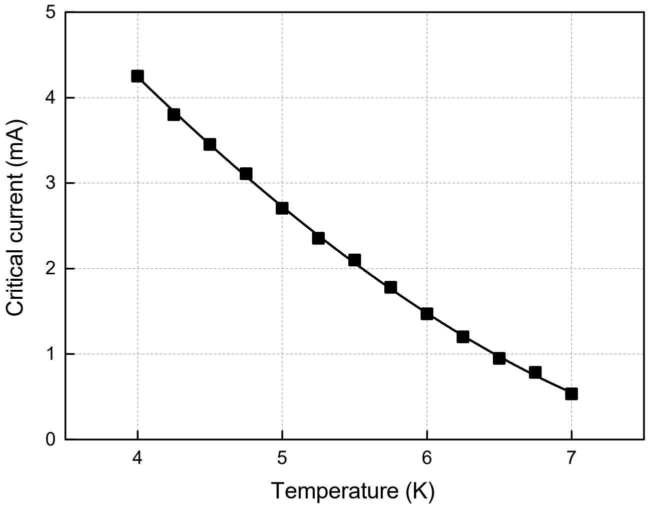

Figure 5.4: Critical current versus temperature of the eight junctions segment. The experimental points are well fitted with the power function described in the text.

and it has been used for the chip temperature determination. Finally, the thermal resistance R of the cryopackage is determined as the ratio between induced temperature increase (ΔT) and applied electrical power (P).

5.2.3 Results

Dependence on mechanical pressure

The overall thermal resistance R has been measured at increasing pressures and at different operating temperatures, set via the PID closed-loop control function of the employed temperature measurement device (Lake Shore 350, [234]). The exerted pressure was evaluated considering the Si-In-Cu contact surface ($5.5\,\mathrm{mm} \times 11\,\mathrm{mm} = 60.5\,\mathrm{mm}^2$, red dashed line in Fig. 5.3). Results are shown in Fig. 5.5: as foreseen, both temperature and pressure affect the cryopackage thermal resistance, which decreases with the latter following an almost linear trend. Error bars are evaluated from the measured thermal fluctuation of the coldplate and, as a consequence, are larger at higher temperature.

With a similar thermal structure, researchers at Supracon AG measured a thermal resistance $R \simeq 3.3\,\mathrm{K\,W^{-1}}$ at 4.2 K with a 10 V PJVS, hence with a larger contact area [136]. In that case, a sapphire substrate was bonded on the chip backside and thermalized to the coldplate with an In film at the interface. Apiezon N was used for a second thermal contact between the chip and two copper blocks pressing it at the top. The authors did not report the value of the exerted pressure. As described in Ref. [262], NIST researchers used a pressed indium foil as

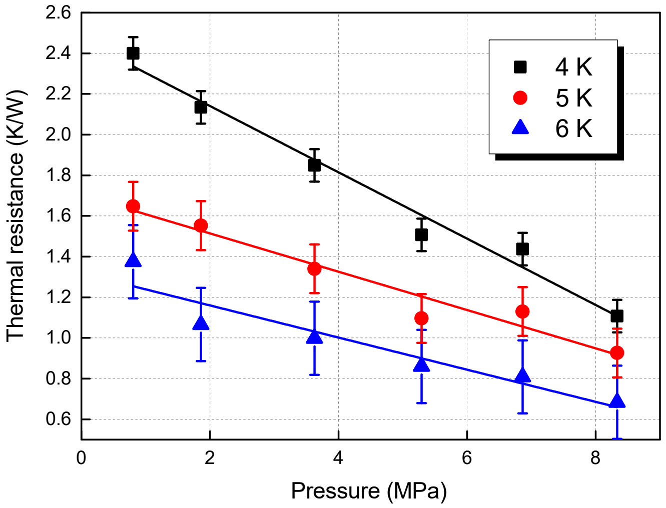

Figure 5.5: Cryopackage thermal resistance versus exerted mechanical pressure at different operating temperatures.

thermal interface material between a 10 V PJVS chip and the Cu holder, obtaining $R \simeq 1.6\,\mathrm{K\,W^{-1}}$ at 3.2 MPa and 4 K, with a $200\,\mathrm{mm^2}$ contact surface. By multiplying the measured thermal resistance (R) per the contact surface between chip and base (A), a parameter independent on the size of the latter is obtained. In our case, $R \cdot A = 1.9\,\mathrm{K\,W^{-1}} \cdot 0.605\,\mathrm{cm^2} = 1.1\,\mathrm{K\,cm^2\,W^{-1}}$ at 4 K and 3.2 MPa (same pressure applied in Ref. [262]), whereas the NIST cryopackage gives $R \cdot A = 3.2\,\mathrm{K\,cm^2\,W^{-1}}$. The lower $R \cdot A$ value obtained with our cryopackage is likely associated to the additional upward heat conduction through the sapphire and the special indium foil.

Owing to the sandwich structure, the total thermal resistance R is the sum of resistances of bulk layers (R_i) and interfaces between them. The thermal resistance of the bulk layers has been evaluated via heat transfer equation

$$R_i = \left(k_i\,\frac{A_i}{d_i}\right)^{-1} \tag{5.1}$$

where k_i, A_i and d_i are thermal conductivity, surface and thickness of the layer i, respectively. For each layer it is assumed $A_i = 5.5\,\mathrm{mm} \times 7\,\mathrm{mm} = 38.5\,\mathrm{mm^2}$, namely the smaller contact area in the sandwich. Therefore, a worst case is considered. The estimated thermal resistance values at 4 K are $R_{\mathrm{Si}} \simeq 0.13\,\mathrm{K\,W^{-1}}$ for the Si chip ($k_{\mathrm{Si}} \simeq 1\,\mathrm{W\,K^{-1}\,cm^{-1}}$ for the employed Si substrate [263] and $d_{\mathrm{Si}} = 0.5\,\mathrm{mm}$), and $R_{\mathrm{sapph}} \simeq 0.078\,\mathrm{K\,W^{-1}}$ for sapphire ($k_{\mathrm{sapph}} \simeq 1\,\mathrm{W\,K^{-1}\,cm^{-1}}$ [207] and $d_{\mathrm{sapph}} = 0.3\,\mathrm{mm}$). The thermal conductivity for the Heat-Spring® indium has been evaluated via Wiedemann-Franz law

$$k_{\mathrm{In}} = L\,\frac{T}{\rho_{In}} \tag{5.2}$$

with the empirical constant $L = 2.44 \times 10^{-8}\,\mathrm{W\,\Omega\,K^{-2}}$, known as Lorentz number, and resistivity ρ_{In} experimentally determined at 4 K. With $k_{\mathrm{In}} \simeq 6\,\mathrm{W\,K^{-1}\,cm^{-1}}$ and $d_{\mathrm{In}} = 0.1\,\mathrm{mm}$, the thermal resistance for In is then $R_{\mathrm{In}} \simeq 0.004\,\mathrm{K\,W^{-1}}$. An important contribution may derive from the thin vacuum grease layers between the Si-sapphire and Cu-sapphire interfaces. The thickness of these layers was estimated by exerting an increasing pressure from 0.5 to 6 MPa on a thin layer of Apiezon N flattened between two sapphire lamellae. For pressures above 1 MPa, the thickness was lower than 1 µm, thus implying $R_{\mathrm{Apiezon}} \simeq 0.065\,\mathrm{K\,W^{-1}}$ with $k_{\mathrm{Apiezon}} \simeq 0.004\,\mathrm{W\,K^{-1}\,cm^{-1}}$ [264]. Because of the very low thickness of the AuPd layer, its contribution is neglected. The sum of these bulk-layers resistances ($\sim 0.34\,\mathrm{K\,W^{-1}}$) is lower than the experimental values (Fig. 5.5), thus confirming that the major contribution to the cryopackage thermal resistance is represented by the interfaces between the bulk elements.

Effect of the additional top conductance

The effectiveness of the sapphire substrate as additional heat-flow path has been assessed by replacing it with a fused-silica lamina of the same thickness. This prevents the heat be dissipated via the upper face of the chip, since fused-silica thermal conductivity is four orders of magnitude lower than that of sapphire [207]. The test has been performed at about 8.3 MPa, which corresponds to the highest pressure employed in the previous analysis. To avoid possible systematic errors, a new indium foil has been used in this second experiment. Indeed, in the employed pressure range, the indium foil does not return in its initial shape and, hence, its reliability is ensured only when pressure is further increased. The experimental ΔT versus P data points are displayed in Fig. 5.6, in the two scenarios of enabled (sapphire) and disabled (fused-silica) top conduction.

To give a size of the effect of the enabled top conduction, the cryopackage thermal system can be interpreted with its analog electrical circuit, made of two parallel-connected resistances R_t and R_b, representing respectively the top and the bottom paths. The equivalent resistance of this circuit (R_{tb}) is that determined in Sec. 5.2.3, with the sapphire lamina placed over the chip. Substituting sapphire with fused-silica allows the determination of the single bottom resistance R_b and, consequently, of single top resistance via $R_t = R_{tb}\,R_b/(R_b - R_{tb})$. The results, listed in Tab. 5.1, confirm that enabling top conduction with sapphire provides a significant contribution to the total heat dissipation, i.e. from +30 % at 4 K up to +60 % at 6 K.

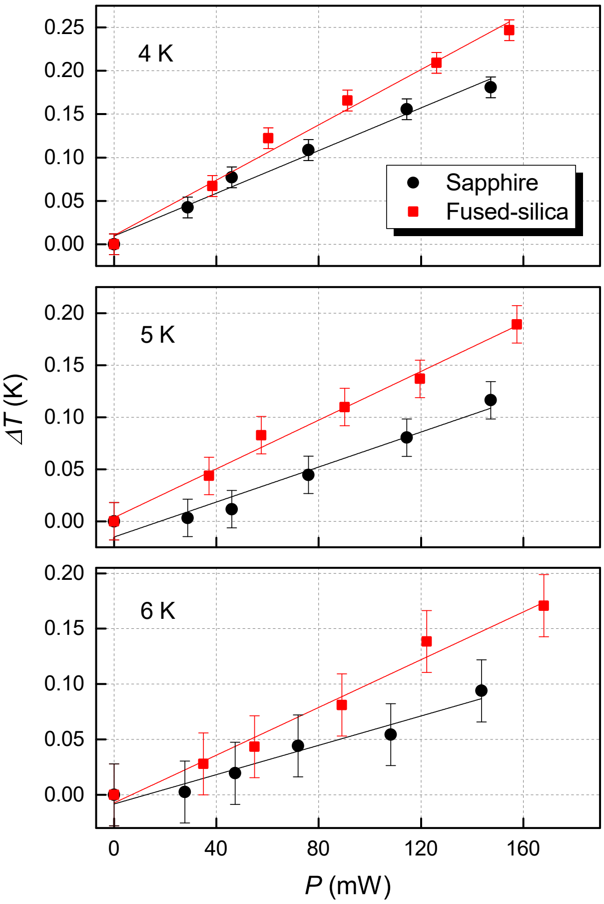

Figure 5.6: Temperature variation ΔT induced by the applied electrical power P with sapphire and fused-silica placed between chip and pressing bridge. Data have been taken at temperatures of 4, 5 and 6 K and mechanical pressure of 8.3 MPa.

Table 5.1: Cryopackage thermal resistance contributions at 8.3 MPa. © 2019 IEEE

T (K)	R_{tb} (K W^{-1})	R_b (K W^{-1})	R_t (K W^{-1})	R_b/R_{tb}
4	1.23	1.59	5.43	1.29
5	0.84	1.17	2.98	1.39
6	0.66	1.08	1.70	1.64

Estimation of the actual pressure at low temperature

It is clear that the extent of the force pressing the chip is set at room temperature. Nevertheless, at cryogenic temperatures the actual pressure may be higher or lower with respect to that applied before the cooling, as a consequence of the different thermal contraction/expansion of its components. This effect has been approximately estimated using the coefficients of thermal expansion to calculate the thickness variations of each cryopackage layer. The elements that may contribute to a pressure change and the corresponding thickness value at room temperature are listed in Fig. 5.7. The parameter $\delta = \Delta_{\mathrm{Cu}} - \sum_{\mathrm{i}} \Delta_{\mathrm{i}}$, i.e. the difference between the thickness variation of the relevant Cu part (Δ_{Cu}) and that of the internal components (Δ_{i}), has been estimated. The contribution of the AuPd layer is again neglected. Tab. 5.2 summarizes the thickness variations Δ between 300 K and 4 K for each element, in accordance with the coefficients of thermal expansion found in Refs. [203, 265, 266, 267]. The calculated δ are $\sim 3.5\,\mu\mathrm{m}$ with the sapphire and $\sim 3.7\,\mu\mathrm{m}$ with the fused silica laminae onto the chip. In both scenarios, δ is positive, which means that the relevant Cu part contraction is larger than that of the inner components, and the exerted pressure grows when the package is cooled.

The amount of such pressure rise has been evaluated both experimentally and via simulation, assuming that the top of the bridge is deformed by δ in the normal direction. At room temperature, the relation between vertical deformation and exerted normal force was found to be approximately linear, from which follows that forces of about 175 N and 185 N, i.e. pressures of 2.9 MPa and 3.1 MPa, are requested to flex the bridge by 3.5 µm and 3.7 µm, respectively. To test the validity of these experimental findings, a SolidWorks simulation of the cryopackage deformation in the elastic regime has been carried out. In this model, the real conditions have been simplified by considering the whole cryopackage as a single copper body and disjointed from the cryocooler coldplate. An upward normal force exerting on the bridge simulates the effect of thermal contraction and, hence, the bridge deformation, whose magnitude is illustrated in Fig. 5.8. It can be seen that, in line with the experimental results, a force of 200 N is required to flex the upper side of the

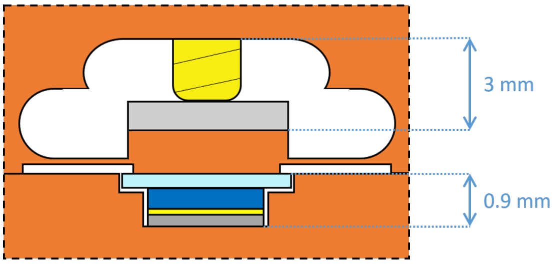

Figure 5.7: Particular of the cryopackage elements contributing to a pressure change between 300 K and 4 K.

Table 5.2: Thickness change of each cryopackage element that may contribute to a pressure change between 300 K and 4 K. More details are given in the text. © 2019 IEEE

Element	Thickness at 300 K (mm)	Thermal contraction coefficient (%)	Variation at 4 K (µm)
	$d_{300\mathrm{K}}$	$\frac{d_{300\mathrm{K}}-d_{4\mathrm{K}}}{d_{300\mathrm{K}}}$	$\Delta = d_{300\mathrm{K}} - d_{4\mathrm{K}}$
Cu (base + bridge)	0.9 + 3 = 3.9	0.326	12.71
Brass screw	2	0.384	7.68
Alumina	1	0.064	0.64
Sapphire (or fused silica)	0.3	0.061 (-0.008)	0.183 (-0.024)
Si chip	0.5	0.022	0.11
In foil	0.1	0.64	0.64

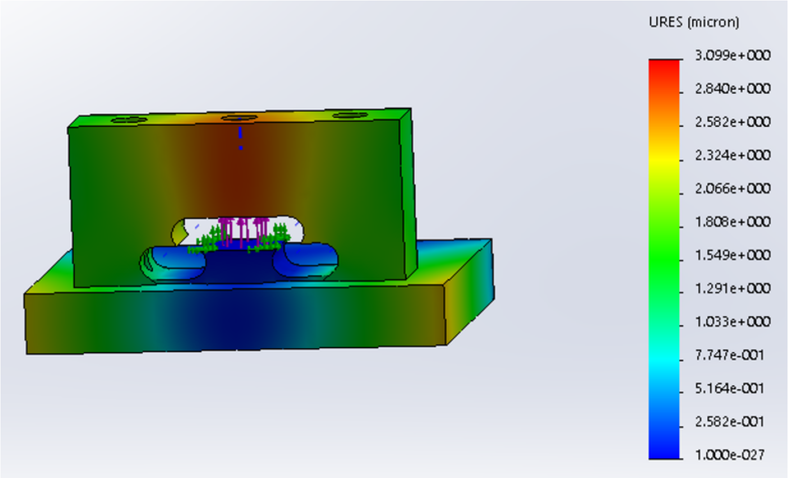

Figure 5.8: SolidWorks simulation showing the cryopackage deformation caused by a 200 N upward force, indicated with purple arrows. It can be noted that the largest deformation occurs at the top of the pressing bridge. © 2019 IEEE

bridge of about 3 µm. As a consequence, both experiments and simulation suggest that a pressure offset of about +3 MPa should be included in the measurements presented above.

5.3 Software for PJVS control

A *Python* package has been developed to properly drive a PJVS array by means of a set of AWGs and a nanovoltmeter. This software allows to independently observe the current-voltage characteristics of each PJVS segment, to check the arrays quantum operating margins and to synthesize stepwise approximated voltage waveforms. The program is modular and easily reconfigurable for different calibration and testing needs. The source code is publicly available under GNU-GPLv3 license on *GitHub* [268].

5.3.1 Why open-source?

Nowadays, proprietary software packages for driving PJVS devices are commercialized within ac quantum voltmeter systems [134, 135]. These are developed in LabView and are mainly addressed for use in calibration laboratories, where routine measurements are performed and, hence, a direct access to the source code is typically not necessary. This is not the case of researchers involved in primary metrology, who may prefer to develop their own software to keep total flexibility in the experimental setup and full control of the measurement procedure [244]. However, to avoid replications, increase reliability and speed-up debugging, a standardized code is greatly advantageous: for this reason, the development of open-source software has been recently addressed in electrical metrology, as witnessed in the activities planned in several EURAMET projects [269, 270].

Among the most outstanding result of the open-source philosophy, Python is an interpreted high-level programming language widely used for scientific applications [271]. It runs on interpreters that are available for all operating systems and provides access to a vast and complete scientific library.

5.3.2 System settings and electrical network analysis

In its current version, the program drives the 13-bit PJVS by controlling four 4-channels AWGs[1] [272] and a Keithley 2182A nanovoltmeter [259] (Fig. 5.9). Using different instruments can be simply accomplished by editing few functions in the code.

Before presenting the software from both user and developer perspectives, a detailed analysis of the employed electrical system is given, with reference to the circuit depicted in Fig. 5.10. This surely helps to understand how the PJVSs are actually operated and, consequently, the steps followed by the main functions to calculate the voltages that each AWG channel should supply to suitably current-drive the PJVS segments.

---

[1] Active Technologies AT-AWG 1104

Figure 5.9: Photograph of the instrumentation controlled by the software: on the right, five AT-AWG 1104 (four are used to drive a 13-bit PJVS), on the left, the Keithley 2182A nanovoltmeter for measuring the PJVS output voltage.

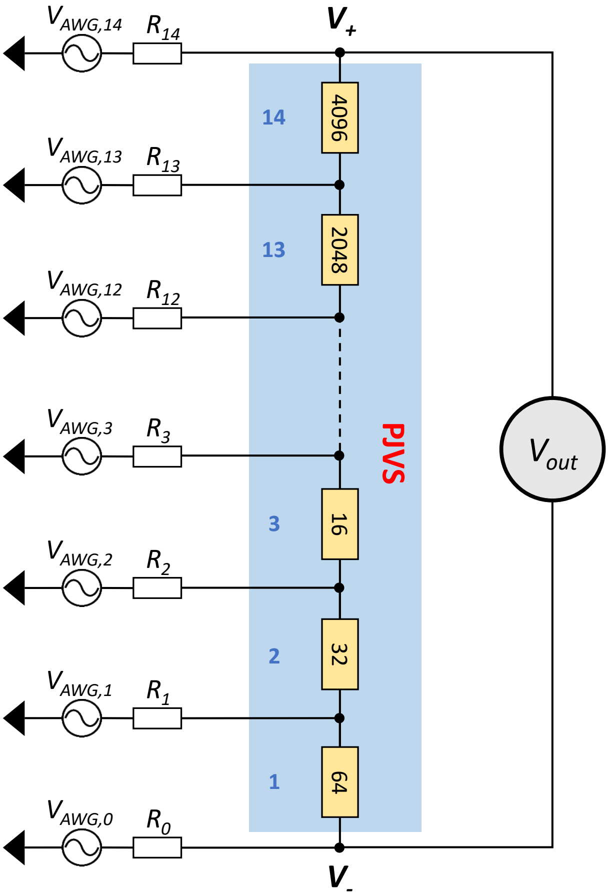

Figure 5.10: Electric circuit comprising the 13-bit PJVS and 15 AWG channels ($V_{AWG,i}$). The PJVS array is enclosed in the blue shaded area, with the number of junctions of each subsection specified in the rectangular boxes. R_i is the output resistance of the i^{th} AWG channel: its value can be selected among $50\,\Omega$, high impedance (open circuit) and low impedance (short circuit) to accomplish the desired operating mode.

Waveform synthesis and quantization test system settings

Referring to Fig. 5.10, the AWGs output resistances from R_1 to R_{14} are set to $50\,\Omega$, whereas R_0 is set to $0\,\Omega$. Voltages from $V_{AWG,1}$ to $V_{AWG,14}$ are evaluated via Kirchhoff analysis according to the current that is wanted to flow in each sub-array. Differently, V_0 is always zero. The current value that bias the i^{th} sub-array to the center of the n quantum step is indicated as $I_{i,n}$, whereas the sub-array voltage drop is provided by Josephson equation $V_{i,n} = N_s(i)\, n\, K_J^{-1}\, f_{rf}$. Consequently, voltages

$V_{AWG,i}$ are calculated as

$$\begin{aligned}
V_{AWG,1} &= V_{1,n} + R_1\,(I_{1,n} - I_{2,n}) \\
V_{AWG,2} &= V_{1,n} + V_{2,n} + R_2\,(I_{2,n} - I_{3,n}) \\
V_{AWG,3} &= V_{1,n} + V_{2,n} + V_{3,n} + R_3\,(I_{3,n} - I_{4,n}) \\
&\ldots\ldots \\
V_{AWG,14} &= V_{1,n} + V_{2,n} + V_{3,n} + \ldots. + V_{13,n} + V_{14,n} + R_{14}\,I_{14,n}
\end{aligned} \tag{5.3}$$

where currents $I_{J,i,n}$ flowing clockwise are taken as positive.

Quantization test is a very particular case of waveform synthesis, where a constant zero output is obtained by driving all the sub-arrays on a non-zero voltage step. This is achieved by setting $n = +1(-1)$ for $i = 1$ to 13 and $n = -1(+1)$ for $i = 14$.

Current-voltage characteristics system settings

The software allows to visualize the current-voltage characteristics of one or more consecutive segments. To do this, output resistance and voltage of each AWG channel have to be properly set. To get a dc current flowing into consecutive sub-arrays from j to k, with $1 \leq j \leq 14$ and $j \leq k \leq 14$, output resistances and voltages are set as follow:

$$\begin{aligned}
&R_{j-1} = 0\,\Omega \\
&R_k = 50\,\Omega, \\
&R_i = \infty, \text{ for } i \neq j-1 \text{ and } i \neq k \\
&V_{AWG,i} = 0\,\mathrm{V}, \text{ for } i \neq k
\end{aligned} \tag{5.4}$$

Accordingly, the current $I_{j\div k}$ that flows into the selected segments is

$$I_{j\div k} = \frac{V_{out} - V_{AWG,k}}{R_k} \tag{5.5}$$

Finally, $V_{AWG,k}$ is varied and the $I_{j\div k}$ versus V_{out} curve is obtained. It must be stressed that, actually, only two channels at time are used, in that the others are set to high-impedance.

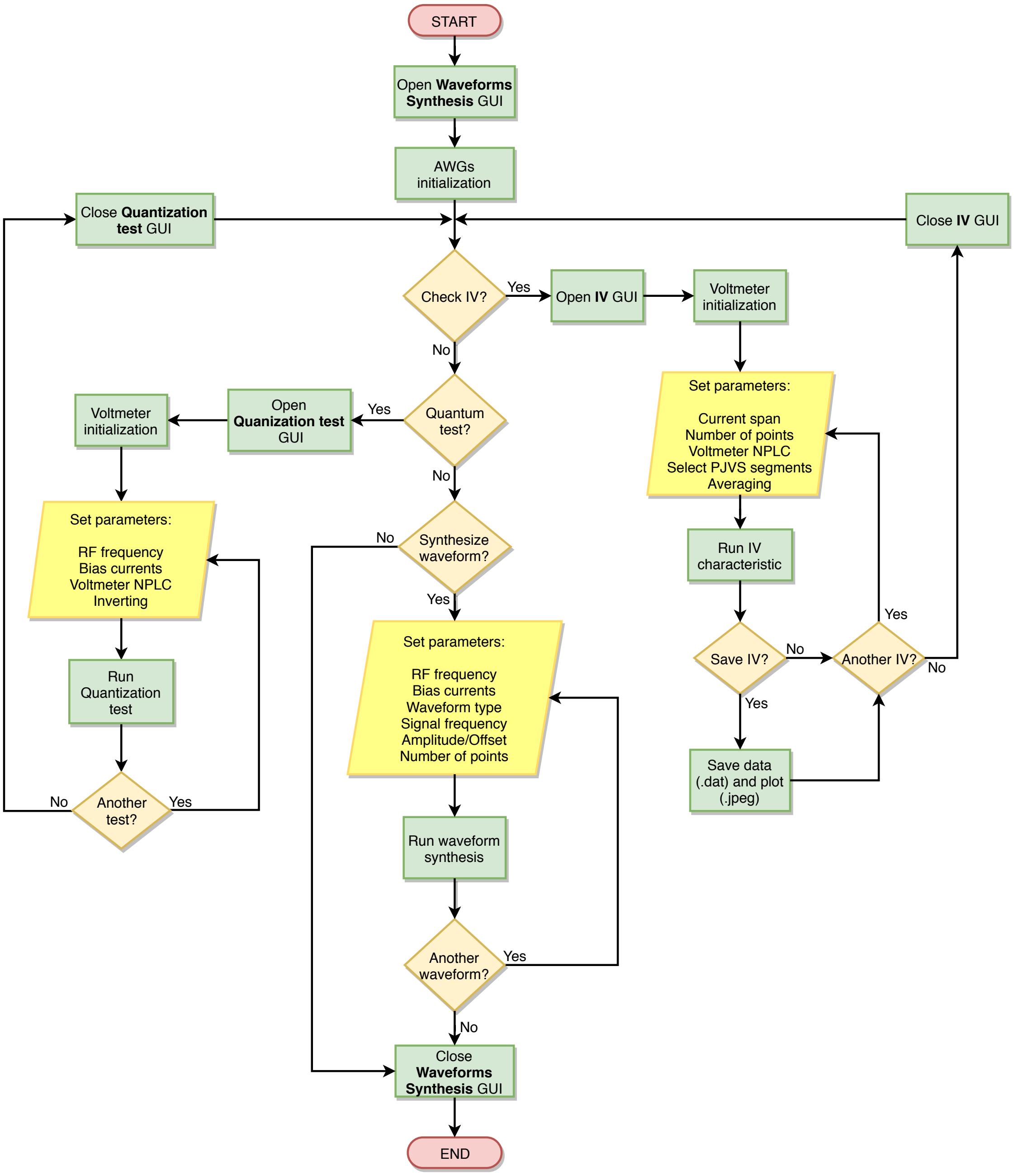

Figure 5.11: Flow chart of the Python software for the control of a PJVS device.

5.3.3 Software description

User's point of view: the Graphic User Interface

The program execution is outlined in the flow chart in Fig. 5.11, which summarizes input parameters and tasks of the three main forms making the Graphic User Interface (GUI). These are:

- *PJVS Waveform Synthesis*
- *PJVS IV-characteristics*
- *PJVS Quantization Test*

The *PJVS Waveform Synthesis* form (Fig. 5.12) is the first that is shown up to the user and enables to correctly initialize the four AWGs. Its description is moved to the end of this section, since current-voltage curves and steps quantization are usually checked first.

The *PJVS IV-characteristics* form is shown in Fig. 5.13. It initializes the nanovoltmeter and sets the main parameters of the current-voltage characteristics to observe, namely current span, number of points, and the number of power line cycles (NPLC) of the nanovoltmeter, related to both speed and accuracy of voltage data acquisition. Moreover, it allows to separately check the current-voltage curves of individual or grouped segments and to average them to reduce noise effects. Finally, current-voltage curves are displayed in real-time and can be saved as image and raw data.

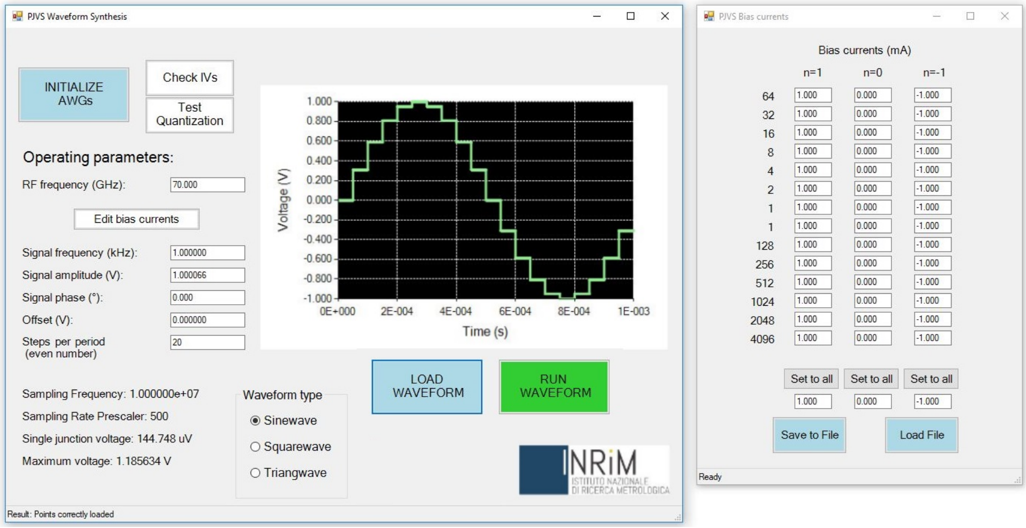

Operating parameters:

RF frequency (GHz): 70.000

Signal frequency (kHz): 1.000000

Signal amplitude (V): 1.000066

Signal phase (°): 0.000

Offset (V): 0.000000

Steps per period (even number): 20

Sampling Frequency: 1.000000e+07

Sampling Rate Prescaler: 500

Single junction voltage: 144.748 uV

Maximum voltage: 1.185634 V

Waveform type

● Sinewave

○ Squarewave

○ Triangwave

Result: Points correctly loaded

Bias currents (mA)

	n=1	n=0	n=-1
64	1.000	0.000	-1.000
32	1.000	0.000	-1.000
16	1.000	0.000	-1.000
8	1.000	0.000	-1.000
4	1.000	0.000	-1.000
2	1.000	0.000	-1.000
1	1.000	0.000	-1.000
1	1.000	0.000	-1.000
128	1.000	0.000	-1.000
256	1.000	0.000	-1.000
512	1.000	0.000	-1.000
1024	1.000	0.000	-1.000
2048	1.000	0.000	-1.000
4096	1.000	0.000	-1.000
	1.000	0.000	-1.000

Ready

Figure 5.12: *PJVS Waveform Synthesis* GUI. The expected output waveform is displayed in the graph. The supplementary form to set, save and load the bias currents matrix is shown on the right.

As anticipated, when quantization test is performed, the PJVS array is split into two equal branches counting 4096 junctions each, which are then current-biased on opposite voltage steps. Therefore, the output voltage across the whole PJVS is expected to be null over a certain currents range, depending on steps width, and can be determined by varying the bias current flowing into each segment. The values of measured voltage and running standard deviation are displayed by means of two dedicated real-time graphs and textboxes.

After this first checking part, the user can return to the *PJVS Waveform Synthesis* form to set input parameters and properties of the waveforms to synthesize. Input parameters are microwave frequency and bias currents matrix. A dedicated form, shown on the right side of Fig. 5.12, enables the user to edit, save and load the bias currents values $I_{i,n}$, three per each segment i, one per quantum step ($n = -1, 0, 1$). Generally, $I_{i,0} = 0$ and $I_{i,-1} = -I_{i,1}$. The most important output parameters are frequency, amplitude, offset, phase and number of steps of the staircase voltage waveform. As soon as the calculated voltages $V_{AWG,i}$ are loaded on each AWG channel, the expected waveform is visualized in the graph and ready to be synthesized.

Developer's point of view

The software consists of four primary functional blocks, which are shortly described as follows.

The *Math_Functions.py* module defines the functions that calculate the AWGs output voltages for waveform synthesis and quantization test. These are:

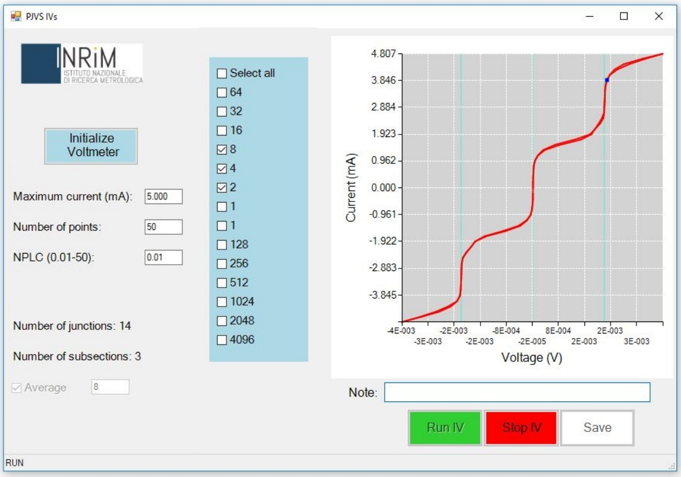
Maximum current (mA): 5.000
Number of points: 50
NPLC (0.01-50): 0.01
Number of junctions: 14
Number of subsections: 3
☑ Average 8
☐ Select all
☐ 64
☐ 32
☐ 16
☑ 8
☑ 4
☑ 2
☐ 1
☐ 1
☐ 128
☐ 256
☐ 512
☐ 1024
☐ 2048
☐ 4096
Note:
RUN

Figure 5.13: *PJVS IV-characteristics* GUI. The averaged current-voltage characteristic of 14 junctions is displayed in the graph.

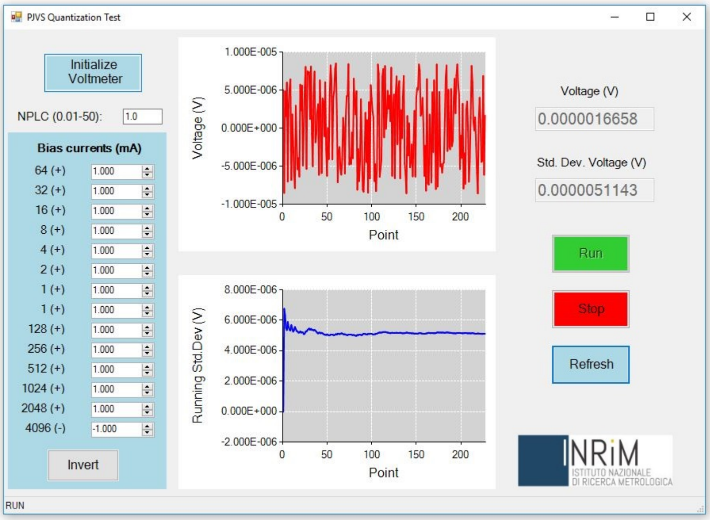

NPLC (0.01-50): 1.0

Bias currents (mA)

64 (+)	1.000
32 (+)	1.000
16 (+)	1.000
8 (+)	1.000
4 (+)	1.000
2 (+)	1.000
1 (+)	1.000
1 (+)	1.000
128 (+)	1.000
256 (+)	1.000
512 (+)	1.000
1024 (+)	1.000
2048 (+)	1.000
4096 (-)	-1.000

Voltage (V): 0.0000016658

Std. Dev. Voltage (V): 0.0000051143

RUN

Figure 5.14: *PJVS Quantization Test* GUI. Measured voltage and running standard deviation are displayed in the two graphs.

- *EvalParameters*: calculates PJVS maximum output voltage and resolution via Josephson equation;
- *CalcQuantumVolt*: converts a generic voltage into the binary representation of the closest quantized voltage obtainable with PJVS. Then it calculates the required AWG voltages with Eqs. 5.3;
- *CalcSine*, *CalcSquare* and *CalcTriang*: respectively discretize ideal sine, square and triangular waves into a number of user-defined evenly time-spaced points, which are then quantized via the *CalcQuantumVolt* function;
- *QuantumTest*: calculates the AWG voltages to bias the two equal halves of the PJVS array on opposite quantum steps, again via Eqs. 5.3.

The *Devices_Control.py* module is responsible of the communication between the computer and the instrumentation. It imports the interfacing libraries (GPIB-PyVISA [273] and AWG's *dll*) and implements all remote-controlled operations of AWGs and voltmeter. Its main functions are:

- *InitAWGs*: initializes the AWGs;
- *InitVoltmeter*: initializes the nanovoltmeter and sets the user-defined NPLC parameter;
- *Load*: loads the calculated $V_{AWG,i}$ points for the waveform synthesis and the required output resistances R_i;
- *Run* and *Stop*: activate and deactivate the AWGs output.

The *Graphics.py* module is based on *Microsoft Developer Network (MSDN) .NET* framework, implements the GUI, and defines its elements' properties and functionalities. It imports *Devices_Control.py* for linking any graphic interactive element (button, textbox, checkbox, etc.) to a device function (initialization, loading, etc.). It imports *Math_Functions.py* for passing user input parameters as arguments of the mathematical functions and performs and displays current-voltage characteristics exploiting Eqs. 5.4 and 5.5.

Finally, the *Main.py* module defines fundamental parameters used throughout the whole program, e.g. array structure (N_s) and maximum AWG output voltage, and starts program execution by opening the *PJVS Waveform Synthesis* form.

5.3.4 Further considerations and future improvements

Owing to its modular structure, the program can be easily customized and integrated with new features by modifying few functional blocks. Furthermore, by simply updating the main functions in *Devices_Control.py*, a different equipment can be employed. Indeed, any instrument can be potentially interfaced through the *PyVisa* GPIB library, via USB with the *PyUSB* library, or by directly using the *dll* libraries with *Python for .NET* [274].

The software is still under refinement. Specifically, the integration of a fast sampling voltmeter is scheduled, which will allow a direct and real-time processing of the output waveforms, fundamental for fully exploiting the peculiar characteristics of PJVSs for ac voltage calibrations [127]. A temperature controller will also be included, particularly useful when the PJVS chip is operated in a cryocooler [257, 275].

5.4 Operation of PJVS under microwave radiation

The custom cryopackage (Sec. 5.2) and the software for the correct polarization of the array segments (Sec. 5.3) have been employed to conduct experimental tests on the PJVS devices in use.

5.4.1 Cryogenic setup

A two-stage PT refrigerator (Cryomech PT-410, 1 W cooling power at 4.2 K [276]) has been employed for cooling the cryopackage with the PJVS device. As with the GM refrigerator, the useful cooling surface is enlarged with an OFHC coldplate installed onto the cold finger. The cryopackage is then tightened to the coldplate, as shown in Fig. 5.15, with a thin layer of Apiezon N applied at the

Figure 5.15: PJVS cryopackage installed on the PT cryocooler coldplate. The Si diode temperature sensor and the WR-12 waveguide for the rf transmission are shown as well.

interface. A Si diode thermometer, installed on the Cu pressing bridge, and a manganin resistive heater, wound around the coldplate, allow to set and monitor the operating temperature. The excitation rf-field was supplied by a mechanically-tuned Gunn oscillator with central frequency $f_{rf} = 72\,\mathrm{GHz}$ [277] and transmitted to the chip antenna through a WR-12 stainless-steel waveguide. The low thermal conductivity of stainless steel limits the heat loading of the cryocooler due to the direct connection with the room temperature environment. Nevertheless, to reduce the detrimental rf signal attenuation of stainless-steel, the waveguide is internally gold-plated.

5.4.2 Results

According to the theory of overdamped junctions, optimal Shapiro steps of order n are obtained with minimum rf power demand when the condition $f_c = K_J\, V_c \simeq n\, f_{rf}$ is met [278], being f_{rf} the frequency of the employed rf oscillator. Therefore, to optimize $n = 1$ voltage steps with $f_{rf} \simeq 72\,\mathrm{GHz}$, the operating temperature should be adjusted to get $V_c \sim 150\,\mu\mathrm{V}$. Owing to the rather high characteristic voltage of the employed PJVS device ($V_c \sim 350\,\mu\mathrm{V}$ at $4.2\,\mathrm{K}$), the cryocooler temperature was raised up to about 6 K to approach the target value. Current-voltage curves with $\sim 1\,\mathrm{mA}$ wide voltage steps were then observed by applying an rf power of about 40 mW (Fig. 5.16a).

Physical conditions to improve the operation with $n = +2$ steps are instead attained around 4.5 K, where V_c is approximately doubled with respect to the $n = 1$ case: experimentally-observed second quantum steps of some PJVS segments are shown in Fig. 5.16b, with current amplitudes comparable to that discussed in the

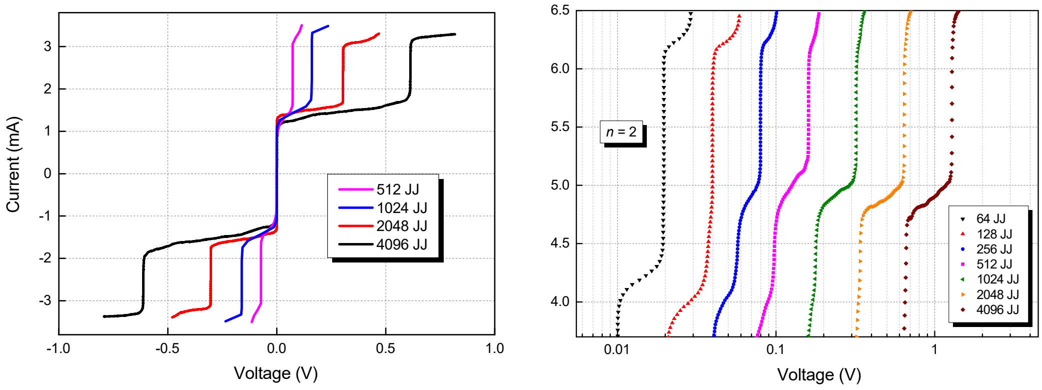

(a) (b)

Figure 5.16: (a) Current-voltage characteristics of the most significant PJVS segments irradiated at 72 GHz at 6 K in cryocooler. (b) Positive second order steps of the most significant PJVS segments irradiated at 72 GHz at 4.5 K in cryocooler.

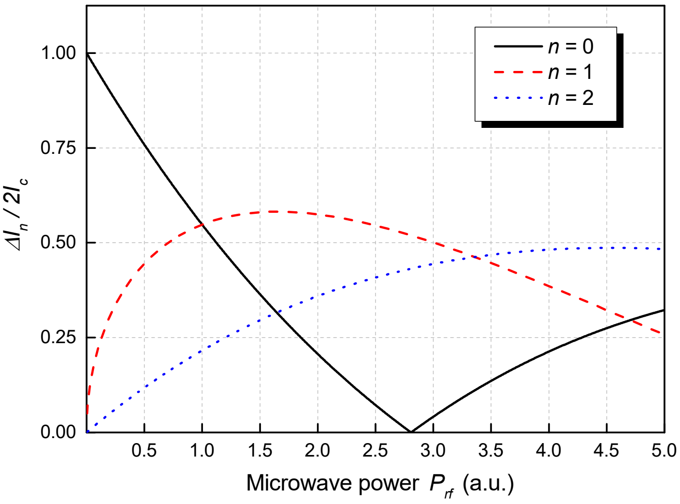

Figure 5.17: Normalized step current width ΔI_n for $n = 0, 1$ and 2 versus rf power per junction P_{rf} (in arbitrary units), calculated via Eq. 5.6 and knowing that $P_{rf} \propto {V_{rf}}^2$. P_{rf} values are normalized to the optimal value that gives equally wide $n = 0$ and 1 steps.

previous case, though with more demanding rf power requirements. In fact, as mentioned in Ch. 1, the relation between n step current width ΔI_n and microwave power can be theoretically derived, leading to

$$\Delta I_n = 2I_c \left| J_n \left(\frac{K_J \, V_{rf}}{f_{rf}} \right) \right| \tag{5.6}$$

with J_n the n order Bessel functions of first kind and V_{rf} the rf voltage amplitude.[45]. According to Eq. 5.6, the normalized step amplitudes for $n = 0, 1$ and 2 are plotted in Fig. 5.17 as a function of the power per junction P_{rf}. For a given I_c, a 50 % increase of the optimal power for equal 0 and 1 steps ($P_{rf} = 1$) is required to get an acceptable amplitude for $n = 2$ step.

First and second quantum steps have been then exploited to synthesize stepwise sine waves with maximum amplitude around 2 V and frequencies up to 1 kHz. Fig. 5.18 shows two 100 Hz sinusoidal waveforms with 20 samples: the black curve uses $n = 1$ steps, hence with $V_{LSB} = 158\,\mu\text{V}$, whereas both peak and resolution V_{LSB} are doubled by exploiting second quantum steps (red curve).

The metrological application of these cryogen-free PJVS voltage waveforms is currently prevented by some specific issues. Among these, cryocooler thermal oscillations, ranging from 200 mK at 4 K to 600 mK at 6 K, and the non-optimal shielding from interfering magnetic fields, causing magnetic fluxons to be trapped inside the junctions, are the most challenging. As illustrated in Ch. 4, interventions aimed at reducing these effects are planned.

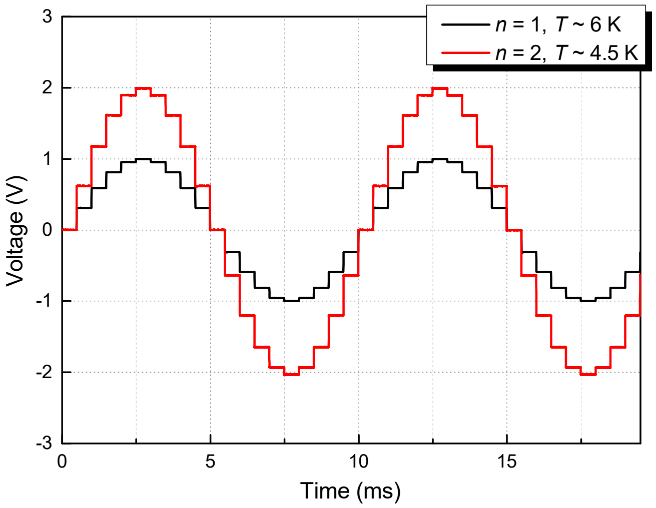

Figure 5.18: 100 Hz stepwise sine waves synthesized with the PJVS device in cryocooler, the black curve (1 V) with first order steps at 6 K, the red curve (2 V) with second order steps at 4.5 K.

5.5 Testing unconventional bias modes

In this section, unconventional methods to bias a PJVS array are presented. These are based on the simultaneous use of first and second quantum steps and allow to decrease the number of junctions and bias lines per volt. Before deepen into the description of these newly-devised polarization techniques, it may be useful to introduce the already existing, but less popular, ternary-divided PJVS arrays [98].

5.5.1 Ternary PJVS

As known, binary PJVSs use steps with order $n = -1, 0$ and $+1$ to generate positive and negative quantized voltages. However, these arrays do not fully exploit the three available quantum steps: in fact, a given output voltage V_{out} can be generated with different combinations. To avoid such redundant behavior, PJVSs with sub-arrays organized in a ternary fashion (1, 3, 9, 27, ...) can be adopted. Such ternary DACs are said to be balanced, in that the three employed voltage levels (-1, 0 +1) are symmetric with respect to zero.

Compared to binary PJVS, the ternary encoding allows to distribute the number of junctions required to reach a given voltage V_{out} in a lower number of sub-arrays and with no losses in terms of resolution. Fewer segments also means fewer bias sources and fewer leads or cables from the room temperature environment to the cryogenic stage. Tab. 5.3 provides a comparison between binary and balanced

Table 5.3: Comparison between binary and balanced ternary PJVSs capable of generating at least 1 V at 70 GHz with $n = -1, 0$ and $+1$.

	Binary	**Balanced ternary**
Number of junctions	8191	9841
Number of segments	13	9
Employed quantum steps	0, ±1	0, ±1
Full-scale voltage V_{FS} ($f_{rf} = 70\,\mathrm{GHz}$)	1.186 V	1.424 V

ternary PJVSs exploiting $n = -1, 0$ and $+1$ steps, considering arrays capable of generating at least 1 V under a typical microwave radiation of 70 GHz: the 1 V balanced ternary array only needs nine independent segments, four fewer than the binary one, at the expenses of a small increase of the total number of junctions.

5.5.2 Exploiting both first and second quantum steps

By exploiting also $n = \pm 2$ voltage steps, a further reduction of the sub-arrays number can be accomplished, along with a lower number of junctions per volt. In the following, novel methods taking advantage of the simultaneous use of zero, first and second Shapiro steps are presented.

Doubling PJVS output voltage

A first straightforward improvement that directly follows from the availability of second quantum steps is the increase of the full-scale voltage. However, as discussed in Sec. 5.4.2, this implies also the doubling of V_{LSB}. Here, a new approach is proposed, which offers the possibility of doubling V_{FS} by maintaining the resolution of the conventional $n = 1$ case. This interesting property can be accomplished with the simultaneous use of zero, first and second order Shapiro steps and, consequently, by properly upgrading the bias voltage calculation algorithm described in Sec. 5.3.2 to consider the availability of the $n = \pm 2$ levels.

This method is formally equivalent to physically add one large sub-array, i.e. a more significant bit, to the original PJVS sequence. For instance, a segment with 8192 junctions would be included at the end of the 13-bit PJVS used in this work. This can be avoided by exploiting second quantum steps, which make this further bit as *virtual*, in the sense that no additional junctions, segments and dedicated bias channels are needed. Tab. 5.4 shows a comparison between these two kinds of (13+1)-bit PJVSs: either with physical or virtual most-significant-bit (MSB).

Table 5.4: Comparison between 14-bit PJVSs with physical and virtual MSB.

	Physical MSB	**Virtual MSB**
Number of junctions	16 383	8191
Number of segments	14	13
Employed quantum steps	0, ±1	0, ±1, ±2
Full-scale voltage V_{FS} ($f_{rf} = 70\,\text{GHz}$)	2.371 V	2.371 V

Non-binary PJVS

Another way to take advantage of the five accessible voltage levels ($n = 0, \pm1, \pm2$) is to implement alternative codifications with base up to five, with the aim of further reducing the number of junctions and segments per volt. Excluding the already discussed binary and balanced ternary encodings, which use only zero and first quantum steps, the possible codifications are:

- unbalanced ternary;
- unbalanced quaternary;
- balanced quinary.

Unbalanced ternary is different from the aforementioned balanced version, since the voltage levels employed in the codification (0, 1 and 2) are not symmetrical with respect to zero. However, as shown in Tab. 5.5, this configuration is not particularly convenient, in that, besides its redundancy, the same number of junctions and sub-arrays of the balanced ternary are needed to reach the 1 V threshold. Though still redundant, quaternary-divided arrays with unbalanced encoding would allow to considerably decrease both the number of sub-arrays (from 13 to 7) and of junctions (by 33 %), compared to conventional binary arrays. Nevertheless, a reduction of number of junctions and bias lines higher than 50 % would be attained with balanced quinary PJVS. It is important to note that reducing number of junctions would be also advantageous in terms of microwave technology, because a lower number of on-chip power-splitters and parallel microstriplines would be necessary. Yet, to address this, a partial redesign of the PJVS device should be undertaken.

5.5.3 Experimental conditions to optimize both first and second steps

As previously discussed, the operating temperature has to be suitably set to enhance the operation of n order quantum steps. Therefore, to get wide first

Table 5.5: Comparison between unbalanced ternary, unbalanced quaternary, and balanced quinary PJVSs capable of generating at least 1 V at 70 GHz with Shapiro steps up to the second order.

	Unbal. ternary	**Unbal. quaternary**	**Bal. quinary**
Number of junctions	9841	5461	3906
Number of segments	9	7	6
Employed quantum steps	$0, \pm 1, \pm 2$	$0, \pm 1, \pm 2$	$0, \pm 1, \pm 2$
Full-scale voltage V_{FS} ($f_{rf} = 70\,\mathrm{GHz}$)	2.849 V	1.581 V	1.131 V

and second steps at the same time, the temperature should be chosen to give V_c comprised between 145 µV and 290 µV at 70 GHz. Generally, Josephson arrays are designed to exhibit $V_c \sim 150\,\mu\mathrm{V}$ at 4.2 K, so as to optimize their response when cooled by LHe; in such case, decreasing the operating temperature to rise V_c is quite complicated. Differently, cooling Josephson devices below the LHe boiling point with a cryocooler is simpler, though limitations related to the reduced cooling power and the lower thermal conductance at such temperatures may arise. A more straightforward solution is to employ Josephson junctions exhibiting a higher V_c.

Concerning microwave power, the theoretical behavior depicted in Fig. 5.17 suggests that a 50 % power per junction increment with respect to the $n = 0$ and 1 optimal condition ($P_{rf} = 1$) is required to get large $n = 2$ steps too. Nevertheless, as shown in Tab. 5.5, the availability of the second steps leads to the halving of the number of junctions per volt and, in principle, the additional rf power should be totally compensated by the reduced number of junctions. In addition, according to the theoretical model, the simultaneous optimization of three steps causes a more than 40 % decrease of the quantum operating margins, given by the smallest step width ($\Delta I_0 = \Delta I_2 < \Delta I_1$), compared to the optimized $n = 0$ and 1 case. Yet, this should not be detrimental for the use of three quantum steps in a novel PJVS implementation, in that operating margins better than 1 mA with $n = 0$ and 1 have been demonstrated [140, 99]. Then, even a 50 % margins reduction would still guarantee adequate second steps [143].

To conclude, it should be stressed that this discussion is based on an ideal description of the Josephson junctions that, though helpful in giving a basic idea of the actual situation, needs be further investigated by experiments.

5.5.4 Experimental tests

The software described in Sec. 5.3 has been properly adapted to implement the unconventional codifications described in Sec. 5.5.2 and to instruct the AT-1104 AWGs accordingly. The cryocooler temperature was set to approximately 5 K, where $V_c \simeq 225\,\mu\mathrm{V}$, i.e. the midpoint between $K_J^{-1} f_{rf}$ and $2\,K_J^{-1} f_{rf}$ with $f_{rf} = 72\,\mathrm{GHz}$. In this condition, current-voltage curves displayed in Fig. 5.19 have been observed, with an rf power of about 55 mW, a value 40 % higher than that required to get optimal zero and first steps at 6 K and in line with the theoretical model.

Although simultaneously wide quantum steps were not achieved for all PJVS segments, these were exploited to conduct the waveform synthesis tests described below. Further experiments will be carried out in LHe, so as to exclude the noisy effects currently affecting the employed cryocooler system, and with a newer PJVS array with a suitable characteristic voltage at 4.2 K.

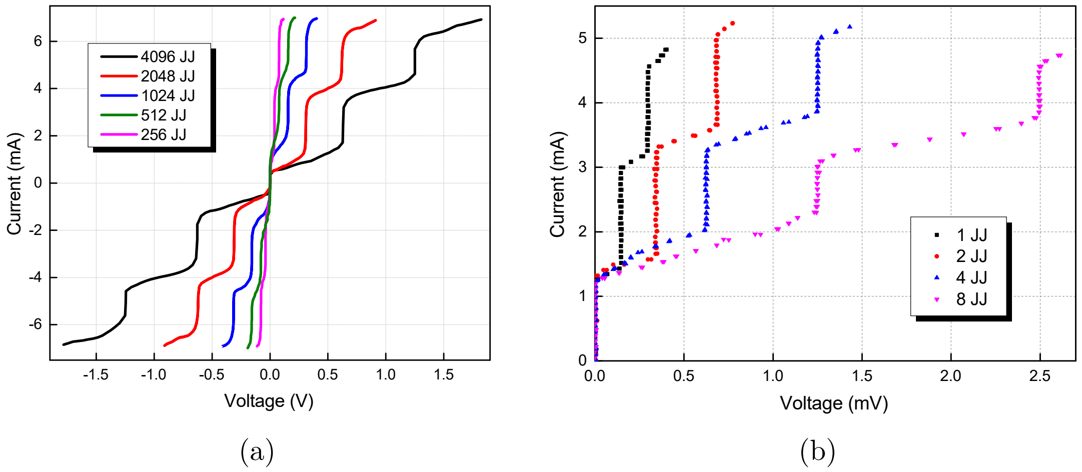

Figure 5.19: Current-voltage characteristics of most (a) and least (b) significant PJVS sub-arrays under 72 GHz radiation at $T \simeq 5\,\mathrm{K}$ in cryocooler.

5.5.5 Synthesis of stepwise sine waves

Tests on waveform synthesis employing the newly devised bias techniques were carried out with the same experimental setup presented in Sec. 5.4.1. Results are presented in the following for two cases.

Sine waves with virtual (13+1)-bit PJVS

Stepwise sinusoidal waveforms have been synthesized adopting the bias technique presented in Sec. 5.5.2. Each voltage step of the approximated sine wave is converted into a vector of digits 0, ±1 and ±2, which defines the quantum step that each sub-array should be driven to. As in the traditional PJVS, there are redundant ways to obtain a generic voltage V_{out}. In the following the simplest one is reported, considering $V_{out} \geq 0$. Negative voltages are simply obtained by reversing each digit.

- For $0 \leq V_{out} \leq V_{FS}/2$, the same bias method employed for conventional PJVSs is adopted. A m-size vector of 0 and 1 encodes V_{out}, where m is the number of physical bits ($m = 13$ in this case). Hence, no sub-array is biased on the second step.

- For $V_{FS}/2 < V_{out} \leq V_{FS}$, all sub-arrays are biased at least on $n = 1$, with some biased on $n = 2$. This is evaluated by converting $V'_{out} = V_{out} - V_{FS}/2$ into a binary m-long pattern of 0 and 1 and, then, raising up each bit by one, thus obtaining a vector of only 1 and 2. At full-scale ($V_{out} = V_{FS}$ and $V'_{out} = V_{FS}/2$), all segments are biased on the second step.

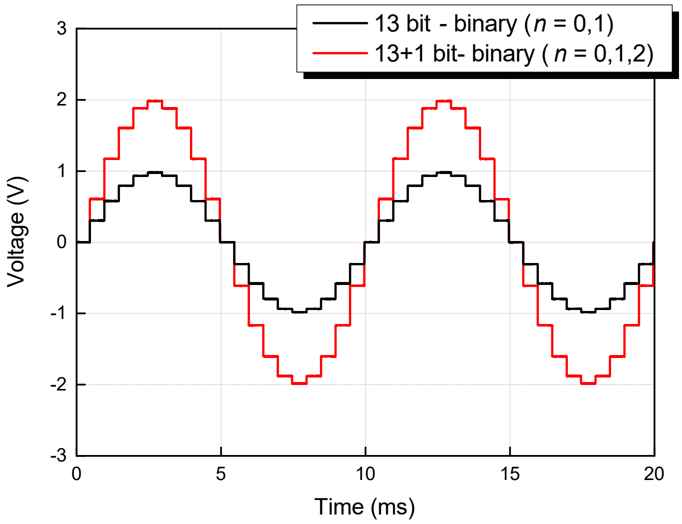

Figure 5.20: Stepwise sine waves synthesized with the PJVS array at $T \sim 5.2\,\mathrm{K}$. The 1 V sine wave (black) has been obtained with the conventional 13-bit binary technique. The 2 V sine wave (red) has been obtained with the *virtual* (13+1)-bit binary technique.

Sine waves with frequencies between 10 Hz and 1 kHz and amplitudes up to 2.6 V have been synthesized. The approximated sine wave in black shown in Fig. 5.20 has been generated via the conventional binary technique, thus exploiting only $n = 0$ and ± 1 steps, in that its peak-amplitude is below $V_{FS}/2$. In the 2 V sine wave (red curve), second order steps were exploited as well, taking advantage of the additional *virtual* bit to increase the peak voltage.

Sine waves with quaternary PJVS

Since PJVSs with codification base greater than three are not available up to now, the 13-bit binary PJVS in use has been treated as quaternary, namely by considering only the segments with a number of junctions equal to a power of four ($2^0 = 4^0$, $2^2 = 4^1$, $2^4 = 4^2$,...). This feature has been attained in two ways:

1. *Fake* quaternary: all segments are electrically connected, hence 13 output voltage channels (i.e. four AT-1104 modules) are actually employed (see Fig. 5.21a). No current flows into the sub-arrays 2, 8, 32, ..., i.e. with 2^i junctions and i odd number, and AWGs voltage outputs are calculated accordingly. A generic quantum voltage V_{out} is then encoded into a quaternary digit-word $(q_7, 0, q_6, 0, q_5, 0, ..., q_1, 0, q_0)$, with $q_i = 0, \pm 1, \pm 2$.

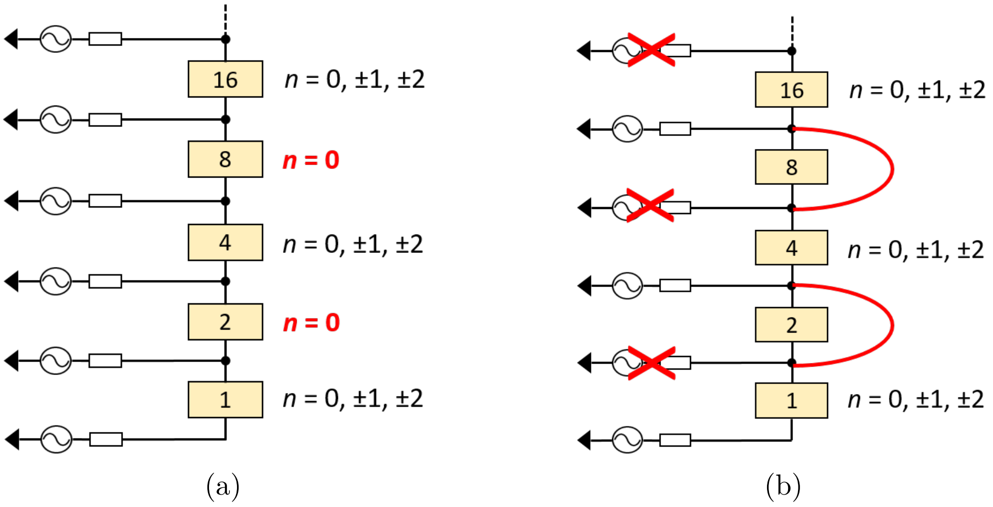

Figure 5.21: Circuit connections for realizing *fake* (a) and *real* (b) quaternary PJVSs.

2. *Real* quaternary: odd-exponent PJVS sub-arrays are physically bypassed with a low (or, better yet, zero) resistance short-circuit (see Fig. 5.21b). Any voltage V_{out} is encoded into a sequence $(q_7, q_6, q_5, ..., q_1, q_0)$, with $q_i = 0, \pm 1, \pm 2$. Hence, half AWG channels (only two AT-1104 modules) are actually employed with respect of the conventional bias mode.

The physical bypasses for the *real* quaternary mode have been realized with short aluminum wires, wedge-bonded on the pads of the chip and with an estimated electrical resistance of few mΩ at 4 K. Since bias currents are in the mA range, a *parasitic* voltage drop up to 10 µV may occur. Though not negligible for metrological purposes, this did not prevent us to perform this experimental proof of concept.

Digitizing a given voltage $V_{out} \geq 0$ in terms of a balanced quaternary vector with -1, 0, $+1$ and $+2$ digits is derived from its unbalanced base-four representation, where only positive digit levels (0, 1, 2 and 3) are used. Starting from the LSB, the voltage steps $n = 3$ are replaced by $n = -1$, then the adjacent more significant digit is increased by one, using ordinary rules of carryover additions. For example:

$$(...\,1\,2\,3)_{uq} \rightarrow (...\,1\,2^{(+1)}\ -1) \rightarrow (...\,1^{(+1)}\ -1\ -1) \rightarrow (...\,2\ -1\ -1)_{bq} \qquad (5.7)$$

where the apex terms are the carryovers. Again, negative voltages are obtained by reversing each digit. Applying these two quaternary bias modes, stepwise sine waves have been synthesized, as shown in Fig. 5.22.

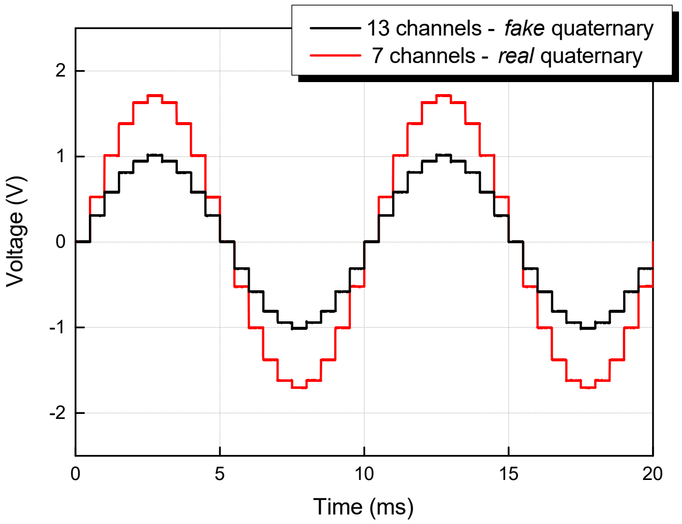

Figure 5.22: Stepwise sine waves synthesized with the PJVS array in cryocooler at $T \sim 5\,\mathrm{K}$. The $1\,\mathrm{V}$ sine wave (black curve) was obtained with the *fake* quaternary technique. The $1.728\,\mathrm{V}$ sine wave (red curve) was obtained with the *real* quaternary technique.

5.6 Conclusion

This chapter presents the activities carried out at INRiM with PJVS devices. A special cryopackage has been devised and tested in cryocooler at different temperatures and applied mechanical pressures between chip and holder. Using the PJVS array both as power source and temperature sensor, the thermal resistance of the package has been determined, resulting to successfully dissipate hundreds mW of power and, then, to guarantee the Josephson device correct operation in the high-vacuum environment of a mechanical refrigerator. An open-source software for driving conventional instrumentation to the correct bias of a PJVS is under development, and the main features of the current version are presented. Software and cryopackage have been then used to perform experimental tests on the SNIS programmable devices in use: it has been shown that suitably wide quantum voltage steps have been obtained in different conditions, enabling the synthesis of stepwise voltage waveforms at voltages higher than $2\,\mathrm{V}$ and frequencies of $1\,\mathrm{kHz}$ at most. Finally, the simultaneous use of both first and second quantum steps is proposed to significantly reduce the number of junctions and of bias lines required. New bias algorithm are shown and experimentally tested, proving that further technological efforts and investigation are needed.

Chapter 6

Investigation on pulse-driven Josephson standards at INRiM

INRiM is being actively involved in both ongoing and concluded EURAMET projects [279, 269], whose activities include research and development on pulse-driven Josephson voltage standards, also known as Josephson arbitrary waveform synthesizers (JAWSs). In this scope, a cryocooled system for JAWS arrays has been set up and is still under further improvement. In this chapter, the implementation of such system is described in detail. This comprises first the realization of a proper cryopackage for the He-free cooling of the JAWS chip, followed by a proper thermalization of the coaxial cable required for the rf pulsed signal transmission. Subsequently, dc and ac electrical characterizations of the array were carried out both in cryocooler and LHe, as a way of checking the effectiveness of the cryogen-free setup. Finally, waveform synthesis tests have been performed, along with an analysis of the systematic errors due to the cable employed to transfer the synthesized voltage waveform to the room-temperature environment.

Parts of this chapter are taken from the manuscripts in Refs. [280, 281, 282].

6.1 Experimental setup

JAWS chips employed at INRiM have been fabricated at PTB: these generally come with the carrier shown in Fig. 6.1, which comprises a Rogers RO30061 PCB mounted on a bakelite support. The chip circuit consists of two arrays, each with 4000 $\mathrm{Nb_xSi_{1\text{-}x}}$ junctions, integrated on a $10\,\mathrm{mm}\times10\,\mathrm{mm}$ Si substrate. For each array, junctions are arranged in two vertical stacks and embedded into the central conductor of a $50\,\Omega$ CPW [284]. To transmit the high frequency pulsed signal to each array, the PCB hosts two conducting CPW paths made of copper, covered with a $2\,\mu\mathrm{m}$ gold layer and terminated at the edge by PCB-SMA launchers [285]. Thin wedge-bonded aluminum wires are employed to connect the on-chip electrical

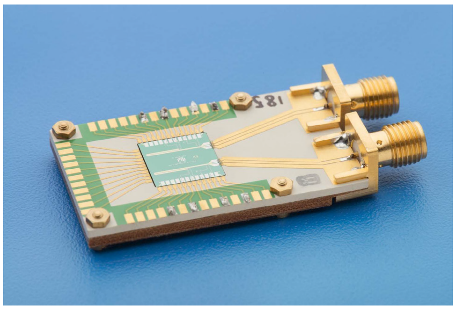

Figure 6.1: Photograph of a JAWS chip with two Josephson arrays, mounted on the bakelite holder for LHe operation [283]. ©2014 IEEE

lines (both low and high frequency) to those on the PCB.

JAWS devices have been characterized and tested both in LHe and in cryocooler. The cryocooler employed is the GM refrigerator presented in Ch. 4.

6.1.1 Cryopackage for JAWS chips

As with PJVSs, also the operating conditions of pulse-driven arrays may be affected by the local warming, if heat is not suitably dissipated. Nevertheless, owing to the lower maximum output voltage per chip and to the better coupling between coaxial cable and CPW, compared to rf waveguide-antenna coupling in PJVS, the design of a He-free cryopackage for JAWS devices presents less stringent constraints.

The original chip holder, shown in Fig. 6.1, was designed for LHe operation and, owing to the insulating bakelite support, is not suited for the use in cryocooler. Hence, a new carrier made of OFHC copper, similar to that for PJVS (Ch. 5), has been designed to replace the original one. In order to realize a good thermal contact, a special spring made of ergal (an aluminum alloy) has been realized for simultaneously pressing the chip against the carrier and transferring the heat from the junctions to the cryocooler. Yet, to avoid accidental electrical contacts, a 0.5 mm thick sapphire substrate is inserted between the chip and the ergal spring. In addition, a thin Cu strip tape is screwed to the Cu carrier and placed between spring and sapphire to further enhance heat transmission. A photograph of this custom cryopackage, positioned on the GM cryocooler coldplate, and its cross-sectional representation are shown in Fig. 6.4.

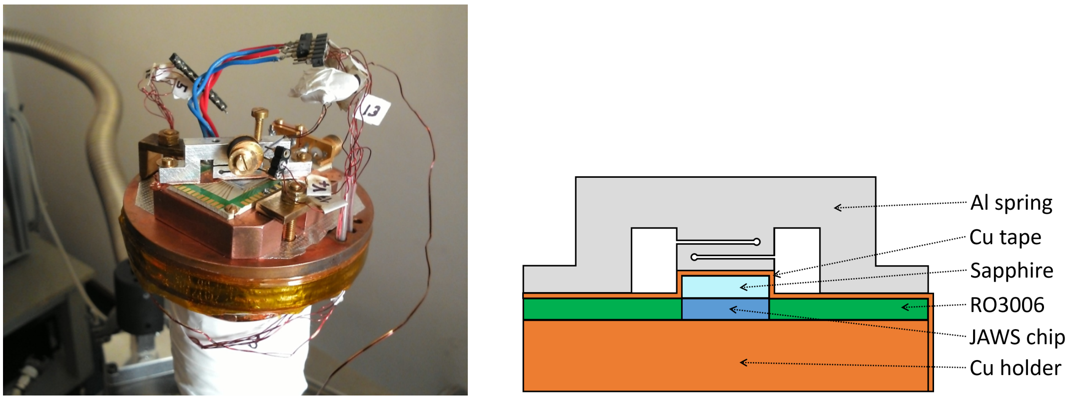

(a) (b)

Figure 6.2: (a) Photograph of the JAWS cryopackage installed on the GM cryocooler coldplate. (b) Cross-sectional schematic representation of the cryopackage (not in scale).

6.1.2 Reducing coaxial cable thermal loading

It should be considered that the coaxial cable employed for the broadband high frequency pulse transmission may significantly affect the lowest operating temperature, since it directly connects the cryocooler coldest stage to the laboratory environment. To reduce this thermal load, a 50 cm long coaxial cable with stainless-steel outer conductor and Cu inner conductor is adopted. As shown in Fig. 6.3a, along its path from the room-temperature vacuum flange to the JAWS holder, the cable is thermally anchored at two points via proper Cu links: first to the radiation shield of the cryocooler first stage at $\sim 40\,\mathrm{K}$ (Fig. 6.3b), then to the cold finger at $\sim 4\,\mathrm{K}$. In addition, an L-shaped Cu block (Fig. 6.4) directly connects the SMA-launcher to the Cu holder, thus allowing a significant heat fraction from the coaxial line to flow to the Cu holder, instead of being transmitted to the chip via the CPW. These interventions proved to reduce the thermal loading of the coldplate due to the coaxial cable, allowing to achieve minimum temperatures slightly above 4 K, sufficient for the operation of the JAWS chips in use.

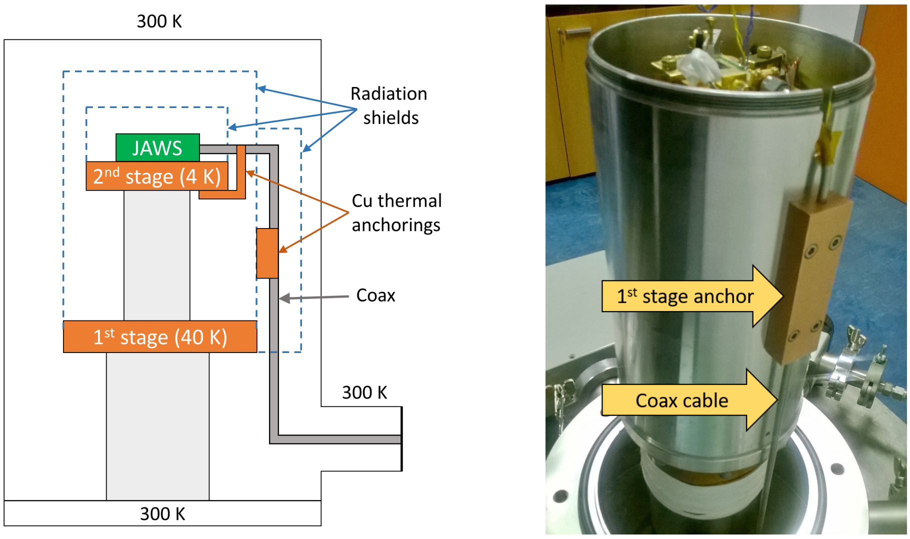

(a)

(b)

Figure 6.3: (a) Schematic representation of the cryocooler setup with the JAWS holder (green rectangle) positioned on the second stage and the coaxial cable for pulses transmission properly thermalized with Cu anchorings. (b) Cu anchoring to the radiation shield of the cryocooler first stage.

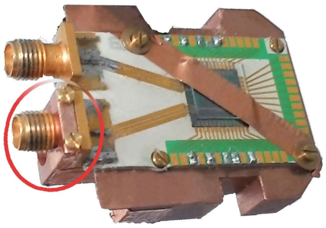

Figure 6.4: Photograph of the JAWS holder showing the L-shaped block (see description in the text) [280]. © 2017 Elsevier

6.2 JAWS electrical characterization

6.2.1 Dc characterization

First electrical measurements consisted in dc characterization of the JAWS device, both in LHe and cryocooler. A Keithley 6220 current source [236] and a Keithley 2182A nanovoltmeter [259] have been employed to observe the array current-voltage curves at different temperatures, as shown in Fig. 6.5. In LHe, setting the operating temperature above 4.2 K was accomplished by slightly raising the stick rod up, making the chip being cooled by He vapor. In cryocooler, the temperature was set via the PID closed-loop control of the employed temperature

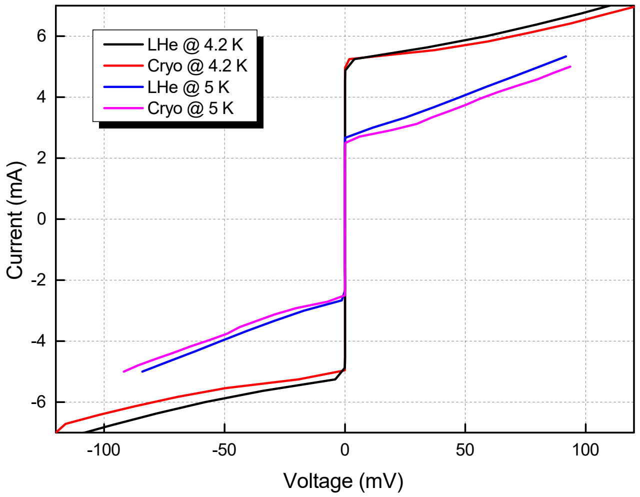

Figure 6.5: Current-voltage characteristics of the JAWS device at different temperatures in LHe and cryocooler.

measurement instrument (Lake Shore 350 [234]). Curves measured in cryocooler have been averaged to filter out the induced critical current oscillations ($\sim 0.5\,\mathrm{mA}$). For a fixed operating temperature, critical currents I_c are similar in both conditions: this means that the temperature of the Josephson array in cryocooler is consistent with the temperature of the He bath, according to the values measured by the temperature sensors.

6.2.2 Characterization under microwave radiation

JAWS metrological properties can be preliminary assessed by studying the array response to a continuous wave (CW) sinusoidal signal, here provided by an HP-83711 synthesizer [286]. The first characterization was performed in LHe, where the high-thermal conductivity of the liquid cryogen easily dissipates the rf heat.

The array under test was designed for a PPG with 15 GHz maximum operating frequency (RZ pulses). Indeed, as can be evaluated from the current-voltage curves in Fig. 6.5, $V_c = I_c R_n = 4.6\,\mathrm{mA} \times 5\,\mathrm{m\Omega} \simeq 23\,\mu\mathrm{V}$ at 4.2 K, which leads to a characteristic frequency f_c around 11 GHz. The large steps obtained under the 10 GHz radiation are then motivated by the operating conditions close to this optimal value. Differently, owing to the resistance of the thermal links, heat dissipation is reduced in cryocooler. This leads the chip temperature to increase when radiated [275] and to lower the effective I_c, with the consequent reduction of f_c that partially compensates for the higher fabrication value. In order to study the combined effect of both contributions in the measurements in cryocooler, the step properties under CW irradiation were first analyzed at different temperatures and microwave

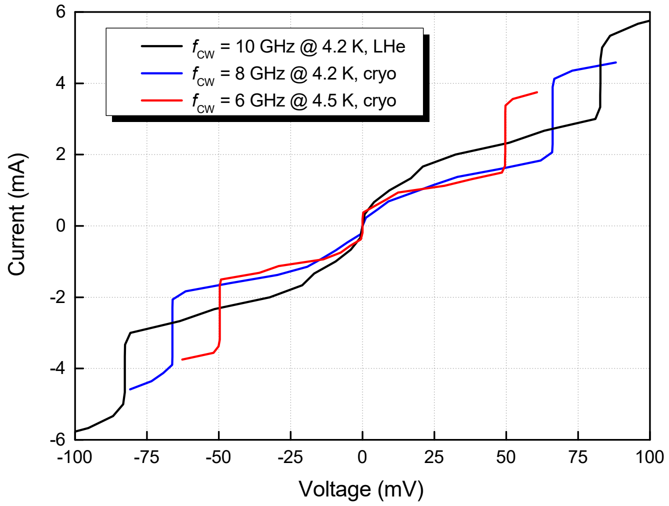

Figure 6.6: Current-voltage characteristics of the JAWS device under CW radiation at different temperatures in LHe and cryocooler

frequencies. The results are shown in Fig. 6.6, along with the steps obtained in LHe at 10 GHz. For each frequency value, temperature and rf power were adjusted to maximize the amplitude of first order steps. These results indicate that adequately wide quantum steps can be obtained at lower rf frequencies. In addition, in spite of the expected increase of junctions temperature, the optimal temperature range at the frequencies of interest is still above 4.2 K. The rf power required for generating suitable steps, which ranges from 2 to 8 mW, is then effectively dissipated on the coldplate, with no significant consequences for the array behavior.

After demonstrating that the chip was working well under CW radiation, its response under rf pulses has been investigated. The employed PPG was an Anritsu MP1763C[1][287], which generates two-level NRZ-pulses with maximum clock frequency of 12.5 GHz. Since the correct operation of JAWS standards requires RZ-pulses, the effective maximum repetition frequency was about 6 GHz, realized by setting a '10101010...' output pattern, where '1' and '0' respectively mean 'pulse' and 'no-pulse'. Fig. 6.7 shows a comparison between the current-voltage curves observed under CW and pulses radiation at equal frequency and temperature (6 GHz, ~ 4.5 K), with voltage steps amplitude larger than 1 mA in both cases. A current-voltage curve exhibiting almost equally wide zero and first steps is shown in Fig. 6.8, along with a zoom of the first quantum step, where ~ 1 mA quantum margins are demonstrated with better resolution.

---

[1] Kindly lent by PTB for cooperation within the Q-WAVE project [279].

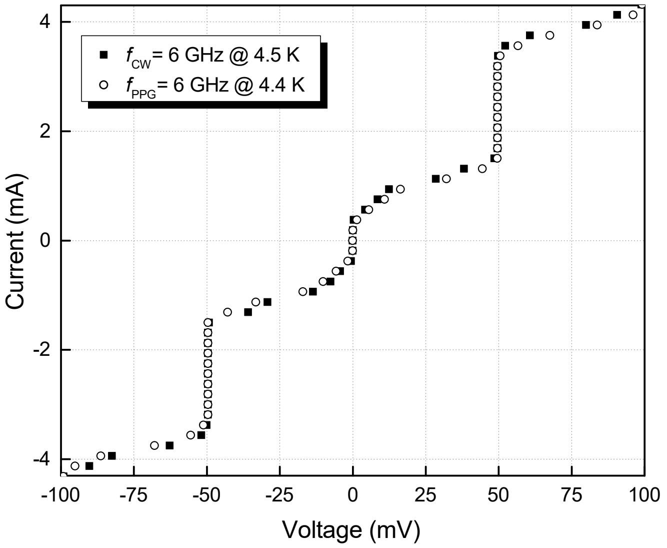

Figure 6.7: Current-voltage characteristics of JAWS array under CW and pulsed 6 GHz radiation at $T \simeq 4.5\,\mathrm{K}$ in cryocooler.

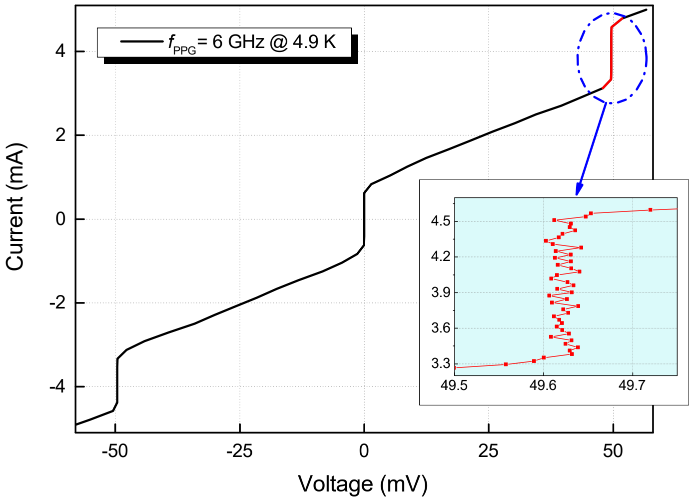

Figure 6.8: Current-voltage characteristic of JAWS array under 6 GHz pulsed radiation at $T \simeq 4.5\,\mathrm{K}$ in cryocooler. The inset shows an higher resolution plot of the first quantum step.

6.3 JAWS waveform synthesis

After this first dc and ac electrical characterization, which proved that the implemented cryocooled system is appropriate to operate JAWS devices, unipolar and bipolar waveform synthesis tests have been carried out. To that aim, the ac-coupling technique, described in Sec. 2.3.2, has been employed.

6.3.1 Unipolar sine waves

Since the PPG initially in use provides two-level bit patterns, only unipolar waveforms could be synthesized. The $\Sigma\Delta$ bit-sequences that encode the desired sine waves were provided by PTB, along with the LabView software used to upload them into the PPG memory.

To find the optimal operating conditions, displaying the array current-voltage characteristics is also useful. Yet, the two Keithley instruments employed in the previous dc and ac electrical characterization are too slow to properly monitor the array response to the modulated rf-pulsed signal. Therefore, as shown in Fig. 6.9, an AWG (Agilent 33250A [235]) was used to generate a faster current-sweep, whilst

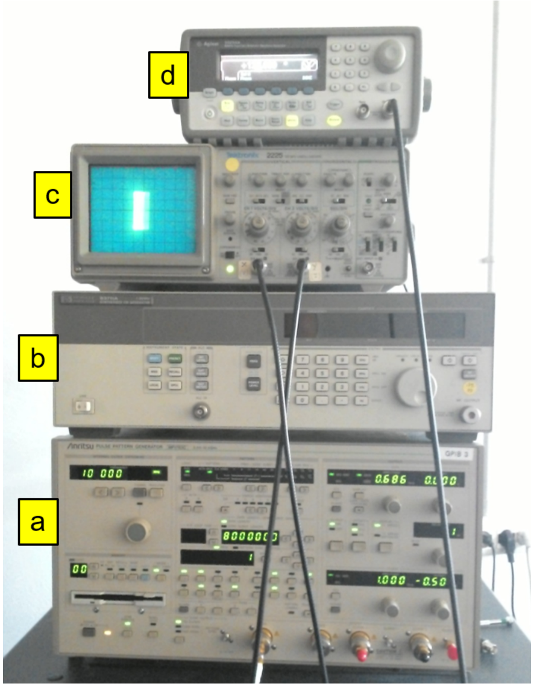

Figure 6.9: Part of the measurement setup employed for the unipolar waveform synthesis test with JAWS: a) PPG Anritsu MP1763C; b) HP-83711 CW synthesizer, employed in ac characterization; c) Fast analog oscilloscope to display high-speed current-voltage characteristics; d) AWG Agilent 33250A as fast current source.

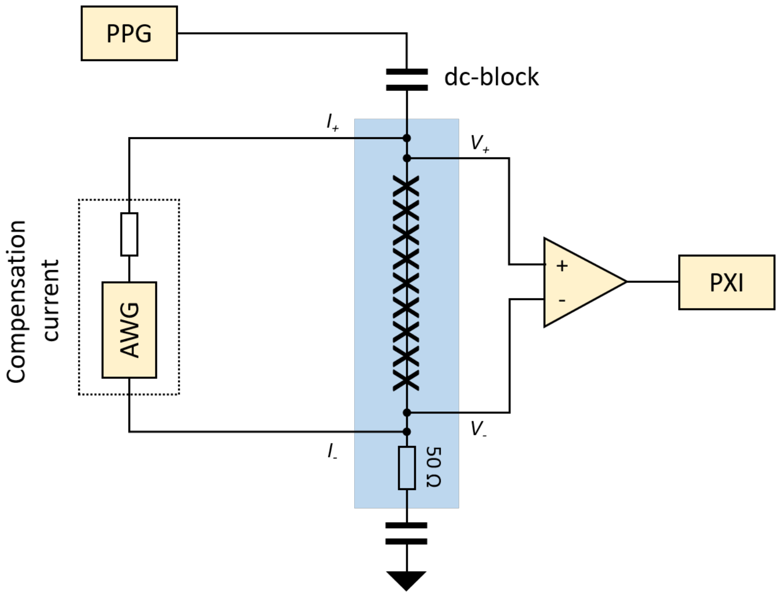

Figure 6.10: Experimental setup for the synthesis of unipolar waveforms with JAWS. The two capacitors represent a single inner/outer dc block

an analog oscilloscope was employed to visualize the array current-voltage curves. Pulses amplitude and cryocooler temperature are properly adjusted to optimize the quantum behavior of the Josephson array.

The overall measurement setup is represented in Fig. 6.12. To realize ac-coupling, an inner/outer dc-block was inserted between the coaxial cable and the SMA-launcher of the holder. The required low-frequency compensation signal was provided by the same AWG used for the current-sweep. A National Instruments PXI5922 sampler [288] was employed to digitize the waveform synthesized by the JAWS array. A battery-operated differential pre-amplifier (SRS-SR560 [237]) was inserted between the JAWS output and the input of the digitizer, with the aim of avoiding ground-loops. Data sampled by the PXI system were processed in real-time, allowing the generated waveforms to be visualized and measured in time and freqency domain.

Unipolar sinusoidal waveforms with peak-to-peak amplitude up to 33 mV and harmonic distortion better than −80 dBc have been synthesized at frequencies around 1 kHz. Fast Fourier Transform (FFT) frequency spectra of two sine waves at 5 K and clock frequency of 10 GHz are shown in Fig. 6.11.

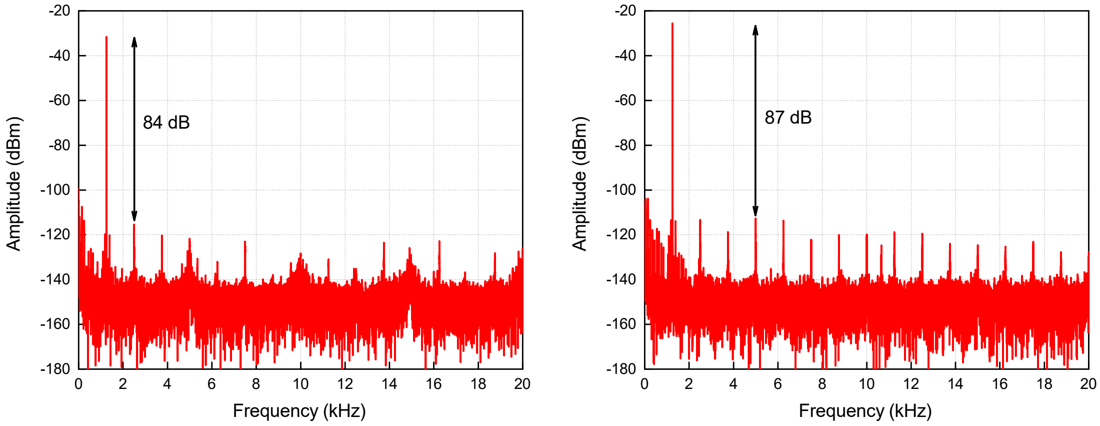

(a) (b)

Figure 6.11: FFT spectra of two unipolar sine waves obtained in cryocooler at $T \simeq 5\,\mathrm{K}$. (a) $V_{pp} = 16.53\,\mathrm{mV}$, $f = 1.25\,\mathrm{kHz}$ and $A_{\Sigma\Delta} = 40\,\%$. (b) $V_{pp} = 33.06\,\mathrm{mV}$, $f = 1.25\,\mathrm{kHz}$ and $A_{\Sigma\Delta} = 80\,\%$. The rms voltage amplitude in the y-axis is expressed in dBm considering a $50\,\Omega$ reference impedance.

6.3.2 Bipolar sine waves

Following tests with a new PPG were carried out: this novel pulse-source system includes two Anritsu MU181020B modules installed on a MP1800A mainframe [289]. Each module delivers two-level NRZ-pulses with a maximum clock frequency of 14 GHz, provided by an external clock synthesizer (HP-83711 CW). The simultaneous use of two MU181020B modules enables the generation of three-level RZ-pulses with a highest repetition frequency of 7 GHz.

A Python script, based on the *python-deltasigma* library [290], has been developed to create the required three-level $\Sigma\Delta$ codes, which now contain the digits '-1', '0', '1', namely 'negative pulse', 'no pulse' and 'positive pulse', respectively. Two separated binary codes are then obtained from this one and separately loaded on the two PPG modules' memory. One of the two modules works as master, thus providing the trigger signal to the other, whose trigger delay can be finely tuned to vary the phase between the two pulsed signals. Afterwards, these are combined by means of a high-frequency splitter, whose output is sent to the JAWS array via the usual stainless-steel coaxial cable.

The adoption of this new PPG allowed us to synthesize bipolar waveforms and, consequently, to considerably increase the peak-to-peak voltage amplitude, compared to the previous case. FFT spectra of two $20\,\mathrm{mV_{rms}}$ sine waves ($V_{pp} = 56.57\,\mathrm{mV}$) of frequencies 1 kHz and 10 kHz are shown in Fig. 6.12. Harmonic distortion around $-90\,\mathrm{dBc}$ was achieved in both cases. However, differently from

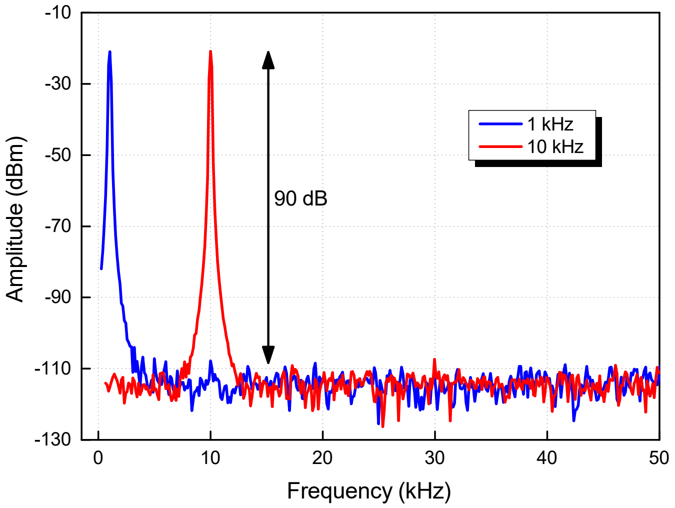

Figure 6.12: FFT spectra of two bipolar sine waves synthesized with the JAWS device in cryocooler at $T \simeq 5\,\mathrm{K}$, $V_{rms} = 20\,\mathrm{mV}$, $1\,\mathrm{kHz}$ (blue) and $10\,\mathrm{kHz}$ (red), $A_{\Sigma\Delta} = 48.8\,\%$. The rms voltage amplitude in the y-axis is expressed in dBm considering a $50\,\Omega$ reference impedance.

Sec. 6.3.1, these were measured with an FFT dynamical signal analyzer (Agilent 35670A [291]), which exhibits a higher noise-floor level compared to the PXI digitizer. Hence, it may be expected that the real harmonic distortion is higher than measured.

In addition, in this new configuration, the voltage signal from the JAWS array was transmitted to the laboratory environment via a 50 cm long flexible coaxial cable with both internal and external conductors made of silver-plated copper and $50\,\Omega$ characteristic impedance, thus replacing the longer and unshielded twisted-pair manganin leads previously used. Despite the cable was thermalized, it resulted in additional thermal loading to the cryocooler that slightly affected its lowest temperature, but sufficient for the JAWS array operation at $T \simeq 5\,\mathrm{K}$.

6.3.3 Towards the mitigation of voltage cable systematic errors

As described in Sec. 2.3.3, the voltage read by the ac voltmeter in the laboratory environment (henceforth referred as the DUT) differs from the calculable voltage provided by the JAWS array as a result of frequency-dependent systematic errors.

The deviation follows approximately the relation

$$\frac{V_{DUT}}{V_{JAWS}} \simeq 1 + 2\,\pi^2\, f^2\, L\, C \tag{6.1}$$

where L and C are the equivalent inductance and capacitance of the circuit, hence including DUT and output voltage line. Using a shorter voltage cable is the most straightforward solution to reduce these errors, since both L and C values are related to its length.

To assess the effectiveness of the 50 cm long coaxial cable, ac-dc differences have been measured from 1 kHz to 1 MHz by means of a calibrated Fluke 792A TTS [93]. The experimental setup is schematically depicted in Fig. 6.13: a Keysight 3458A multimeter [292] was used to measure the TTS dc voltage output, whereas, owing to the limited bandwidth of the 35670A FFT analyzer (< 50 kHz), a digital oscilloscope (Teledyne-LeCroy HDO6034A [239]) has been employed to observe the frequency spectra of JAWS sine waves above 20 kHz. As shown in Fig. 6.14, the TTS is directly connected to the vacuum-system flange through a series of adapters and a tee connector. The overall length of the output line was then approximately equal to 60 cm. The N-type tee connector allowed to connect in parallel the TTS and the spectrum analyzer, thus simplifying the measurement procedure. However, to avoid possible systematic errors, the spectrum analyzer was detached from the tee during the ac-dc measurements.

Ac-dc differences have been measured at rms amplitudes of 5 mV and 20 mV, with the TTS in the 22 mV range. The 5 $\mathrm{mV_{rms}}$ value made it possible to synthesize

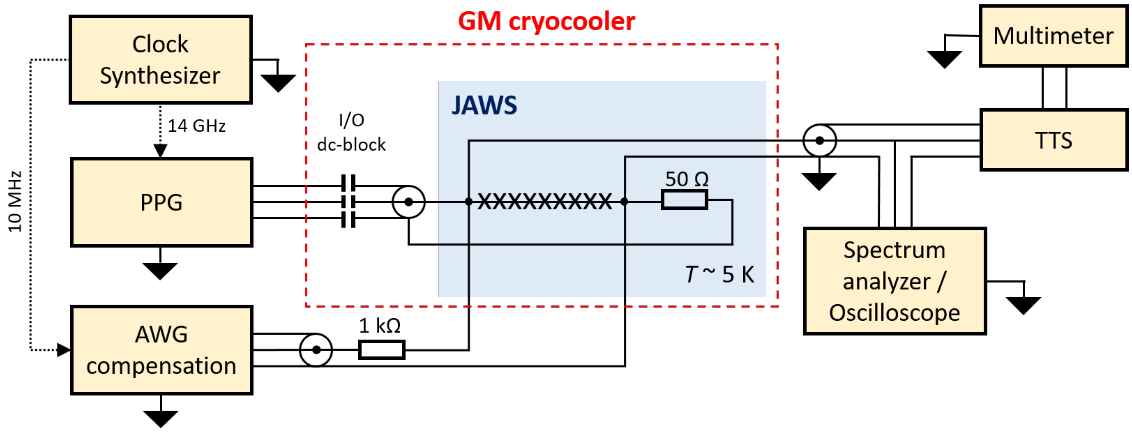

Figure 6.13: Experimental setup of the ac-dc difference measurements with the JAWS device. A spectrum analyzer and a digital oscilloscope were alternatively used to observe the FFT spectra of the synthesized sine waves for different frequency ranges, owing to the limited bandwidth of the former.

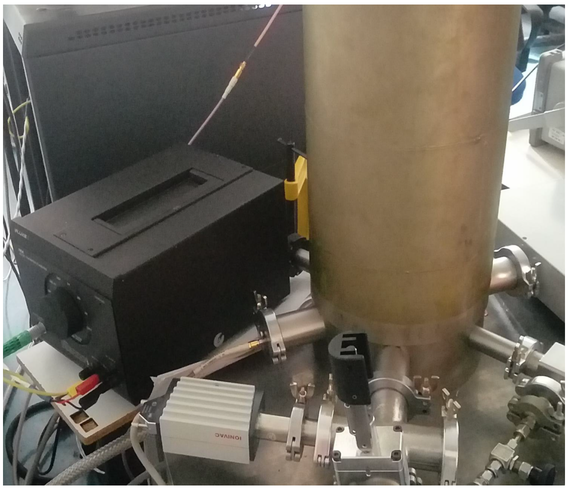

(a)

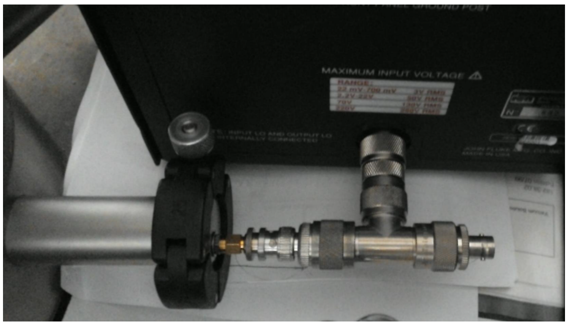

(b)

Figure 6.14: Photographs of the cryocooler setup with the TTS directly connected to the vacuum system flange, where the voltage cable from the JAWS device is internally connected.

sine waves without the need of the low-frequency compensation signal, hence avoiding possibly correlated systematic errors. Measurements were planned as follows: the ac-dc difference at 1 kHz was first measured by consecutively applying a positive dc voltage, an ac voltage and a negative dc voltage, all provided by the JAWS device. Subsequently, faster ac-ac differences were measured, in which measurements at higher frequencies were compared to the average between the previous and the successive 1 kHz results [193].

In Fig. 6.15, the measured ac-dc difference is plotted as a function of the signal frequency, showing an approximate quadratic behavior. Yet, both magnitude and sign appear to disagree with the expected one, calculated via Eq. 6.1. Indeed, using the values of capacitance and inductance per length provided by the cable manufacturer and the 40 pF input capacitance of the TTS, the expected ac-dc difference

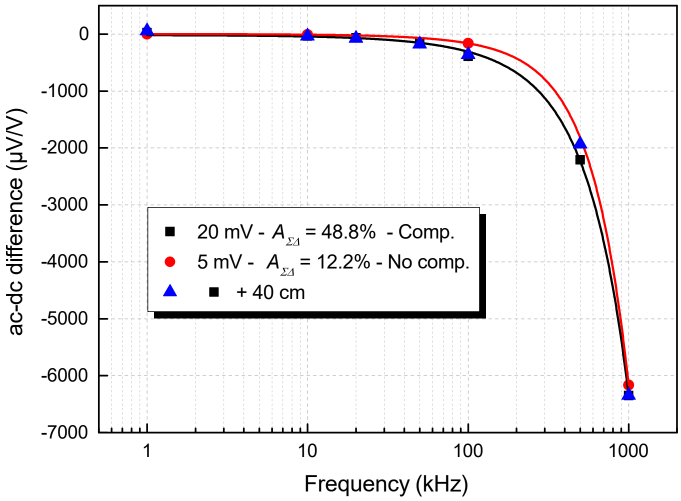

Figure 6.15: Measured ac-dc difference as a function of the signal frequency for three distinct cases: 1) $V_{rms} = 20\,\mathrm{mV}$, with compensation; 2) $V_{rms} = 5\,\mathrm{mV}$, without compensation; 3) $V_{rms} = 20\,\mathrm{mV}$, with compensation and an additional 40 cm long coaxial cable.

at 1 MHz should be about $+300\,\mu\mathrm{V\,V^{-1}}$. The measurement at $5\,\mathrm{mV_{rms}}$ was in fact performed to rule out the possible contribution of the compensation signal lines to this unexpected deviation, but no difference has been noticed. Moreover, the insertion of a 40 cm long extra-cable between vacuum flange and TTS appeared to have no effect on the measured ac-dc difference (Fig. 6.15, blue triangles).

Further investigation is then required to find out the cause of this rather large discrepancies. In particular, quantization and spectral purity of JAWS sine waves have to be verified at higher resolution, especially for upper frequencies.

6.4 Conclusion

In this chapter, activities carried out with pulse-driven Josephson arrays are presented. First, dc and ac electrical characteristics of an array with 4000 SNS junctions were analyzed: measurements were conducted both in LHe and in cryocooler, with the aim of investigating the effects related to the chip dry-cooling and checking the effectiveness of the newly-designed cryopackage. A special stainless steel coaxial cable was used for the rf transmission and interventions to limit the resultant thermal load on the experiment region were successful. Both cooling techniques provide similar results for all relevant parameters, as critical current and normal resistance. In particular, voltage steps $\sim 1\,\mathrm{mA}$ wide have been observed in cryocooler both under CW and pulsed ac excitations. Unipolar and bipolar sine waves have been synthesized with two distinct experimental setups, and harmonic distortions approaching 90 dBc have been achieved. However, ac-dc difference measurements with a commercial TTS showed that further improvements of JAWS quantization and electrical system immunity to external noise are required for the realization of an accurate and reliable cryocooled ac voltage source.

Chapter 7

Application of ac Josephson standards at PTB

Primary dc voltage standards based on the Josephson effect are well established in NMIs. So far, only a few NMIs in Europe have ac quantum voltage standards of amplitudes and frequencies useful in industry calibrations and scientific research. However, these standards are increasingly gaining importance, as they allow us to measure waveforms with uncertainties at the µV/V level a hundred-times faster than ac-dc thermal converters.

In this context, the main purpose of the ACQ-PRO EMPIR project [293] is to spread the access to ac quantum voltage standards between NMIs, transferring knowledge, technical skills and calibration capabilities and allowing the diversification of research and the development of specific industrial applications.

In the scope of the ACQ-PRO project, I spent three months at Physikalisch-Technische Bundesanstalt (PTB), in the Josephson effect working group [294], to gain technical capabilities in the use of advanced ac quantum voltage systems for the calibration of conventional devices. The experimental activities described here are not directly correlated to the measurements performed at INRiM and presented in the previous chapters. For example, Josephson systems I worked with at PTB were based on LHe cooling, whose use is favored by the presence of an efficient He-gas recovery system along with a liquefier. It should be clear that, owing to the relatively short period, the activities described as follows were mostly performed in strict cooperation with PTB scientists. Among the different Josephson systems employed (Sec. 7.1), I gained particular confidence with PJVS-based systems, i.e. ac quantum voltmeters (QVMs), whereas, owing to the higher complexity, pulse-driven Josephson systems were mainly operated with the assistance of PTB experienced researchers. Despite this, I have been involved in the experimental activities as well as in the data analysis and presentation.

7.1 Ac Josephson voltage standards at PTB

7.1.1 Ac quantum voltmeters

As anticipated in Sec. 2.2.1, quantum voltmeters (QVMs) calibrate the ac voltage from a device under test (DUT) by synchronizing it to a stepwise version of the same sine wave from a PJVS. Their difference is then measured by a sampler, acting as a null-detector and, thus, improving the overall calibration accuracy. The phase between the two waveforms is adjusted to get a balanced difference signal, meaning that the waveform under test crosses the PJVS waveform at the center of each quantized step (Fig 7.1b). The PJVS voltage can be rapidly switched and the uncertainties arising from the transients, where the voltage is unpredictable, is eliminated by discarding the sampled points in proximity of each transition. Finally, the DUT waveform is reconstructed from the measured differences and their associated, and exactly known, Josephson voltage steps.

Two distinct QVM systems have been used, identified as QVM-1 and QVM-2. QVM-1 is shown in Fig. 7.2: it makes use of five synchronized LeCroy ArbStudio 1104 AWGs[1], each with four output channels, to drive a 10 V PJVS with 69 632 $Nb/Nb_xSi_{1-x}/Nb$ junctions, subdivided into 22 segments (only 16 used) and rf-operated at 70 GHz [127]. QVM-2 used a multi-channel bias source, developed at National Physical Laboratory (NPL) [295], to drive a 2 V PJVS with 16 384 $Nb/Nb_xSi_{1-x}/Nb$ junctions, subdivided into 14 segments, also radiated at 70 GHz [166]. LHe at 4.2 K have been exploited to cool the PJVS arrays, suitably installed

---

[1] Now commercialized by Active Technologies [272].

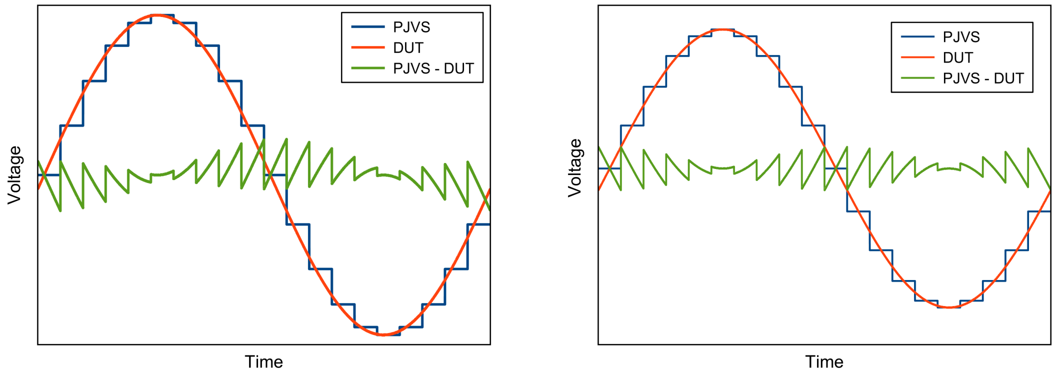

(a) (b)

Figure 7.1: Unbalanced (a) and balanced (b) difference signals (green) between PJVS (blue) and DUT (red) waveforms.

Figure 7.2: Photograph of the QVM-1 system

at the top of low-conductivity stick probes and immersed into the liquid cryogen. Both QVM-1 and QVM-2 bias sources were electrically isolated from ground: the NPL source has an internal isolation transformer, whereas the ArbStudio 1104 AWGs were battery-operated. In addition, both sources were connected to the computer via an optically isolated USB extender. Both QVMs systems used a phase-locked oscillator [296] as 70 GHz microwave source, referenced to the 10 MHz signal provided by the PTB's atomic clock. Each QVM had its dedicated NI-PXI5922A ADC [288], optically connected to the computers and capable of working in battery-mode.

A custom LabView software remotely controls the employed instrumentation and sets the main parameters, such as rms output voltage, frequency, number of quantum steps, number of ringing points to delete, microwave power, sampling frequency, etc. The number of quantized steps per period was set to 20 for all the measurements. If it were higher, the difference signal measured by the sampler would decrease, and its linearity and gain errors would become less important. Yet, the number of steps is limited by the settling time after each transition between the PJVS voltage levels. Therefore, as proven in Ref. [127], the choice of 20 samples per period results to be a good compromise.

7.1.2 Josephson arbitrary waveform synthesizers

At PTB, JAWS systems make use of ac-coupling technique (Sec. 2.3.2). All compensation signal sources were electrically decoupled from the Josephson array by means of PTB-built electronics, henceforth referred as IV-boxes [159].

Two LHe cooled JAWS systems have been used for calibrating ac voltage sources. For calibrations in the 1 V range, the JAWS system described in Ref. [159] and shown in Fig. 7.3a was used. It consists of four chips with two arrays each, for a total of 63 000 Nb/Nb$_x$Si$_{1\text{-}x}$/Nb junctions arranged in three stacks. The eight arrays are series-connected via superconducting wires. Each array requires its dedicated compensation signal and pulse transmission line, so four two-channel AWGs (Agilent 33522B [297]), an eight-channel IV-box, and an eight-channel Sympuls PPG [298] have been employed. For calibrations up to 250 mV, a single chip with two arrays, each with 7500 triple-stacked Nb/Nb$_x$Si$_{1\text{-}x}$/Nb junctions, has been employed. It is basically identical to the 1 V system, apart from the lower number of channels required (from eight to two). Therefore, only a single dual waveform generator, a two-channel IV-box, and a two-channel PPG are needed (Fig. 7.3b). Both systems used a PXI5922A ADC as FFT analyzer. In addition, both PPGs were externally-clocked at $f_{clock} = 14\,\text{GHz}$ and provide RZ pulses, so that the maximum pulse repetition frequency equals f_{clock}. A custom LabView software was used to control the instrumentation. For each channel, i.e. each array, four operating parameters have to be adjusted: positive and negative pulse amplitudes and compensation signal amplitude and phase. A sweep current was also applied

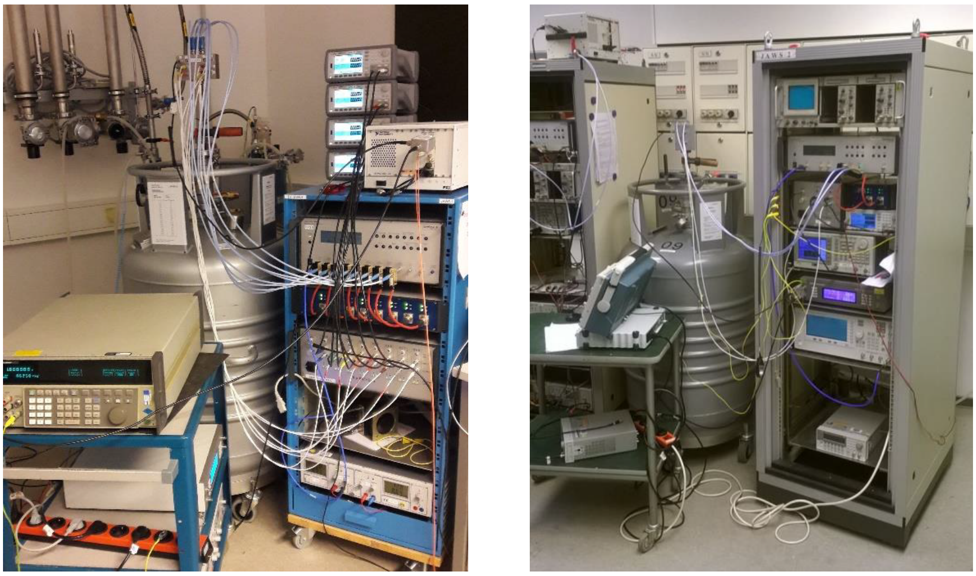
(a) (b)

Figure 7.3: Photographs of the 1 V (a) and the 250 mV (b) JAWS systems

to each array to evaluate the width of the quantum operating range, i.e. where the frequency spectrum of the synthesized waveform does not change [166]. After the individual adjustment of each array's parameters, these are switched on simultaneously and a final minor adjustment is performed to compensate for possible crosstalks.

The lowest signal frequency is given by f_{clock}/M, with M the PPG memory size (256 Mbit in this case). In spite of this, it is possible to reach lower frequencies by exploiting the "word repetition" function of Sympuls PPGs, that allows to repeat each 128 bit word of the code from one to eight times. This makes the output waveform "less pure" than without word repetition, but due to the high OSR, it still allows to get clean frequency spectra.

In the same way of QVMs, calibration of ac voltage sources with JAWS are based on a difference measurement, usually with a lock-in amplifier as null-detector. It is not possible to exploit the lock-in technique in QVM systems in that it does not allow to discard a given number of ringing points.

7.2 Measurements

7.2.1 Real-time indirect comparison of two ac-QVMs

A real-time indirect comparison of the two ac-QVMs at rms amplitude of 1 V and frequency of 1.25 kHz has been performed through the calibration of three different DUTs, hence acting as transfer standards. These are a Fluke 5720A calibrator [299], an AudioPrecision APx-555 [300], and a *präzise doppelwellenform quelle* (PDWQ), a custom dual waveform source designed for ratio measurements [301].

The clock, trigger and electrical connections scheme of the setups is shown in Fig. 7.4. An AWG (Keithley 3390 [302]) was used as clock source for the DUT timing: the phase between measuring and reference waveforms was typically adjusted by manually detuning it until a balanced difference was obtained. The DUT waveform was alternately sent to either QVM-1 or QVM-2 by means of a computer-controlled switch.

Fluke Calibrator 5720A

The measurements were performed by switching between the two systems approximately every 60 s, during which the average rms of the reconstructed waveform was recorded. Fig. 7.5 shows the differences between measured and nominal values for a series of alternate data acquisitions. The error bars for each data point is given by the Allan deviation of the single acquisition. QVM-1 provided an average difference of $(-5.71 \pm 0.12)\,\mu\mathrm{V}$, while QVM-2 measured $(-6.34 \pm 0.40)\,\mu\mathrm{V}$. The type-A uncertainties have been evaluated via Allan deviation analysis, in that the

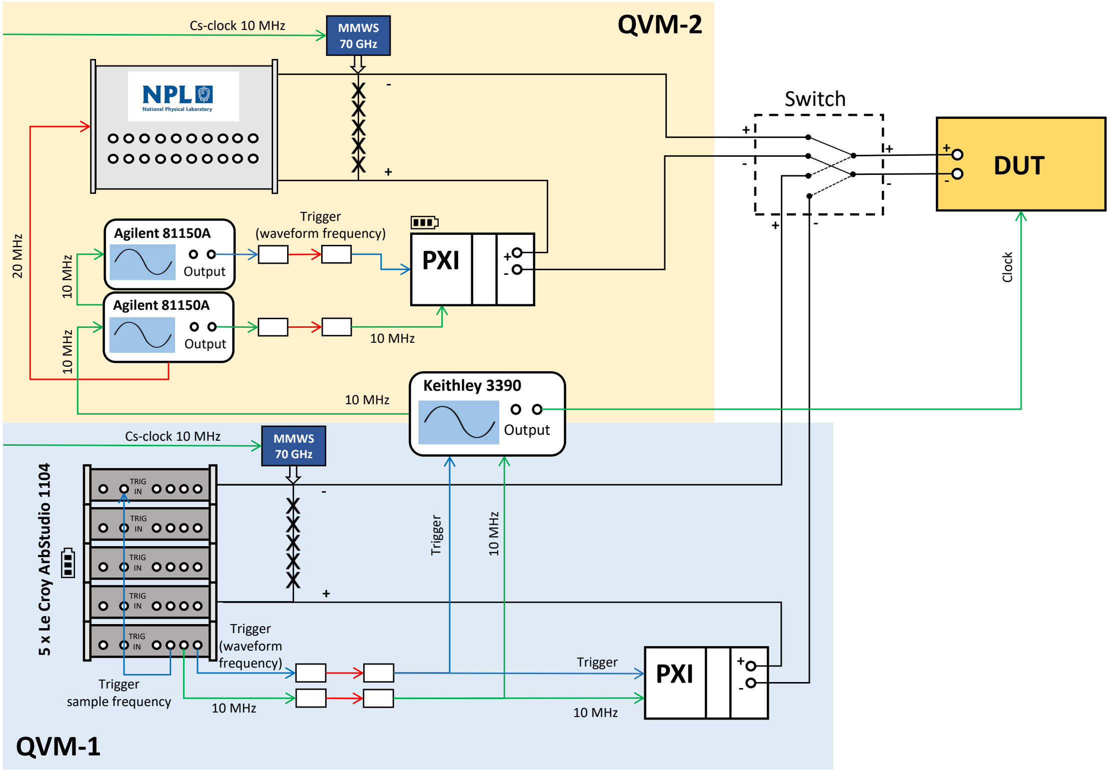

Figure 7.4: Schematic representation of the measurement setup for the indirect ac QVMs comparison with a DUT as transfer standard. Green, blue and red lines represent clock, trigger and optical fiber connections, respectively.

typical standard deviation of the mean, valid in white noise regime [303], would underestimate the uncertainty value.

Finally, the difference between QVM-1 and QVM-2 was $(0.63 \pm 0.42)\,\mu\text{V}$, for a $k = 1$ coverage factor.

AudioPrecision APx-555

The measurement procedure is the same described in the previous section and results are summarized in Fig. 7.6. In Fig. 7.6a, it can be seen that the readings were affected by the drift of the DUT, so an assessment of the agreement between the QVMs is illustrated in Fig. 7.6b, where the data points are calculated as the difference between one point measured with a QVM and the average of the two adjacent points measured with the other. In this way, the drift has been corrected and the average difference between QVM-1 and QVM-2 equals $(0.17 \pm 0.05)\,\mu\text{V}$ $(k = 1)$.

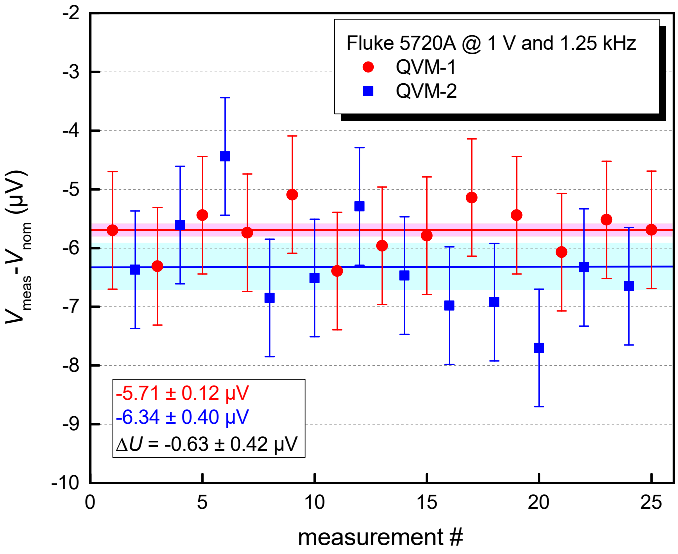

Figure 7.5: Differences between measured and nominal rms voltage of Fluke Calibrator 5720A at 1 V_{rms} and 1.25 kHz with QVM-1 (red) and QVM-2 (blue). The shaded areas represent the uncertainties of the two mean values, estimated via Allan deviation analysis, while the error bars in each single point represent the Allan deviation of the individual measurement.

PDWQ with LC-filter

Differently from the former DUTs, the PDWQ requires an optical clock signal, therefore an opto-coupler has been used to convert the Keithley 3390 AWG output into light pulses.

PDWQ waveforms are affected by a high number of glitches, thus making the measurement strongly dependent on the recorded time windows. These glitches have been reduced by means of an LC-filter, whose effects are analyzed in the appendix of this chapter (Appendix 7.4).

The measurement procedure is the same described in the previous sections and results are summarized in Fig. 7.7. In Fig. 7.7a, it can be seen that the readings were again drift-influenced. An assessment of the agreement between the QVMs is shown in Fig. 7.7b, where the drift has been corrected as illustrated in Sec. 7.2.1: the average difference between QVM-1 and QVM-2 was then $(-0.01 \pm 0.30)\,\mu\mathrm{V}$ ($k = 1$).

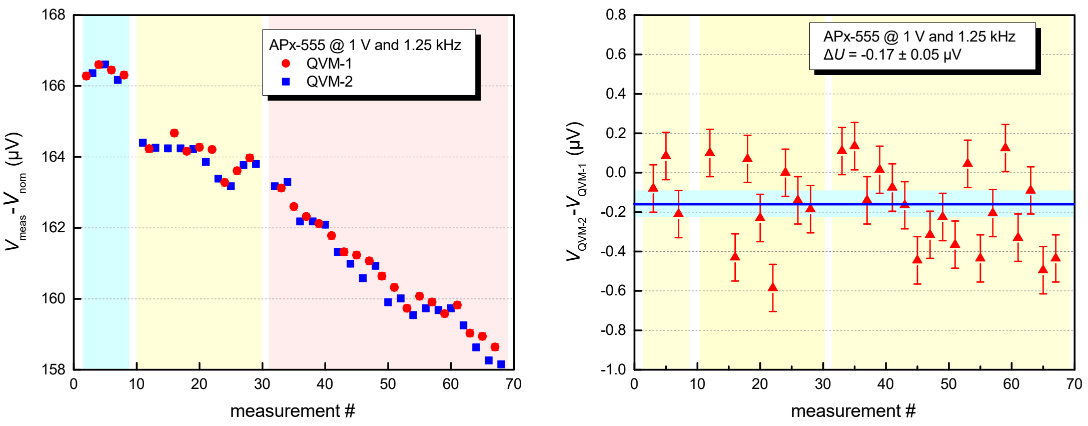

(a) (b)

Figure 7.6: (a) Differences between measured and nominal rms voltage of APx-555 at 1 V_{rms} and 1.25 kHz with QVM-1 (red) and QVM-2 (blue). (b) Voltage differences between QVM-1 and QVM-2, properly drift-corrected. The blue shaded area represents the uncertainty of the mean value, estimated via Allan deviation analysis, while the error bars in each single point represent the Allan deviation of the individual measurement.

7.2.2 Calibration of devices with QVM-1 and JAWS

A Fluke Calibrator 5700A and the PDWQ have been calibrated at different frequencies and rms voltages using QVM-1 and the two JAWS systems. Measurements were carried out in different days and in different laboratories, hence not in real-time as for the QVMs comparisons.

As already mentioned, since JAWS waveforms are not affected by the transients issue, the difference signal can be accurately measured with a lock-in amplifier, a Signal Recovery DSP7265 [240]. The phase between JAWS and DUT was set by manually detuning the DUT clock, provided by an AWG, until the in-phase component of the difference signal was minimized. A further check was done by slightly increasing the JAWS rms voltage: no changes in the quadrature component were expected if the phase was correctly set. The magnitude of the difference signal was then evaluated by averaging the in-phase component data points.

The system configuration for the measurements with the 250 mV JAWS is depicted in Fig. 7.8. The 1 V JAWS calibration setup was very similar, with the difference that eight series-connected arrays, an eight-channel PPG, an eight-channel IV-box, and four two-channel AWGs for the compensation signals were employed. The system setup for the measurement with QVM-1 is the same of Fig. 7.4, though here the switch was not used and the DUT was directly connected to QVM-1.

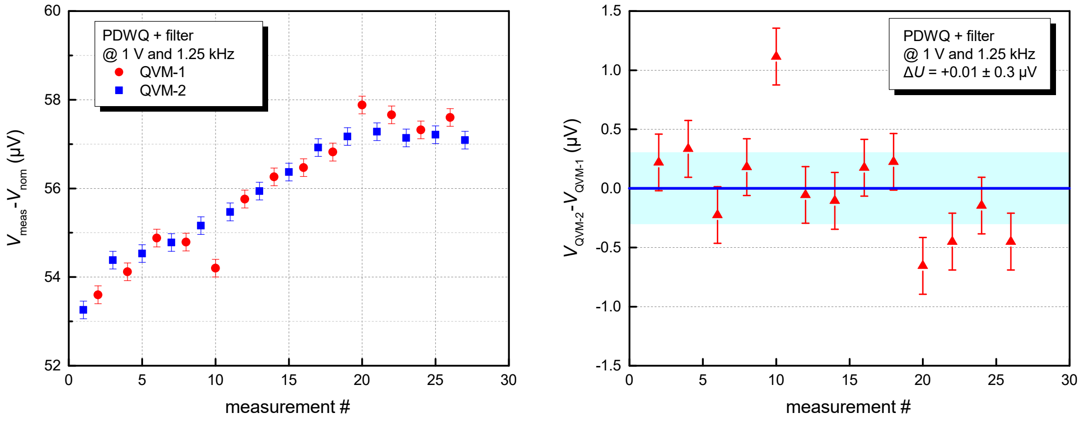

(a) (b)

Figure 7.7: (a): Differences between measured and nominal rms voltage of PDWQ + LC-filter at 1 V_{rms} and 1.25 kHz with QVM-1 (red) and QVM-2 (blue). (b): Voltage differences between QVM-1 and QVM-2, properly drift-corrected. The blue shaded area represents the uncertainty of the mean value, estimated via Allan deviation analysis, while the error bars in each single point represent the Allan deviation of the individual measurement.

Fluke Calibrator 5700A

A Fluke 5700A has been calibrated at rms voltages of 1 V and 100 mV and frequencies of 625 Hz and 1.25 kHz. A high instability of the difference signal occurred with the 1 V JAWS system, probably because of some ground-loops. Therefore, a battery-operated PXI5922A digitizer has been employed as null-detector, in place of the lock-in amplifier. In this case, the phase was set by observing the frequency spectrum of the difference signal and minimizing the peak at the signal frequency.

The results of this calibration are shown in Fig. 7.9: the data points represent the average values of about 10 minutes of continuous data acquisition, except for the data taken with the PXI, evaluated from a single-shot FFT. The error bars for the long-acquisition data points, obtained via Allan deviation analysis, are comprised between 0.1 and 0.4 µV/V, whereas an uncertainty of 1 µV is assigned *a priori* to the PXI measurements. Relative differences between the two systems span from 4 to 13 µV/V, probably affected by some systematic errors.

PDWQ without LC-filter

The PDWQ has been calibrated at rms voltages of 1 V and 100 mV and frequencies of 12.5, 80, 312.25, 625 and 1250 Hz. Here, the LC-filter was not used, because the consequent drift (see Appendix 7.4) made it impossible to use the PDWQ +

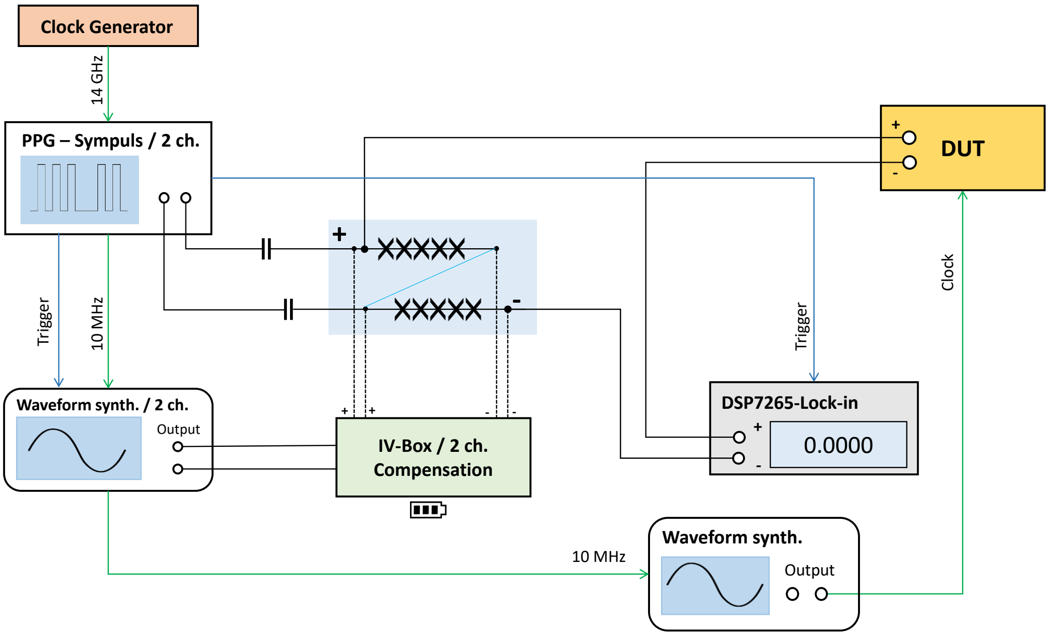

Figure 7.8: Schematic representation of the measurement setup for the DUTs calibration with the 250 mV JAWS. Green and blue lines represent clock and trigger, respectively.

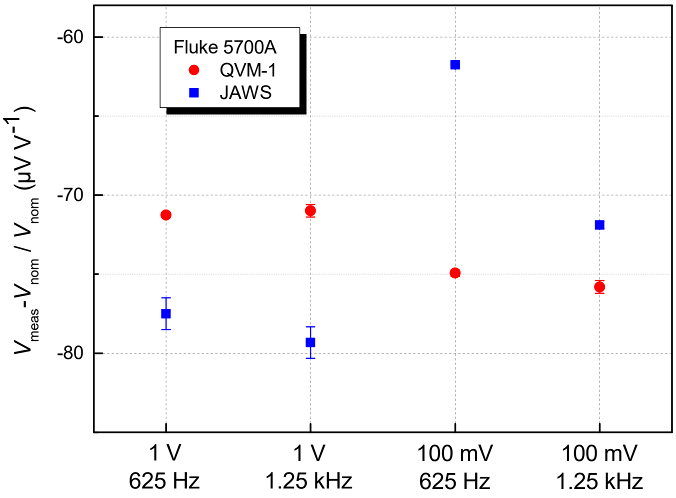

Figure 7.9: Relative differences between measured and nominal rms voltage of Fluke 5700A with QVM-1 and JAWS.

filter as transfer standard for measurements in different times.

The results of this comparison are shown in Fig. 7.10a: the data points represent

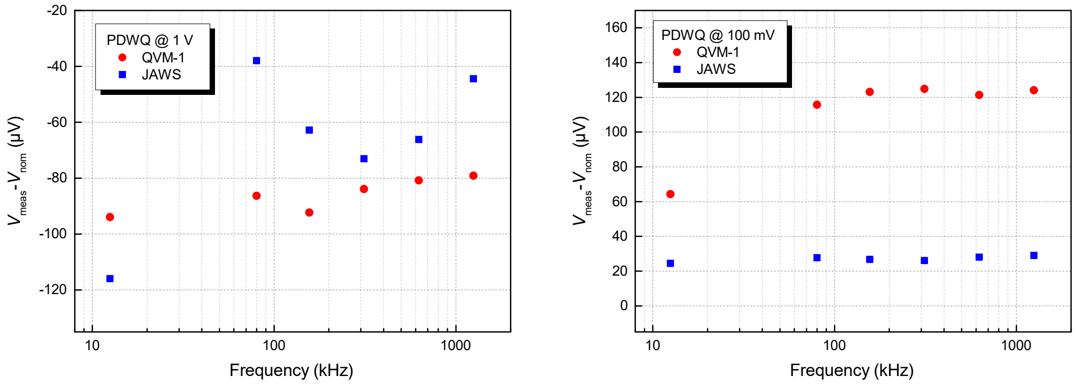

(a) (b)

Figure 7.10: Differences between measured and nominal rms voltage of the PDWQ with QVM-1 and JAWS at 1 V_{rms} (a) and 100 mV_{rms} (b).

the average values of a 10 minutes data acquisition, with error bars obtained via Allan deviation analysis and always below 1 µV. The difference of the two systems at 1 V_{rms} is between 10 and 50 µV, whereas for the measurements at 100 mV_{rms} differences up to 100 µV have been obtained. Possible causes of this considerable disagreement are listed as follow:

1. the PDWQ is not a stable source and is mainly used for ratio measurements using its two output channels. The measurements were performed in different weeks and the device has been rebooted several times in the meantime;
2. the PDWQ measurements strictly depend on the recorded time-windows, owing to the glitches affecting the supplied waveform (see Appendix 7.4) and to the fact that the QVM does not measure the complete waveform;
3. some systematic errors or interferences may have occurred. Measurements were conducted in two different labs, both thermo-controlled, one of which (QVM-1) was EMI-shielded too;
4. the lock-in technique extracts the signal frequency component of the measured difference between JAWS and DUT. Nevertheless, the PDWQ frequency spectrum exhibits large harmonic components that are not taken into account in the measurement.

7.3 Conclusion

Several comparisons between different ac quantum voltage systems have been performed at PTB in the scope of the ACQ-PRO EMPIR project. Real-time indirect comparisons of two different ac-QVMs has been carried out via the calibration of conventional devices at 1 V_{rms} and 1.25 kHz, achieving an agreement at the 1 µV-level and below. Indirect comparisons between JAWS and ac-QVM systems have been performed by calibrating two devices in different ranges of voltages and frequency. In this case, differences up to 1 mV/V have been measured, showing that some systematic errors, interference or other factors may affect the measurements, whose causes need to be further investigated.

7.4 Appendix: analysis of PDWQ

The PDWQ is a home-built two-channels DAC, mainly employed for the measurement of the ratio of electrical quantities. As anticipated, PDWQ sine waves are affected by many glitches:

In the indirect comparison of the two ac-QVMs with the PDWQ as transfer standard (Sec. 7.2.1), an LC-filter was used for canceling these glitches and “smoothing” the output waveform. The comparison between filtered and non-filtered sine waves is shown in Fig. 7.11: the filtered waveform does not exhibit any glitches, thus allowing a time-window independent calibration of the PDWQ.

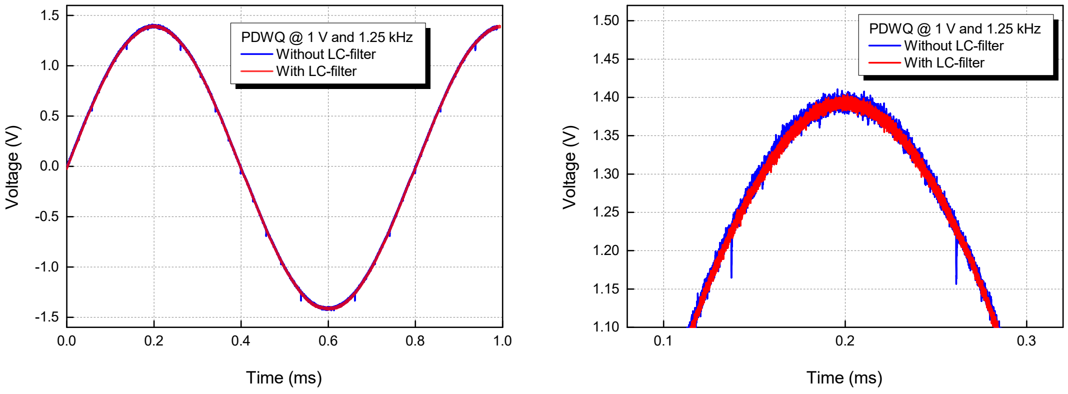

(a) (b)

Figure 7.11: (a) Filtered (red) and non-filtered (blue) sine waves at 1 V_{rms} and 1.25 kHz synthesized by the PDWQ and recorded by PXI5922A. (b) Zoomed portions of the same filtered and non-filtered sine waves.

The effectiveness of the LC-filter has been proven by studying the dependence between the rms voltage of a PDWQ sine wave, measured with QVM-1, and the number of the deleted ringing points (DRP) in proximity of the PJVS transients, both with and without the filter. The results in Fig. 7.12 show that the measurements with the filter were influenced by a drift caused by the filter itself, hence a correction has been made by measuring the rms at DRP = 10 before and after each acquisition. Each value was then shifted with respect to the average of the two adjacent points at DRP = 10.

It can be seen that, owing to the glitches, rms voltage without the LC-filter is distributed in 23.3 µV, whereas the spread is reduced to 1.8 µV by using the filter and applying the drift-correction.

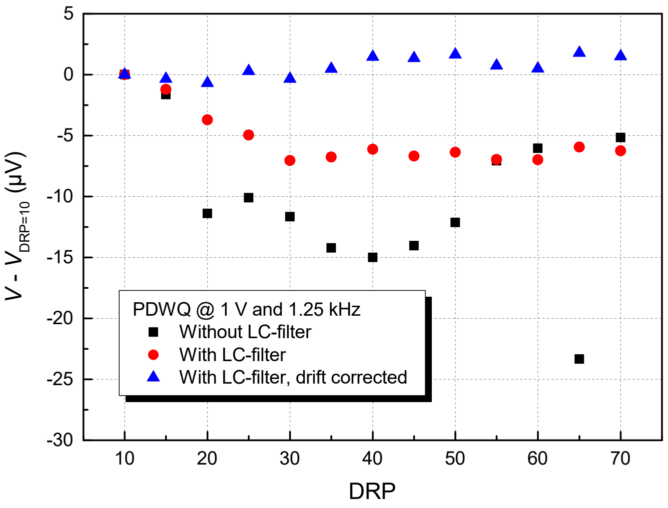

Figure 7.12: Shifted rms voltages of PDWQ at 1 V and 1.25 kHz measured with QVM-1 versus the number of deleted ringing points (DRP), with and without the LC-filter. Data are shifted with respect to the rms value at DRP = 10.

Conclusion

Josephson standards for the synthesis of ac and arbitrary voltage signals are the main subject of this dissertation. With the exception of the last chapter, which shows how these are employed for metrological purposes, this work was mainly focused on the operation of these superconducting devices in cryogen-free refrigeration systems (cryocoolers), which bear a particular interest because of their simplicity and the avoidance of the potentially dangerous liquid cryogen. On the other side, other issues arise, as the annoying thermal fluctuations of a few hundreds of mK and the difficulty of dissipating the heat generated inside the Josephson device.

As a first step, aimed at damping the temperature fluctuations, the dynamic thermal response of a GM cryocooler has been studied, assuming it to be linear around a stable point. System parameters have been derived through the analysis in time and frequency domains, hence providing a cross validation of the results and a preliminary uncertainties estimation. The cryocooler transfer function, given by the ratio in the Laplace space between temperature variation and input power, has been determined at 4 K, and could be useful to realize both passive and active damping techniques. Preliminary tests on active feedbacks were unsuccessful at this temperature and at this oscillation period. Therefore, further work is planned to repeat these experimental analysis at higher temperatures, where cooling powers are larger, and by tuning the frequency of the GM cooler displacer motion.

To enhance heat dissipation in the vacuum environment of a cryocooler, a novel cryopackage, suitable for the operation of PJVS standards at liquid helium temperature and above, has been realized and tested. This package exploits low-temperature properties of materials, as indium and sapphire, suitably organized in a sandwich-structure to significantly increase heat transmission. To reduce thermal contact resistances between the various layers, a special pressing system allows to apply reproducible forces to the sandwich: it is made by a copper bridge hosting a brass screw, whose measured closure torque determines the exerted force and, hence, pressure. In addition, the actual pressure exerted at cryogenic temperature has been estimated from the calculated cryopackage thermal contraction, resulting in a non-negligible increase compared to that applied at room temperature. Though this study was carried out with a 1 V PJVS chip, this cryopackage can be even more effective for the 10 V PJVS version, whose larger contact surface should easily dissipate the large amount of power generated (up to 350 mW) with a limited temperature increase. An open-source software has been developed in *Python* to drive and test each segment of the PJVS array. This program controls four AWGs and a nanovoltmeter, connected to the PJVS device, to check the subarrays current-voltage characteristics, the quantization of their Shapiro steps, and to synthesize stepwise voltage waveforms. The software is modular and easily reconfigurable for different experimental needs. The source code is publicly available on *GitHub*: it is currently in its alpha-stage and is going to be further improved with the addition of new instruments and data analysis tools. Afterward, both software and cryopackage have been exploited to test 1 V PJVS devices made of SNIS junctions in a pulse-tube cryocooler. Operating temperature and microwave power were suitably set to optimize the junctions response, namely to exhibit wide quantum voltage steps for each segment, whose behavior was still affected by the noisy thermal oscillations and by the rather high sensibility of junctions to external magnetic flux. Possible improvements to the state-of-art of PJVS technology have been investigated. In particular, the simultaneous exploitation of first and second voltage steps have been proposed for decreasing the number of junctions and bias lines up to a factor of two. Indeed, the use of all available quantum steps ($n = 0, \pm 1$ and ± 2), allows to encode a generic output voltage in a more convenient form with respect to the conventionally employed binary encoding. These new codifications have been implemented and tested. However, in order to make full use of this peculiar characteristic, a partial redesign of the PJVS chip structure should be undertaken.

Pulse-driven Josephson standards have been also investigated, both in cryocooler and liquid helium. The GM cooler in use has been purposely set to host and adequately thermalize a 50 cm long stainless-steel coaxial cable required for the high-frequency pulses transmission from room temperature to the JAWS array at 4 K. The electrical response of a 4000 SNS junctions array, with and without pulsed excitation, have been measured and showed comparable results for the two different cooling systems, with step amplitudes up to 1 mA. After this preliminary electrical characterization, tests on sinusoidal waveform synthesis have been carried out: first unipolar, by means of a two-level pulse generator and, then bipolar, with a novel PPG system, capable of providing both positive and negative current-pulses. Voltage sine waves with amplitude of few tens of mV and frequency up to the kHz range exhibited satisfactory spectral purity, being harmonics suppressed by more than −80 dB with respect to the fundamental tone. However, approaching the MHz, the deviation of the output voltage measured in the laboratory environment results to be different from that expected from the characteristics of the voltage cable, thus indicating that deeper tests on the real JAWS quantum operation is needed.

Finally, the metrological application of LHe-cooled ac Josephson standards, carried out at PTB, is described in the last chapter. Real-time indirect comparisons of two PJVS-based systems, i.e. ac quantum voltmeters, has been carried out by calibrating conventional devices at 1 V_{rms} and 1.25 kHz, and achieving an agreement at the µV/V level and below. Indirect comparisons between JAWS and PJVS have been conducted in different voltage and frequency ranges: in this case the difference spans from 5 µV/V to 1 mV/V, clearly showing that some systematic errors, interference or other factors may affect the measurements.

Bibliography

[1] Bureau International des Poids et Mesures (BIPM). *The International System of Units SI.* 9th ed. 2019. ISBN: 978-92-822-2272-0.

[2] H. Bachmair. “Electrical Metrology”. In: *Metrology and Fundamental Constants, Course CLXVI.* Ed. by T. W. Hänsch, S. Leschiutta, and A. J. Wallard. Vol. 166. IOS Press, 2007, pp. 95–133.

[3] V. Sienknecht and T. Funck. “Realization of the SI unit volt by means of a voltage balance”. In: *Metrologia* 22.3 (1986), p. 209.

[4] R. Steiner. “History and progress on accurate measurements of the Planck constant”. In: *Rep. Prog. Phys.* 76.1 (2012), p. 016101.

[5] A. M. Thompson and D. G. Lampard. “A new theorem in electrostatics and its application to calculable standards of capacitance”. In: *Nature* 177.4515 (1956), p. 888.

[6] J. Flowers. “The route to atomic and quantum standards”. In: *Science* 306.5700 (2004), pp. 1324–1330.

[7] BIPM et al. *The international vocabulary of metrology - basic and general concepts and associated terms (VIM).* 3rd ed. 2012.

[8] P. Vanysek. *Weston, the Weston Cell, and the Volt.* 2017.

[9] W. Nawrocki. *Introduction to Quantum Metrology. Quantum Standards and Instrumentation.* 1st ed. Poznan: Springer International Publishing, 2015. DOI: `10.1007/978-3-319-15669-9`.

[10] J. Millman and A. Grabel. *Microelectronics.* McGraw-Hill, Inc., 1987.

[11] Fluke Corporation. *732C and 734C DC Voltage Reference Standards.* 2019. URL: `https://eu.flukecal.com/products/electrical-calibration/electrical-standards/732c-and-734c-dc-voltage-reference-standards` (visited on 03/18/2019).

[12] T. J. Witt. “Maintenance and dissemination of voltage standards by Zener-diode-based instruments”. English. In: *IEE Proceedings - Science, Measurement and Technology* 149 (6 2002), pp. 305–312.

[13] D. R. Lide. “A Practical Josephson Voltage Standard at One Volt”. In: *A Century of Excellence in Measurements, Standards, and Technology.* CRC Press, 2018, pp. 315–318.

[14] H. Kamerlingh Onnes. “The resistance of pure mercury at helium temperatures”. In: *Communications from the Laboratory of Physics at the University of Leiden, b* 120 (1911).

[15] M. Tinkham. *Introduction to superconductivity.* 2nd ed. New York: McGraw-Hill, 1996.

[16] W. Meissner and R. Ochsenfeld. “A new effect in penetration of superconductors”. In: *Die Naturwissenschaften* 21 (1933), pp. 787–788.

[17] J. F. Annett. *Superconductivity, superfluids and condensates.* Oxford University Press, 2004.

[18] A. A. Abrikosov. “On the magnetic properties of superconductors of the second group”. In: *Sov. Phys. JETP* 5 (1957), pp. 1174–1182.

[19] C. Rey, ed. *Superconductors in the power grid: materials and applications.* 1st ed. Elsevier, 2015.

[20] F. London and H. London. “The electromagnetic equations of the supraconductor”. In: *Proceedings of the Royal Society of London A* 149.866 (1935), pp. 71–88.

[21] V. I. Ginzburg. “On the theory of superconductivity”. In: *Zh. eksper. teor. Fiz.* 20 (1950), pp. 1064–1082.

[22] V. V. Schmidt. *The physics of superconductors. Introduction to fundamentals and applications.* Ed. by P. Müller and A. V. Ustinov. Springer, 2013.

[23] J. Bardeen, L. N. Cooper, and J. R. Schrieffer. “Microscopic theory of superconductivity”. In: *Phys. Rev.* 106.1 (1957), p. 162.

[24] J. Bardeen, L. N. Cooper, and J. R. Schrieffer. “Theory of superconductivity”. In: *Phys. Rev.* 108.5 (1957), p. 1175.

[25] R. Gross and A. Marx. *Applied superconductivity. Josephson effect and superconducting electronics.* Oct. 2015. URL: `https://www.wmi.badw.de/teaching/Lecturenotes/index.html`.

[26] F. Marsiglio and J. P. Carbotte. “Electron-phonon superconductivity”. In: *Superconductivity.* Springer, 2008, pp. 73–162.

[27] J. G. Bednorz and K. A. Müller. “Possible high T_c superconductivity in the Ba-La-Cu-O system”. In: *Zeitschrift für Physik B Condensed Matter* 64.2 (1986), pp. 189–193.

[28] E. O. Göbel and U. Siegner. *Quantum Metrology: Foundation of Units and Measurements.* 1st ed. John Wiley & Sons, 2015.

[29] J. Clarke and A. I. Braginski. *The SQUID handbook: Applications of SQUIDs and SQUID systems.* John Wiley & Sons, 2006.

[30] A. Barone and G. Paternò. *Physics and applications of the Josephson effect.* Vol. 1. John Wiley & Sons, 1982.

[31] B. D. Josephson. “Possible new effects in superconductive tunnelling”. In: *Physics Letters* 1.7 (1962), pp. 251–253.

[32] P. W. Anderson and J. M. Rowell. “Probable observation of the Josephson superconducting tunneling effect”. In: *Phys. Rev. Lett.* 10.6 (1963), p. 230.

[33] R. P. Feynman, R. B. Leighton, and M. Sands. “The Feynman lectures on physics; vol. I”. In: *Am. J. Phys* 33.9 (1965), pp. 750–752.

[34] C. A. Hamilton, C. J. Burroughs, and S. P. Benz. “Josephson voltage standard-a review”. In: *IEEE Trans. Appl. Supercond.* 7.2 (1997), pp. 3756–3761.

[35] S. Shapiro. “Josephson currents in superconducting tunneling: the effect of microwaves and other observations”. In: *Phys. Rev. Lett.* 11.2 (1963), p. 80.

[36] R. L. Kautz and F. L. Lloyd. “Precision of series-array Josephson voltage standards”. In: *Appl. Phys. Lett.* 51.24 (1987), pp. 2043–2045.

[37] J. Niemeyer et al. “High precision measurement of a possible resistive slope of Josephson array voltage steps”. In: *IEEE Electron Device Lett.* 7.1 (1986), pp. 44–46.

[38] J. Tsai, A. K. Jain, and J. E. Lukens. “High-precision test of the universality of the Josephson voltage-frequency relation”. In: *Phys. Rev. Lett.* 51.4 (1983), p. 316.

[39] P. J. Mohr, D. B. Newell, and B. N. Taylor. “CODATA recommended values of the fundamental physical constants: 2014”. In: *J. Phys. Chem. Ref. Data* 45.4 (2016), p. 043102.

[40] W. C. Stewart. “Current-voltage characteristics of Josephson junctions”. In: *Appl. Phys. Lett.* 12.8 (1968), pp. 277–280.

[41] D. E. McCumber. “Effect of ac impedance on dc voltage-current characteristics of superconductor weak-link junctions”. In: *J. Appl. Phys.* 39.7 (1968), pp. 3113–3118.

[42] R. L. Kautz. “Noise, chaos, and the Josephson voltage standard”. In: *Rep. Prog. Phys.* 59.8 (1996), p. 935.

[43] B. Jeckelmann and B. Jeanneret. “The application of the Josephson and quantum Hall effects in electrical metrology”. In: *Metrology and Fundamental Constants, Course CLXVI.* Ed. by T. W. Hänsch, S. Leschiutta, and A. J. Wallard. Vol. 166. IOS Press, 2007, pp. 135–179.

[44] B. F. Field, T. F. Finnegan, and J. Toots. “Volt maintenance at NBS via $2e/h$: a new definition of the NBS volt”. In: *Metrologia* 9.4 (1973), p. 155.

[45] B. Jeanneret and S. P. Benz. “Application of the Josephson effect in electrical metrology”. In: *The European Physical Journal Special Topics* 172.1 (2009), pp. 181–206.

[46] T. Endo, M. Koyanagi, and A. Nakamura. “High-accuracy Josephson potentiometer”. In: *IEEE Trans. Instrum. Meas.* 32.1 (1983), pp. 267–271.

[47] M. T. Levinsen et al. “An inverse ac Josephson effect voltage standard”. In: *Appl. Phys. Lett.* 31.11 (1977), pp. 776–778.

[48] J. Niemeyer, J. H. Hinken, and R. L. Kautz. “Microwave-induced constant-voltage steps at one volt from a series array of Josephson junctions”. In: *Appl. Phys. Lett.* 45.4 (1984), pp. 478–480.

[49] C. A. Hamilton et al. “A practical Josephson voltage standard at 1 V”. In: *IEEE Electron Device Lett.* 6.12 (1985), pp. 623–625.

[50] J. Niemeyer et al. “Stable Josephson reference voltages between 0.1 and 1.3 V for high-precision voltage standards”. In: *Appl. Phys. Lett.* 47.11 (1985), pp. 1222–1223.

[51] F. L. Lloyd et al. “A Josephson array voltage standard at 10 V”. In: *IEEE Electron Device Lett.* 8.10 (1987), pp. 449–450.

[52] A. M. Klushin et al. “High-temperature superconductor Josephson junctions for voltage standards”. In: *Phys. Solid State* 58.11 (Nov. 2016), pp. 2196–2202. DOI: `10.1134/S1063783416110184`.

[53] V. Lacquaniti and A. Sosso. “Josephson Junctions for Present and Next Generation Voltage Metrology”. In: *Modern Metrology Concerns*. InTech, 2012.

[54] C. A. Hamilton. “Josephson voltage standards”. In: *Rev. Sci. Instrum.* 71.10 (2000), pp. 3611–3623.

[55] R. L. Kautz. “Quasipotential and the stability of phase lock in nonhysteretic Josephson junctions”. In: *J. Appl. Phys.* 76.9 (1994), pp. 5538–5544.

[56] C. Noeldeke et al. “Experimental survey of chaos in the Josephson effect”. In: *J. Low Temp. Phys.* 64.3-4 (1986), pp. 235–268.

[57] J. Kohlmann and R. Behr. “Development of Josephson voltage standards”. In: *Superconductivity-Theory and Applications*. InTech, 2011.

[58] R. Behr et al. “Development and metrological applications of Josephson arrays at PTB”. In: *Meas. Sci. Technol.* 23.12 (2012), p. 124002.

[59] J. Kohlmann, R. Behr, and T. Funck. “Josephson voltage standards”. In: *Meas. Sci. Technol.* 14.8 (2003), p. 1216.

[60] S. P. Benz and C. A. Hamilton. “Application of the Josephson effect to voltage metrology”. In: *Proc. IEEE* 92.10 (2004), pp. 1617–1629.

[61] G. Boella et al. “Traceability of the 10 kΩ standard at IEN”. In: *IEEE Trans. Instrum. Meas.* 50.2 (2001), pp. 245–248.

[62] R. Behr and A. S. Katkov. “Final report on the key comparison EUROMET. BIPM. EM-K10. a: Comparison of Josephson array voltage standards by using a portable Josephson transfer standard”. In: *Metrologia* 42.1A (2005), p. 01005.

[63] K. Von Klitzing, G. Dorda, and M. Pepper. “New method for high-accuracy determination of the fine-structure constant based on quantized Hall resistance”. In: *Phys. Rev. Lett.* 45.6 (1980), p. 494.

[64] E. H. Hall. “On a new action of the magnet on electric currents”. In: *American Journal of Mathematics* 2.3 (1879), pp. 287–292.

[65] L. Callegaro. *Electrical impedance: principles, measurement, and applications.* CRC Press, 2012.

[66] R. E. Elmquist et al. “The ampere and electrical standards”. In: *J. Res. Nat. Inst. Stand. Technol.* 106.1 (2001), p. 65.

[67] B. Jeckelmann and B. Jeanneret. “The quantum Hall effect as an electrical resistance standard”. In: *Rep. Prog. Phys.* 64.12 (2001), p. 1603.

[68] J. Weis and K. Von Klitzing. “Metrology and microscopic picture of the integer quantum Hall effect”. In: *Philosophical Transactions of the Royal Society A* 369.1953 (2011), pp. 3954–3974.

[69] F. Delahaye et al. “Comparison of quantum Hall effect resistance standards of the PTB and the BIPM”. In: *Metrologia* 34.3 (1997), p. 211.

[70] D. V. Averin and K. K. Likharev. “Coulomb blockade of single-electron tunneling, and coherent oscillations in small tunnel junctions”. In: *J. Low Temp. Phys.* 62.3-4 (1986), pp. 345–373.

[71] T. A. Fulton and G. J. Dolan. “Observation of single-electron charging effects in small tunnel junctions”. In: *Phys. Rev. Lett.* 59.1 (1987), p. 109.

[72] F. Piquemal et al. “Single charge transport standards and quantum-metrological triangle experiments”. In: *Metrology and Fundamental Constants, Course CLXVI.* Ed. by T. W. Hänsch, S. Leschiutta, and A. J. Wallard. Vol. 166. IOS Press, 2007, pp. 181–210.

[73] N. Feltin and F. Piquemal. “Determination of the elementary charge and the quantum metrological triangle experiment”. In: *The European Physical Journal Special Topics* 172.1 (2009), pp. 267–296.

[74] F. Piquemal and G. Genevès. “Argument for a direct realization of the quantum metrological triangle”. In: *Metrologia* 37.3 (2000), p. 207.

[75] M. W. Keller, N. M. Zimmerman, and A. L. Eichenberger. “Uncertainty budget for the NIST electron counting capacitance standard, ECCS-1”. In: *Metrologia* 44.6 (2007), p. 505.

[76] B. N. Taylor and T. J. Witt. “New international electrical reference standards based on the Josephson and quantum Hall effects”. In: *Metrologia* 26.1 (1989), p. 47.

[77] CIPM. *Recommendation 1: Representation of the volt by means of the Josephson effect.* 1988. URL: `https://www.bipm.org/en/CIPM/db/1988/1/`.

[78] CIPM. *Recommendation 2: Representation of the ohm by means of the quantum Hall effect.* 1988. URL: `https://www.bipm.org/en/CIPM/db/1988/2/`.

[79] BIPM. *International System of Units revised in historic vote.* URL: `https://www.bipm.org/en/news/full-stories/2018-11-si-overhaul.html` (visited on 03/18/2019).

[80] M. J. T. Milton, R. Davis, and N. Fletcher. “Towards a new SI: a review of progress made since 2011”. In: *Metrologia* 51.3 (2014), R21.

[81] N. Fletcher et al. “Electrical units in the new SI: saying goodbye to the 1990 values”. In: *NCSLI Measure* 9.3 (2014), pp. 30–35.

[82] C. A. Hamilton, C. J. Burroughs, and R. L. Kautz. “Josephson D/A converter with fundamental accuracy”. In: *IEEE Trans. Instrum. Meas.* 44.2 (1995), pp. 223–225.

[83] R. Monaco. “Enhanced ac Josephson effect”. In: *J. Appl. Phys.* 68.2 (1990), pp. 679–687.

[84] S. Maggi. “Step width enhancement in a pulse-driven Josephson junction”. In: *J. Appl. Phys.* 79.10 (1996), pp. 7860–7863.

[85] S. P. Benz and C. A. Hamilton. “A pulse-driven programmable Josephson voltage standard”. In: *Appl. Phys. Lett.* 68.22 (1996), pp. 3171–3173.

[86] S. P. Benz, P. D. Dresselhaus, and C. J. Burroughs. “Nanotechnology for next generation Josephson voltage standards”. In: *IEEE Trans. Instrum. Meas.* 50.6 (2001), pp. 1513–1518.

[87] B. D. Inglis. “Standards for AC-DC transfer”. In: *Metrologia* 29.2 (1992), p. 191.

[88] F. L. Hermach. “Thermal converters as ac-dc transfer standards for current and voltage measurements at audio frequencies”. In: *J. Res. Nat. Bur. Stand.* 48.2 (1952), pp. 121–138.

[89] T. F. Wunsch et al. *Recent Advances in ac-dc Transfer Measurements Using Thin-film Thermal Converters.* Tech. rep. Sandia National Labs., Albuquerque, NM (US); Sandia National Labs., Livermore, CA (US), 2000.

[90] F. L. Hermach and E. S. Williams. "Thermal converters for audio-frequency voltage measurements of high accuracy". In: *IEEE Trans. Instrum. Meas.* 15.4 (1966), pp. 260–268.

[91] M. Klonz. "AC-DC transfer difference of the PTB multijunction thermal converter in the frequency range from 10 Hz to 100 kHz". In: *IEEE Trans. Instrum. Meas.* 1001.2 (1987), pp. 320–329.

[92] H. Dintner et al. "AC-DC-mV-transfer with highly sensitive thin-film multijunction thermal converters". In: *IEEE Trans. Instrum. Meas.* 42.2 (1993), pp. 612–614.

[93] Fluke Corporation. *792A AC/DC Transfer Standard.* URL: `https://us.flukecal.com/products/electrical-calibration/electrical-standards/792a-acdc-transfer-standard-0` (visited on 03/18/2019).

[94] H. A. Mageed et al. "Establishment and characterization of a traceable AC voltage source at NIS, Egypt". In: *Universities Power Engineering Conference, 2008. UPEC 2008. 43rd International.* IEEE. 2008, pp. 1–5.

[95] H. Fujiki, Y. Amagai, and H. Sasaki. "Development of thin-film multijunction thermal converters". In: *Synthesiology English edition* 8.3 (2015), pp. 113–132.

[96] L. Scarioni, M. Klonz, and E. Kebler. "Explanation for the AC–DC voltage transfer differences in thin-film multijunction thermal converters on silicon chips at high frequencies". In: *IEEE Trans. Instrum. Meas.* 56.2 (2007), pp. 567–570.

[97] T. E. Lipe and J. R. Kinard. "Quantum AC voltage standards". In: *IEEE Trans. Instrum. Meas.* 61.8 (2012), pp. 2160–2166.

[98] Y. Chong et al. "2.6-V high-resolution programmable Josephson voltage standard circuits using double-stacked $MoSi_2$-barrier junctions". In: *IEEE Trans. Instrum. Meas.* 54.2 (2005), pp. 616–619.

[99] F. Müller et al. "NbSi barrier junctions tuned for metrological applications up to 70 GHz: 20 V arrays for programmable Josephson voltage standards". In: *IEEE Trans. Appl. Supercond.* 23.3 (2013), pp. 1101005–1101005.

[100] H. Yamamori et al. "A 10 V programmable Josephson voltage standard circuit with a maximum output voltage of 20 V". In: *Supercond. Sci. Technol.* 21.10 (2008), p. 105007.

[101] Y. Chong, M. S. Kim, and K. T. Kim. "Fast and almost continuously programmable Josephson standard system with multiple microwave drive". In: *Precision Electromagnetic Measurements (CPEM 2016), 2016 Conference on.* 2016, p. 382.

[102] A. Rüfenacht, C. J. Burroughs, and S. P. Benz. "Precision sampling measurements using ac programmable Josephson voltage standards". In: *Rev. Sci. Instrum.* 79.4 (2008), p. 044704.

[103] C. J. Burroughs et al. "Error and transient analysis of stepwise-approximated sine waves generated by programmable Josephson voltage standards". In: *IEEE Trans. Instrum. Meas.* 57.7 (2008), pp. 1322–1329.

[104] C. J. Burroughs et al. "Systematic error analysis of stepwise-approximated AC waveforms generated by programmable Josephson voltage standards". In: *IEEE Trans. Instrum. Meas.* 58.4 (2009), pp. 761–767.

[105] C. J. Burroughs et al. "Method for ensuring accurate ac waveforms with programmable Josephson voltage standards". In: *IEEE Trans. Instrum. Meas.* 62.6 (2013), pp. 1627–1633.

[106] J. M. Williams et al. "Achieving sub-100-ns switching of programmable Josephson arrays". In: *IEEE Trans. Instrum. Meas.* 56.2 (2007), pp. 651–654.

[107] A. Rüfenacht, N. E. Flowers-Jacobs, and S. P. Benz. "Impact of the latest generation of Josephson voltage standards in ac and dc electric metrology". In: *Metrologia* 55.5 (2018), S152.

[108] C. J. Burroughs et al. "Development of a 60 Hz power standard using SNS programmable Josephson voltage standards". In: *IEEE Trans. Instrum. Meas.* 56.2 (2007), pp. 289–294.

[109] L. Palafox et al. "The Josephson-effect-based primary AC power standard at the PTB: Progress report". In: *IEEE Trans. Instrum. Meas.* 58.4 (2009), pp. 1049–1053.

[110] S. Djordjevic et al. "Direct comparison between a programmable and a conventional Josephson voltage standard at the level of 10 V". In: *Metrologia* 45.4 (2008), p. 429.

[111] Y. Tang et al. "A 10 V programmable Josephson voltage standard and its applications for voltage metrology". In: *Metrologia* 49.6 (2012), p. 635.

[112] T. Yamada et al. "Single-chip 10-V programmable Josephson voltage standard system based on a refrigerator and its precision evaluation". In: *IEEE Trans. Appl. Supercond.* 20.1 (2010), pp. 21–25.

[113] S. Solve et al. "Direct comparison of two NIST PJVS systems at 10 V". In: *Metrologia* 50.5 (2013), p. 441.

[114] A. Rüfenacht et al. "Automated direct comparison of two cryocooled 10 volt programmable Josephson voltage standards". In: *Metrologia* (2018).

[115] M. Maruyama et al. “Development of zener calibration system using 10 V programmable Josephson voltage standard at NMIJ”. In: *Precision Electromagnetic Measurements (CPEM 2014), 2014 Conference on*. IEEE. 2014, pp. 260–261.

[116] H. E. van den Brom et al. “Voltage linearity measurements using a binary Josephson system”. In: *Meas. Sci. Technol.* 18.11 (2007), p. 3316.

[117] M. S. Kim et al. “Voltage linearity evaluation for a high-speed digitizer adopted to a quantum sampling voltmeter”. In: *Precision Electromagnetic Measurements (CPEM 2016), 2016 Conference on*. IEEE. 2016, pp. 1–2.

[118] W. G. Kurten et al. “Characterization of a high-resolution analog-to-digital converter with a Josephson AC voltage source”. In: *IEEE Trans. Instrum. Meas.* 54.2 (2005), pp. 649–652. DOI: `10.1109/TIM.2004.843064`.

[119] F. Overney et al. “Characterization of metrological grade analog-to-digital converters using a programmable Josephson voltage standard”. In: *IEEE Trans. Instrum. Meas.* 60.7 (2011), pp. 2172–2177.

[120] T. Funck, R. Behr, and M. Klonz. “Fast reversed dc measurements on thermal converters using a SINIS Josephson junction array”. In: *IEEE Trans. Instrum. Meas.* 50.2 (2001), pp. 322–325.

[121] J. Lee et al. “Programmable Josephson arrays for impedance measurements”. In: *IEEE Trans. Instrum. Meas.* 60.7 (2011), pp. 2596–2601.

[122] T. Hagen, L. Palafox, and R. Behr. “A Josephson Impedance Bridge Based on Programmable Josephson Voltage Standards”. In: *IEEE Trans. Instrum. Meas.* 66.6 (2017), pp. 1539–1545.

[123] C. A. Sanchez et al. “A determination of Planck’s constant using the NRC watt balance”. In: *Metrologia* 51.2 (2014), S5.

[124] S. Schlamminger et al. “Determination of the Planck constant using a watt balance with a superconducting magnet system at the National Institute of Standards and Technology”. In: *Metrologia* 51.2 (2014), S15.

[125] L. Devoille et al. “Quantum metrological triangle experiment at LNE: measurements on a three-junction R-pump using a 20 000: 1 winding ratio cryogenic current comparator”. In: *Meas. Sci. Technol.* 23.12 (2012), p. 124011.

[126] R. Behr et al. “Direct comparison of Josephson waveforms using an AC quantum voltmeter”. In: *IEEE Trans. Instrum. Meas.* 56.2 (2007), pp. 235–238.

[127] J. Lee et al. “An ac quantum voltmeter based on a 10 V programmable Josephson array”. In: *Metrologia* 50.6 (2013), p. 612.

[128] M. Schubert et al. "An AC Josephson voltage standard up to the kilohertz range tested in a calibration laboratory". In: *IEEE Trans. Instrum. Meas.* 64.6 (2015), pp. 1620–1626.

[129] A. Rüfenacht et al. "Differential sampling measurement of a 7 V RMS sine wave with a programmable Josephson voltage standard". In: *IEEE Trans. Instrum. Meas.* 62.6 (2013), pp. 1587–1593.

[130] J. Lee et al. "A quantum voltmeter for precision AC measurements". In: *Precision Electromagnetic Measurements (CPEM 2014), 2014 Conference on.* IEEE. 2014, pp. 732–733.

[131] J. Lee et al. "From AC quantum voltmeter to quantum calibrator". In: *Precision Electromagnetic Measurements (CPEM 2016), 2016 Conference on.* IEEE. 2016, pp. 1–2.

[132] W. G. K. Ihlenfeld and R. P. Landim. "Investigations on extending the frequency range of PJVS based AC voltage calibrations by coherent subsampling". In: *2016 Conference on Precision Electromagnetic Measurements (CPEM 2016).* 2016, pp. 1–2. DOI: `10.1109/CPEM.2016.7539732`.

[133] R. Behr et al. "Frequency Range Extension of the AC Quantum Voltmeter". In: *2018 Conference on Precision Electromagnetic Measurements (CPEM 2018).* 2018, pp. 1–2. DOI: `10.1109/CPEM.2018.8501156`.

[134] Supracon AG. *AC Quantum Voltmeter.* 2016. URL: `http://www.supracon.com/en/ac_quantum_voltmeter.html` (visited on 03/18/2019).

[135] National Institute of Standards and Technology. *SRI 6000 Series Programmable Josephson Voltage Standard (PJVS).* Feb. 14, 2019. URL: `https://www.nist.gov/sri/standard-reference-instruments/sri-6000-series-programmable-josephson-voltage-standard-pjvs` (visited on 03/18/2019).

[136] M. Schubert et al. "A dry-cooled AC quantum voltmeter". In: *Supercond. Sci. Technol.* 29.10 (2016), p. 105014.

[137] S. P. Benz et al. "Stable 1 volt programmable voltage standard". In: *Appl. Phys. Lett.* 71.13 (1997), pp. 1866–1868.

[138] B. Baek, P. D. Dresselhaus, and S. P. Benz. "Co-Sputtered Amorphous $\mathrm{Nb_xSi_{1\text{-}x}}$ Barriers for Josephson-Junction Circuits". In: *IEEE Trans. Appl. Supercond.* 16.4 (2006), pp. 1966–1970.

[139] A. E. Fox et al. "Junction yield analysis for 10 V programmable Josephson voltage standard devices". In: *IEEE Trans. Appl. Supercond.* 25.3 (2015), pp. 1–5.

[140] P. D. Dresselhaus et al. "10 volt programmable Josephson voltage standard circuits using NbSi-barrier junctions". In: *IEEE Trans. Appl. Supercond.* 21.3 (2011), pp. 693–696.

[141] H. Schulze et al. “SINIS Josephson junctions for programmable Josephson voltage standard circuits”. In: *IEEE Trans. Appl. Supercond.* 9.2 (1999), pp. 4241–4244.

[142] H. Schulze et al. “Design and fabrication of 10 V SINIS Josephson arrays for programmable voltage standards”. In: *Supercond. Sci. Technol.* 13.9 (2000), p. 1293.

[143] F. Müller et al. “Improved 10 V SINIS series arrays for applications in AC voltage metrology”. In: *IEEE Trans. Appl. Supercond.* 17.2 (2007), pp. 649–652.

[144] F. Müller et al. “1 V and 10 V SNS programmable voltage standards for 70 GHz”. In: *IEEE Trans. Appl. Supercond.* 19.3 (2009), pp. 981–986.

[145] H. Yamamori, M. Ishizaki, and A. Sasaki H.and Shoji. “Operating Margins of a 10 V Programmable Josephson Voltage Standard Circuit Using NbN/TiN$_x$/NbN/TiN$_x$/NbN Double-Junction Stacks”. In: *IEEE Trans. Appl. Supercond.* 17.2 (2007), pp. 858–863.

[146] V. Lacquaniti et al. “Overdamped Nb/Al–AlO$_x$/Nb Josephson junctions”. In: *Appl. Phys. Lett.* 86.4 (2005), p. 042501.

[147] V. Lacquaniti et al. “Nb/Al–AlO$_x$/Nb superconducting heterostructures: A promising class of self-shunted Josephson junctions”. In: *J. Appl. Phys.* 108.9 (2010), p. 093701.

[148] V. Lacquaniti et al. “1 V programmable voltage standards based on SNIS Josephson junction series arrays”. In: *Supercond. Sci. Technol.* 24.4 (2011), p. 045004.

[149] V. Lacquaniti et al. “Engineering overdamped niobium-based Josephson junctions for operation above 4.2 K”. In: *IEEE Trans. Appl. Supercond.* 19.3 (2009), pp. 234–237.

[150] A. Sosso et al. “Cryocooler operation of SNIS Josephson arrays for ac voltage standards”. In: *Journal of Physics: Conference Series.* Vol. 507. 4. IOP Publishing. 2014, p. 042040.

[151] R. L. Kautz. “Shapiro steps in large-area metallic-barrier Josephson junctions”. In: *J. Appl. Phys.* 78.9 (1995), pp. 5811–5819.

[152] S. Pavan, R. Schreier, and G. C. Temes. *Understanding delta-sigma data converters.* John Wiley & Sons, 2017.

[153] H. E. van den Brom and E. Houtzager. “Expanding the operating range of the pulse-driven AC Josephson voltage standard”. In: *Precision Electromagnetic Measurements (CPEM), 2012 Conference on.* IEEE. 2012, pp. 42–43.

[154] J. A. Brevik et al. “Radio-Frequency Waveform Synthesis with the Josephson Arbitrary Waveform Synthesizer”. In: *2018 Conference on Precision Electromagnetic Measurements (CPEM 2018)*. 2018, pp. 1–2. DOI: `10.1109/CPEM.2018.8501023`.

[155] S. P. Benz et al. “Pulse-driven Josephson digital/analog converter”. In: *IEEE Trans. Appl. Supercond.* 8.2 (1998), pp. 42–47.

[156] S. P. Benz et al. “AC and DC bipolar voltage source using quantized pulses”. In: *IEEE Trans. Instrum. Meas.* 48.2 (1999), pp. 266–269.

[157] S. P. Benz et al. “Operating conditions for a pulse-quantized AC and DC bipolar voltage source”. In: *IEEE Trans. Appl. Supercond.* 9.2 (1999), pp. 3306–3309.

[158] H. E. van den Brom et al. “Bipolar pulse-drive electronics for a Josephson arbitrary waveform synthesizer”. In: *IEEE Trans. Instrum. Meas.* 57.2 (2008), pp. 428–431.

[159] O. F. Kieler et al. “Towards a 1 V Josephson Arbitrary Waveform Synthesizer”. In: *IEEE Trans. Appl. Supercond.* 25.3 (June 2015), pp. 1–5. DOI: `10.1109/TASC.2014.2366916`.

[160] S. P. Benz et al. “One-volt Josephson arbitrary waveform synthesizer”. In: *IEEE Trans. Appl. Supercond.* 25.1 (2015), pp. 1–8.

[161] S. P. Benz et al. “Performance Improvements for the NIST 1 V Josephson Arbitrary Waveform Synthesizer”. In: *IEEE Trans. Appl. Supercond.* 25.3 (2015), pp. 1–5. DOI: `10.1109/TASC.2014.2364137`.

[162] N. E. Flowers-Jacobs et al. “Three Volt Pulse-Driven Josephson Arbitrary Waveform Synthesizer”. In: *2018 Conference on Precision Electromagnetic Measurements (CPEM 2018)*. IEEE. 2018, pp. 1–2.

[163] O. F. Kieler et al. “Precision comparison of sine waveforms with pulse-driven Josephson arrays”. In: *IEEE Trans. Appl. Supercond.* 23.3 (2013), pp. 1301404–1301404.

[164] N. E. Flowers-Jacobs et al. “2 Volt pulse-driven Josephson arbitrary waveform synthesizer”. In: *Precision Electromagnetic Measurements (CPEM 2016), 2016 Conference on*. IEEE. 2016, pp. 1–2.

[165] B. Jeanneret et al. “High precision comparison between a programmable and a pulse-driven Josephson voltage standard”. In: *Metrologia* 48.5 (2011), p. 311.

[166] R. Behr et al. “Direct comparison of a 1 V Josephson arbitrary waveform synthesizer and an ac quantum voltmeter”. In: *Metrologia* 52.4 (2015), p. 528.

[167] R. Behr et al. “Combining Josephson systems for spectrally pure AC waveforms with large amplitudes”. In: *IEEE Trans. Instrum. Meas.* 62.6 (2013), pp. 1634–1639.

[168] S. P. Benz et al. “An AC Josephson Voltage Standard for AC-DC Transfer-Standard Measurements”. In: *IEEE Trans. Instrum. Meas.* 56.2 (2007), pp. 239–243. DOI: `10.1109/TIM.2007.891153`.

[169] P. S. Filipski, H. E. van den Brom, and E. Houtzager. “International comparison of quantum AC voltage standards for frequencies up to 100 kHz”. In: *Measurement* 45.9 (2012), pp. 2218–2225.

[170] O. Seron et al. “Precision AC–DC transfer measurements with a Josephson waveform synthesizer and a buffer amplifier”. In: *IEEE Trans. Instrum. Meas.* 61.1 (2012), pp. 198–204.

[171] T. E. Lipe et al. “Thermal voltage converter calibrations using a quantum AC standard”. In: *Metrologia* 45.3 (2008), p. 275.

[172] P. S. Filipski et al. “Experimental determination of the voltage lead error in an ac Josephson voltage standard”. In: *IEEE Trans. Instrum. Meas.* 60.7 (2011), pp. 2387–2392.

[173] L. Palafox et al. “First metrological applications of the PTB 1 V Josephson arbitrary waveform synthesizer”. In: *Precision Electromagnetic Measurements (CPEM 2016), 2016 Conference on.* IEEE. 2016, pp. 1–2.

[174] F. Overney et al. “Josephson-based full digital bridge for high-accuracy impedance comparisons”. In: *Metrologia* 53.4 (2016), p. 1045.

[175] S. Bauer et al. “A novel two-terminal-pair pulse-driven Josephson impedance bridge linking a 10 nF capacitance standard to the quantized Hall resistance”. In: *Metrologia* 54.2 (2017), p. 152.

[176] R. Behr, O. Kieler, and B. Schumacher. “A Precision Microvolt-Synthesizer Based on a Pulse-Driven Josephson Voltage Standard”. In: *IEEE Trans. Instrum. Meas.* 66.6 (2017), pp. 1385–1390.

[177] R. C. Toonen and S. P. Benz. “Nonlinear behavior of electronic components characterized with precision multitones from a Josephson arbitrary waveform synthesizer”. In: *IEEE Trans. Appl. Supercond.* 19.3 (2009), pp. 715–718.

[178] S. P. Benz et al. “Improvements in the NIST Johnson noise thermometry system”. In: *IEEE Trans. Instrum. Meas.* 58.4 (2009), pp. 884–890.

[179] S. P. Benz et al. “An electronic measurement of the Boltzmann constant”. In: *Metrologia* 48.3 (2011), p. 142.

[180] D. Hagedorn et al. “Modified fabrication of planar sub-µm superconductor–normal metal–superconductor Josephson junctions for use in a Josephson arbitrary waveform synthesizer”. In: *Supercond. Sci. Technol.* 19.4 (2006), p. 294.

[181] J. Kohlmann et al. “Josephson series arrays for programmable 10-V SINIS Josephson voltage standards and for Josephson arbitrary waveform synthesizers based on SNS junctions”. In: *IEEE Trans. Instrum. Meas.* 56.2 (2007), pp. 472–475.

[182] S. P. Benz, C. J. Burroughs, and P. D. Dresselhaus. “AC coupling technique for Josephson waveform synthesis”. In: *IEEE Trans. Appl. Supercond.* 11.1 (2001), pp. 612–616.

[183] J. Kohlmann et al. “Josephson series arrays with NbSi barrier for ac voltage standards”. In: *Precision Electromagnetic Measurements (CPEM 2014), 2014 Conference on.* IEEE. 2014, pp. 466–467.

[184] H. E. van den Brom et al. “Synthesis of sinusoidal signals with a Josephson arbitrary waveform synthesizer”. In: *Supercond. Sci. Technol.* 20.5 (2007), p. 413.

[185] P. D. Dresselhaus et al. “Stacked SNS Josephson junction arrays for quantum voltage standards”. In: *IEEE Trans. Appl. Supercond.* 13.2 (2003), pp. 930–933.

[186] N. Hadacek et al. “Fabrication and measurement of tall stacked arrays of SNS Josephson junctions”. In: *IEEE Trans. Appl. Supercond.* 15.2 (2005), pp. 110–113.

[187] O. F. Kieler et al. “SNS Josephson junction series arrays for the Josephson arbitrary waveform synthesizer”. In: *IEEE Trans. Appl. Supercond.* 17.2 (2007), pp. 187–190.

[188] O. F. Kieler, J. Kohlmann, and F. Müller. “Improved design of superconductor/normal conductor/superconductor Josephson junction series arrays for an ac Josephson voltage standard”. In: *Supercond. Sci. Technol.* 20.11 (2007), S318.

[189] K. Zhou, J. Qu, and S. P. Benz. “Zero-compensation method and reduced inductive voltage error for the AC Josephson voltage standard”. In: *IEEE Trans. Appl. Supercond.* 25.5 (2015), pp. 1–6.

[190] J. A. Brevik et al. “Josephson Arbitrary Waveform Synthesis With Multilevel Pulse Biasing”. In: *IEEE Trans. Appl. Supercond.* 27.3 (2017), pp. 1–7.

[191] P. S. Filipski et al. “Correction of systematic errors due to the voltage leads in an ac Josephson voltage standard”. In: *IEEE Trans. Instrum. Meas.* 58.4 (2009), pp. 853–858.

[192] H. E. van den Brom and E. Houtzager. “Voltage lead corrections for a pulse-driven ac Josephson voltage standard”. In: *Meas. Sci. Technol.* 23.12 (2012), p. 124007.

[193] H. E. van den Brom et al. “AC–DC Calibrations With a Pulse-Driven AC Josephson Voltage Standard Operated in a Small Cryostat”. In: *IEEE Trans. Instrum. Meas.* 66.6 (2017), pp. 1391–1396.

[194] H. E. van den Brom, D. Zhao, and E. Houtzager. “Voltage lead errors in an AC Josephson voltage standard: explanation in terms of standing waves”. In: *Precision Electromagnetic Measurements (CPEM 2016), 2016 Conference on.* IEEE. 2016, pp. 1–2.

[195] D. Zhao, H. E. van den Brom, and E. Houtzager. “Mitigating voltage lead errors of an AC Josephson voltage standard by impedance matching”. In: *Meas. Sci. Technol.* 28.9 (2017), p. 095004.

[196] J. M. Williams et al. “The simulation and measurement of the response of Josephson junctions to optoelectronically generated short pulses”. In: *Supercond. Sci. Technol.* 17.6 (2004), p. 815.

[197] J. Ireland et al. “An Optoelectronic Pulse Drive for Quantum Voltage Synthesizer”. In: *IEEE Trans. Instrum. Meas.* (2018), pp. 1–6. DOI: `10.1109/TIM.2018.2877562`.

[198] J. Ireland et al. “Josephson Arbitrary Waveform System with Optoelectronic Drive”. In: *Superconductive Electronics Conference (ISEC), 2017 16th International.* IEEE. 2017, pp. 1–4.

[199] C. Urano et al. “Operation of a Josephson arbitrary waveform synthesizer with optical data input”. In: *Supercond. Sci. Technol.* 22.11 (2009), p. 114012.

[200] E. Bardalen et al. “Packaging of fiber-coupled module for Josephson junction array voltage standards”. In: *Precision Electromagnetic Measurements (CPEM 2016), 2016 Conference on.* IEEE. 2016, pp. 1–2.

[201] R. G. Ross Jr. “Refrigeration Systems for Achieving Cryogenic Temperatures”. In: *Low Temperature Materials and Mechanisms.* CRC Press, 2016, pp. 127–200.

[202] M. N. Jirmanus. “Introduction to laboratory cryogenics”. In: *Janis Research Company, MA, EUA* (1990).

[203] G. Ventura and L. Risegari. *The art of cryogenics: low-temperature experimental techniques.* Elsevier, 2010.

[204] R. Radebaugh. “Cryocoolers: the state of the art and recent developments”. In: *J. Phys.: Condens. Matter* 21.16 (2009), p. 164219.

[205] G. Walker. *Cryocoolers, part I: Fundamentals and part 2. Applications.* 1983.

[206] W. Shen, M. Coffey, and W. McGhee. “Development of 9.5 T NbTi cryogen-free magnet”. In: *IEEE Trans. Appl. Supercond.* 11.1 (2001), pp. 2619–2622.

[207] S. W. Van Sciver. *Helium cryogenics.* 2nd ed. Springer, 2012.

[208] J. G. Weisend and J. G. Weisend. *Handbook of cryogenic engineering.* Vol. 325. Taylor & Francis Philadelphia, PA, 1998.

[209] Sumitomo Heavy Industries, Ltd. *Cryocoolers.* Nov. 2018. URL: `http://www.shi.co.jp/english/products/precision/cold/index.html` (visited on 03/18/2019).

[210] R. Radebaugh. “A review of pulse tube refrigeration”. In: *Advances in Cryogenic Engineering.* Springer, 1990, pp. 1191–1205.

[211] A. T. A. M. De Waele. “Basic operation of cryocoolers and related thermal machines”. In: *J. Low Temp. Phys.* 164.5-6 (2011), p. 179.

[212] L. Trevisani, F. Negrini, and M. Fabbri. *Studi teorici e sperimentali sull’utilizzo di materiali magnetici nello scambiatore di calore di un cryocooler Gifford-McMahon.* Tech. rep. Università degli Studi di Bologna - Dipartimento di Ingegneria Elettrica, June 2002.

[213] G. Thummes et al. “Convective heat losses in pulse tube coolers: effect of pulse tube inclination”. In: *Cryocoolers 9.* Springer, 1997, pp. 393–402.

[214] Cryomech, Inc. *Cryorefrigerators.* 2019. URL: `http://www.cryomech.com/cryorefrigerators/` (visited on 03/18/2019).

[215] J. D. de Aguilar et al. *Good Practice Guide on the operation of AC quantum voltage standards.* 2018.

[216] Lake Shore Cryotronics, Inc. *Cryogenic Temperature Sensors.* 2019. URL: `https://www.lakeshore.com/Products/Cryogenic-Temperature-Sensors/Pages/default.aspx` (visited on 03/18/2019).

[217] C. V. Madhusudana and F. F. Ling. *Thermal contact conductance.* Springer, 1996.

[218] J. G. Hust. “Thermal anchoring of wires in cryogenic apparatus”. In: *Rev. Sci. Instrum.* 41.5 (1970), pp. 622–624.

[219] A. Sosso and P. Durandetto. “Experimental analysis of the thermal behavior of a GM cryocooler based on linear system theory”. In: *Int. J. Refrig* 92 (2018), pp. 125–132. DOI: `https://doi.org/10.1016/j.ijrefrig.2018.04.016`.

[220] T. I. Mulcahey, M. G. Pathak, and S. M. Ghiaasiaan. “The effect of flow pulsation on drag and heat transfer in an array of heated square cylinders”. In: *Int. J. Therm. Sci.* 64 (2013), pp. 105–120.

[221] I. Catarino, D. Martins, and R. Sudiwala. “Materials for damping the PTC-induced thermal fluctuations of the cold-head”. In: *IOP Conference Series: Materials Science and Engineering*. Vol. 102. 1. IOP Publishing. 2015, p. 012014.

[222] D. Snow et al. “Apparatus and methods for improving vibration isolation, thermal dampening, and optical access in cryogenic refrigerators”. US8516834B2. 2010.

[223] G. Dubuis, X. He, and I. Božović. “Sub-millikelvin stabilization of a closed cycle cryocooler”. In: *Rev. Sci. Instrum.* 85.10 (2014), p. 103902.

[224] Y. Hasegawa et al. “High-precision temperature control and stabilization using a cryocooler”. In: *Rev. Sci. Instrum.* 81.9 (2010), p. 094901.

[225] Cryomech, Inc. *Temperature Oscillation Damping Pot.* 2019. URL: `https://www.cryomech.com/articles/temperature-oscillation-damping-pot/` (visited on 03/18/2019).

[226] R. J. Webber and J. Delmas. “Cool-down acceleration of GM cryocoolers with thermal oscillations passively damped by helium”. In: *IOP Conference Series: Materials Science and Engineering*. Vol. 101. 1. IOP Publishing. 2015, p. 012137.

[227] Y. P. Banjare, R. K. Sahoo, and S. K. Sarangi. “CFD simulation of a Gifford-McMahon type pulse tube refrigerator”. In: *Int. J. Therm. Sci.* 48.12 (2009), pp. 2280–2287.

[228] B. J. Huang and M. D. Chuang. “System design of orifice pulse-tube refrigerator using linear flow network analysis”. In: *Cryogenics* 36.11 (1996), pp. 889–902.

[229] K. Kim et al. “Numerical analysis of different valve effects on the cooling performance of a two-stage GM type pulse tube cryocooler”. In: *Int. J. Refrig* 77 (2017), pp. 1–10.

[230] V. Székely and T. Van Bien. “Fine structure of heat flow path in semiconductor devices: a measurement and identification method”. In: *Solid-State Electron.* 31.9 (1988), pp. 1363–1368.

[231] D. G. Luenberger. *Introduction to Dynamic Systems, Theory, Models, and Applications.* Ed. by J. W.
bibinitperiod Sons. 1979.

[232] Oerlikon Leybold Vacuum. *Coolpower 4.2 1.0 Watt Cold Head at 4.2K.* URL: `https://www.tu-chemnitz.de/physik/ION/Technology/cold%20heads/Oerlikon%20Coolpower%204.2GM%20-%201%20W.pdf` (visited on 05/22/2019).

[233] Apiezon. *Apiezon N Grease.* URL: `https://www.apiezon.com/products/vacuum-greases/n-grease` (visited on 03/18/2019).

[234] Lake Shore Cryotronics, Inc. *Model 350 Cryogenic Temperature Controller.* 2019. URL: `https://www.lakeshore.com/products/Cryogenic-Temperature-Controllers/Model-350/Pages/Overview.aspx` (visited on 03/18/2019).

[235] Keysight Technologies. *33250A Function / Arbitrary Waveform Generator, 80 MHz.* 2019. URL: `https://www.keysight.com/en/pd-1000000803%3Aepsg%3Apro-pn-33250A/function-arbitrary-waveform-generator-80-mhz?cc=IT&lc=ita` (visited on 03/18/2019).

[236] Tektronix, Inc. *Keithley Precision DC and AC+DC Low Noise Current Sources.* 2019. URL: `https://www.tek.com/keithley-low-level-sensitive-and-specialty-instruments/keithley-ultra-sensitive-current-sources-seri` (visited on 03/18/2019).

[237] SRS - Standford Research Systems. *SR560 – Low-noise voltage preamplifier.* URL: `https://www.thinksrs.com/products/sr560.html` (visited on 03/18/2019).

[238] Keysight Technologies. *6634B 100 Watt System Power Supply, 100V, 1A.* 2019. URL: `https://www.keysight.com/en/pd-838600-pn-6634B/100-watt-system-power-supply-100v-1a?cc=IT&lc=ita&lsrch=true&searchT=6634B` (visited on 03/18/2019).

[239] Teledyne LeCroy. *HDO6034A.* 2019. URL: `http://teledynelecroy.com/oscilloscope/hdo6000a-high-definition-oscilloscopes/hdo6034a` (visited on 03/18/2019).

[240] Am Scientific Instruments. *7265 Dual Phase DSP Lock-in Amplifier.* 2015. URL: `https://www.ameteksi.com/products/lock-in-amplifiers/7265-dual-phase-lock-in-amplifier` (visited on 03/18/2019).

[241] Oerlikon Leybold Vacuum. *Coolpower 4.2 One Watt Performance Data.* URL: `https://www.tu-chemnitz.de/physik/ION/Technology/cold%20heads/Oerlikon%20Load%20Map%20&%20Lay%20out%20-%201%20Watt.pdf` (visited on 03/18/2019).

[242] P. Durandetto et al. “Thermal Performances of an Improved Package for Cryocooled Josephson Standards”. In: *IEEE Trans. Compon. Packag. Manuf. Technol.* (2019), pp. 1–1. DOI: `10.1109/TCPMT.2019.2901297`.

[243] P. Durandetto and A. Sosso. “A modular and customizable open-source package for quantum voltage standards operation and control”. In: *PLOS ONE* 13.12 (2018). DOI: `10.1371/journal.pone.0209246`.

[244] P. Durandetto and A. Sosso. “Open-Source Package for PJVS Testing and Calibration”. In: *2018 Conference on Precision Electromagnetic Measurements (CPEM 2018)*. 2018, pp. 1–2. DOI: `10.1109/CPEM.2018.8501187`.

[245] P. Durandetto and A. Sosso. “Non-Conventional PJVS Exploiting First and Second Steps to Reduce Junctions and Bias Lines”. In: *IEEE Trans. Instrum. Meas.* (2019), pp. 1–1. ISSN: 0018-9456. DOI: `10.1109/TIM.2019.2913717`.

[246] F. Müller et al. “Microwave design and performance of PTB 10 V circuits for the programmable Josephson voltage standard”. In: *World Journal of Condensed Matter Physics* 4.03 (2014), p. 107.

[247] Y. Tang et al. “Cryocooled primary voltage standard system”. In: *IEEE Trans. Instrum. Meas.* 46.2 (1997), pp. 256–259.

[248] E. T. Swartz and R. O. Pohl. “Thermal boundary resistance”. In: *Rev. Mod. Phys.* 61 (3 1989), pp. 605–668. DOI: `10.1103/RevModPhys.61.605`. URL: `https://link.aps.org/doi/10.1103/RevModPhys.61.605`.

[249] J. Ekin. *Experimental techniques for low-temperature measurements: cryostat design, material properties and superconductor critical-current testing.* Oxford university press, 2006.

[250] H. Takahashi et al. “Heat transfer analysis of a programmable Josephson voltage standard chip operated with a mechanical cooler”. In: *Physica C: Superconductivity and its Applications* 518 (2015), pp. 89–95.

[251] R. Kirschman, W. Sokolowski, and E. Kolawa. “Die Attachment for -120 °C to +20 °C Thermal Cycling of Microelectronics for Future Mars Rovers - An Overview”. In: *J. Electron. Packag.* 123.2 (2001), pp. 105–111.

[252] I. Savija et al. “Review of thermal conductance models for joints incorporating enhancement materials”. In: *J. Thermophys. Heat Transfer* 17.1 (2003), pp. 43–52.

[253] M. Deutsch. “Thermal conductance in screw-fastened joints at helium temperatures”. In: *Cryogenics* 19.5 (1979), pp. 273–274. DOI: `https://doi.org/10.1016/0011-2275(79)90141-3`.

[254] A. Dillon et al. “Thermal interface material characterization for cryogenic electronic packaging solutions”. In: *IOP Conference Series: Materials Science and Engineering*. Vol. 278. 1. IOP Publishing. 2017, p. 012054.

[255] A. Sosso et al. “Temperature stability of SNIS Josephson arrays between 4.2 K and critical temperature in cryocooler”. In: *IEEE Trans. Appl. Supercond.* 25.3 (2015), pp. 1–4.

[256] A. Sosso et al. “Cryogen-free operation of SNIS for ac quantum voltage standards”. In: *IEEE Trans. Appl. Supercond.* 26.3 (2016), pp. 1–3.

[257] B. Trinchera et al. "On the synthesis of stepwise quantum waves using a SNIS programmable Josephson array in a cryocooler". In: *IEEE Trans. Appl. Supercond.* 27.4 (2017), pp. 1–5.

[258] Indium Corporation. *Heat-Spring.* 2019. URL: `http://www.indium.com/thermal-interface-materials/heat-spring/#products` (visited on 03/18/2019).

[259] Tektronix, Inc. *Keithley Ultra-low Voltage Measurements.* 2019. URL: `https://www.tek.com/keithley-low-level-sensitive-and-specialty-instruments/keithley-nanovoltmeter-model-2182a` (visited on 03/18/2019).

[260] Tektronix, Inc. *Model 220 Programmable Current Source Instruction Manual Rev. H Manual.* 2019. URL: `https://www.tek.com/manual/model-220-programmable-current-source-instruction-manual-rev-h` (visited on 03/18/2019).

[261] Tektronix, Inc. *Keithley Model 181 Digital Nanovoltmeter Operator's Manual 32421A Manual.* 2019. URL: `https://www.tek.com/manual/keithley-model-181-digital-nanovoltmeter-operators-manual-32421a` (visited on 03/18/2019).

[262] L. Howe et al. "Cryogen-free operation of 10 V programmable Josephson voltage standards". In: *IEEE Trans. Appl. Supercond.* 23.3 (2013), pp. 1300605–1300605.

[263] M. Asheghi et al. "Thermal conduction in doped single-crystal silicon films". In: *J. Appl. Phys.* 91.8 (2002), pp. 5079–5088.

[264] M. Kreitman and J. Callahan. "Thermal conductivity of Apiezon N grease at liquid helium temperatures". In: *Cryogenics* 10.2 (1970), pp. 155–159.

[265] R. Corruccini and J. Gniewek. *Thermal expansion of technical solids at low temperatures: a compilation from the literature. National Bureau of Standards Monograph 29.* Washington D.C.: US. Gov. Printing Office, May 19, 1961.

[266] C. Swenson. "Properties of Indium and Thallium at low temperatures". In: *Phys. Rev.* 100.6 (1955), p. 1607.

[267] N. Simon. *Cryogenic properties of inorganic insulation materials for ITER magnets: a review.* Tech. rep. National Institute of Standards and Technology, 1994.

[268] GitHub, ed. *PJVS-driving-tool.* 2019. URL: `https://github.com/pdurandetto/PJVS-driving-tool`.

[269] EURAMET e.V. *"Waveform metrology based on spectrally pure Josephson voltages"*. 2019. URL: `https://www.euramet.org/research-innovation/search-research-projects/details/?eurametCtcp_project_show%255Bproject%255D=1435` (visited on 03/18/2019).

[270] EURAMET e.V. *"Traceability routes for electrical power quality measurements"*. 2019. URL: `https://www.euramet.org/research-innovation/search-research-projects/details/?eurametCtcp_project_show%5Bproject%5D=1407` (visited on 03/18/2019).

[271] M. Lutz. *Learning Python: Powerful Object-Oriented Programming.* O'Reilly Media, Inc., 2013.

[272] Active Technologies. *AWG 1102/1104*. 2017. URL: `https://www.activetechnologies.it/products/signal-generators/arbitrary-waveform-generators/awg-1102-1104/` (visited on 03/18/2019).

[273] PyVISA. *PyVISA: Control your instruments with Python.* URL: `https://pyvisa.readthedocs.io/en/stable/` (visited on 03/18/2019).

[274] pythonnet.github.io. *Python for .NET*. URL: `https://pythonnet.github.io/` (visited on 03/18/2019).

[275] A. Rüfenacht et al. "Cryocooled 10 V programmable Josephson voltage standard". In: *IEEE Trans. Instrum. Meas.* 64.6 (2015), pp. 1477–1482.

[276] Cryomech, Inc. *PT-410*. 2019. URL: `https://www.cryomech.com/products/pt410/` (visited on 03/18/2019).

[277] Millitech Inc. *SERIES GDM - Mechanically-Tuned Gunn Oscillators.* 2009. URL: `http://www.millitech.com/MMW-Sources-GDM.htm` (visited on 03/18/2019).

[278] S. I. Borovitskii et al. "Increasing the working voltage across chains of Josephson junctions". In: *Pisma v Zhurnal Tekhnischeskoi Fiziki* 11 (1985), pp. 663–667.

[279] EURAMET e.V. *"A quantum standard for sampled electrical measurements"*. 2019. URL: `https://www.euramet.org/research-innovation/search-research-projects/details/?eurametCtcp_project_show%5Bproject%5D=1182&eurametCtcp_project%5Bback%5D=472&cHash=0dbcdfd402c0d01f7106f7bd187e7a99` (visited on 03/18/2019).

[280] A. Sosso et al. "Characterization of a Josephson array for pulse-driven voltage standard in a cryocooler". In: *Measurement* 95 (2017), pp. 77–81. DOI: `https://doi.org/10.1016/j.measurement.2016.09.039`.

[281] A. Sosso et al. "Tests on waveform synthesis in a new cryocooler setup". In: *2016 Conference on Precision Electromagnetic Measurements (CPEM 2016).* July 2016, pp. 1–2. DOI: `10.1109/CPEM.2016.7540563`.

[282] A. Sosso et al. “Towards Mitigation of Cable-Loading Effect with a Cryocooled Pulse-Driven Josephson Standard”. In: *2018 Conference on Precision Electromagnetic Measurements (CPEM 2018)*. July 2018, pp. 1–2. DOI: `10.1109/CPEM.2018.8501217`.

[283] J. Kohlmann et al. “A quantum standard for sampled electrical measurements - main goals and first results of the EMRP project Q-WAVE”. In: *29th Conference on Precision Electromagnetic Measurements (CPEM 2014)*. 2014, pp. 522–523. DOI: `10.1109/CPEM.2014.6898489`.

[284] J. Kohlmann et al. “Development and investigation of SNS Josephson arrays for the Josephson arbitrary waveform synthesizer”. In: *IEEE Trans. Instrum. Meas.* 58.4 (2009), pp. 797–802.

[285] O. F. Kieler, T. Scheller, and J. Kohlmann. “Cryocooler operation of a pulse-driven AC Josephson voltage standard at PTB”. In: *World Journal of Condensed Matter Physics* 3.04 (2013), p. 189.

[286] Keysight Technologies. *83711B Synthesized CW Generator, 1 GHz to 20 GHz.* 2019. URL: `https://www.keysight.com/en/pd-1000001880%3Aepsg%3Apro-pn-83711B/synthesized-cw-generator-1-ghz-to-20-ghz?cc=IT&lc=ita` (visited on 03/18/2019).

[287] Anritsu. *12.5G Pulse Pattern Generator.* 2019. URL: `https://www.anritsu.com/en-us/test-measurement/products/mp1763c` (visited on 03/18/2019).

[288] National Instruments. *PXI-5922 Specifications.* Sept. 26, 2018. URL: `http://www.ni.com/documentation/en/pxi-oscilloscope/latest/specs-pxi-5922/specs/` (visited on 03/18/2019).

[289] Anritsu. *Signal Quality Analyzers - MP1800A.* 2019. URL: `https://www.anritsu.com/en-us/test-measurement/products/mp1800a` (visited on 03/18/2019).

[290] G. Venturini. *python-deltasigma - A port of the MATLAB Delta Sigma Toolbox based on free software and very little sleep.* 2013. URL: `http://www.python-deltasigma.io/` (visited on 03/18/2019).

[291] Keysight Technologies. *35670A FFT Dynamic Signal Analyzer, DC-102.4 kHz.* 2019. URL: `https://www.keysight.com/en/pd-1000001335%3Aepsg%3Apro-pn-35670A/fft-dynamic-signal-analyzer-dc-1024-khz?cc=US&lc=eng` (visited on 03/18/2019).

[292] Keysight Technologies. *3458A Digital Multimeter, 8 ½ Digit.* 2019. URL: `https://www.keysight.com/en/pdx-2905513-pn-3458A/digital-multimeter-8-digit?cc=IT&lc=ita` (visited on 03/18/2019).

[293] EURAMET e.V. *"Towards the propagation of ac quantum voltage standards"*. 2019. URL: `https://www.euramet.org/research-innovation/search-research-projects/details/?eurametCtcp_project_show%5Bproject%5D=1329` (visited on 03/18/2019).

[294] Physikalisch-Technische Bundesanstalt. *Josephson Effect, Voltage - Working Group 2.63*. URL: `https://www.ptb.de/cms/en/ptb/fachabteilungen/abt2/fb-26/ag-263.html` (visited on 03/18/2019).

[295] P. Kleinschmidt et al. "Investigation of binary Josephson arrays for arbitrary waveform synthesis". In: *IEE Proceedings-Science, Measurement and Technology* 149.6 (2002), pp. 313–319.

[296] Jülicher SQUID GmbH. *Phase Locked Oscillator*. URL: `http://jsquid.com/products/phase-locked-oscillator/` (visited on 03/18/2019).

[297] Keysight Technologies. *33522B Waveform Generator, 30 MHz, 2-Channel with Arb*. 2019. URL: `https://www.keysight.com/en/pd-2155053-pn-33522B/waveform-generator-30-mhz-2-channel-with-arb?cc=US&lc=eng` (visited on 03/18/2019).

[298] Sympuls. *Bipolar Pattern Generators*. Mar. 2, 2017. URL: `http://www.sympuls-aachen.de/en/bmg_ter.html` (visited on 03/18/2019).

[299] Fluke Corporation. *5700A/5720A Multifunction Calibrators*. 2019. URL: `https://us.flukecal.com/products/obsolete-products/5700a5720a-multifunction-calibrators?quicktabs_product_details=2` (visited on 03/18/2019).

[300] Audio Precision, Inc. *APx555 Audio Analyzer*. 2019. URL: `https://www.ap.com/analyzers-accessories/apx555/` (visited on 03/18/2019).

[301] G. Ramm, H. Moser, and A. Braun. "A new scheme for generating and measuring active, reactive, and apparent power at power frequencies with uncertainties of 2.5×10^{-6}". In: *IEEE Trans. Instrum. Meas.* 48.2 (1999), pp. 422–426.

[302] Tektronix, Inc. *3390 Arbitrary Waveform Generator*. 2019. URL: `https://www.tek.com/arbitrary-waveform-generator/model-3390-50mhz-arbitrary-waveform-function-generator` (visited on 03/18/2019).

[303] T. J. Witt. "Testing for correlations in measurements". In: *Advanced mathematical and computational tools in metrology IV*. World Scientific, 2000, pp. 273–288.

This Ph.D. thesis has been typeset by means of the TEX-system facilities. The typesetting engine was pdfLATEX. The document class was `toptesi`, by Claudio Beccari, with option `tipotesi=scudo`. This class is available in every up-to-date and complete TEX-system installation.